École polytechnique de Louvain

Rotatable heterostructures with bilayer graphene and hexagonal boron nitride

Author: **Pauline de Crombrugghe de Picquendaele**
Supervisor: **Benoît Hackens**
Readers: **Jean-Christophe Charlier, Vincent Bayot**
Academic year 2020–2021
Master [120] in Physical Engineering

Abstract

Since the discovery of graphene, the development of van der Waals heterostructures has offered an unprecedented research playground for a wide range of remarkable breakthroughs in nanoscience. More recently, the study of how the twist angle between two layers can change the properties of the assembled materials has been a major point of interest, especially since the discovery of superconductivity in twisted bilayer graphene in 2018.

This work focuses on the case of an heterostructure in which hexagonal boron nitride (hBN) that is stacked and twisted on bilayer graphene (BLG), in a rotatable configuration. The aim is to investigate different phenomena arising at low angle, and on the other hand the angle dependence of electrical, optical, and frictional properties of the heterostructure. In this master thesis, the fabrication of a device allowing to study the twist angle effect in the hBN/BLG interface experimentally is presented, as well as the frictional, electrical and Raman measurements that were conducted on it.

Friction measurements on hBN/BLG yielded results with clear differences from the monolayer graphene/hBN case, and some hints for peculiar stable configurations at low twist angle. These observations forecast potential exciting findings in low angle states of the BLG/hBN superstructure that need to be confirmed, thus paving the way to further experimental and/or simulation studies.

Contents

Chapter 1

Introduction

In recent years, the development of two-dimensional materials such as graphene has provided an exceptional research playground to study all sorts of novel electronic behaviors. Stacking and combining different layers of those innovative materials into van der Waals heterostructures paved the way to other new exciting breakthroughs, with a nearly infinite number of new possibilities. Varying parameters such as the number of layers of a material, the alignment or misalignment between crystalline orientations etc. offers the ability to tune electronic properties of nanoscale devices, which represents an important step forward in modern technology and motivates lots of research in condensed matter physics.

The interlayer twist angle is a parameter raising particular interest in many studies, especially since the recent famous discovery of unconventional superconductivity in twisted bilayer graphene [1], a breakthrough which raises a lot of questions and hopes for the future of the field. Since then, similar superconductivity phenomena were reported in different moiré superstructures (bilayer/hBN, trilayer/hBN...) [2,3].

Besides the remarkable electronic properties studied in those heterostructures, there is also a growing interest in graphene and similar atomically flat materials for their peculiar frictional properties. The reduction of friction and wear represents indeed a crucial point in small mechanical devices as they cause energy loss and component failure in functional devices. In recent years, several studies have demonstrated the existence of an ultra-low friction state called superlubricity in graphitic structures. Graphene-based structures thus also have the potential to be used as a solid lubricant providing a good alternative to traditional liquid lubrication methods that are not adapted in many situations (small devices, confined conditions, high loads, high temperature, chemical contamination, vacuum environment, ...).

The purpose of this work is to investigate experimentally all sorts of properties and features arising in a rotatable heterostructures including a tunable moiré formed by bilayer graphene and hBN lattices. The objectives pursued were:

- to fabricate a functional electronic device with dynamically twistable layers of bilayer graphene and hBN (thus forming a tunable moiré superlattice);

- to reach the alignment of the BLG anf hBN crystalline orientations, then to be able to measure and control the twist angle;
- to investigate properties of the layered stucture in electronic, Raman and friction measurements, with possible comparison with the case of monolayer graphene;
- to test the electronic behavior at ultra low temperature, especially to check the possibility of emergence of unconventional superconductivity.

In the following chapters, the state of the art of the research field is first presented providing theoretical information about the topic. Then, the fabrication techniques are detailed, leading to the completion of the device. Finally the experimental work is described: the setup, methods, results and their interpretation are eventually reported.

Chapter 2

State of the art

In this chapter, an overview of the development of two-dimensional materials at stake in the device studied and of van der Waals heterostructures is provided, leading to the recent advances motivating this work.

The properties of graphene are first briefly introduced, without going into extensive details (as the topic is more oriented towards bilayer graphene and hBN/BLG/hBN heterostructures); then the properties that are different in bilayer graphene (BLG), and properties of hexagonal boron nitride (hBN) are presented; the development of van der Waals heterostructure is discussed, emphasizing on hBN/graphene heterostructures and the discoveries yielded from their moiré superstructure; the novel rotatable device architecture is also presented and the experiments realized thanks to it; recent observations in hBN/BLG moiré are unveiled; and finally, the motivations retrieved from these various advances are explained.

2.1 Graphene

Graphene is the very first 2D crystal ever elaborated. It is formed of an hexagonal lattice of carbon atoms arranged in a honeycomb-like pattern, and corresponds to an isolated single layer of graphite. Figure 2.1-a and b provide respectfully a scanning tunneling microscope (STM) image of graphene and an illustration of the structure of graphene. Andre Geim and Konstantin Novoselov were the first to isolate and experimentally demonstrate the exceptional properties of graphene in 2004, which granted them the Nobel prize in 2010 [4].

As shown on Figure 2.1c, each carbon atomic orbital presents an sp^2 hybridization, allowing for covalent σ-bonding with 3 neighboring atoms in the $x-y$ plane, and leaving one electron on a $2p_z$ orbital, perpendicular to that plane. The neighboring $2p_z$ orbitals hybridize together to form the π-band and $\pi^\star$-bands, in which charge carriers contributing to transport can flow, forming a confined two-dimensional delocalized electron gas (2DEG), which is decisive in the emergence of the peculiar electronic properties

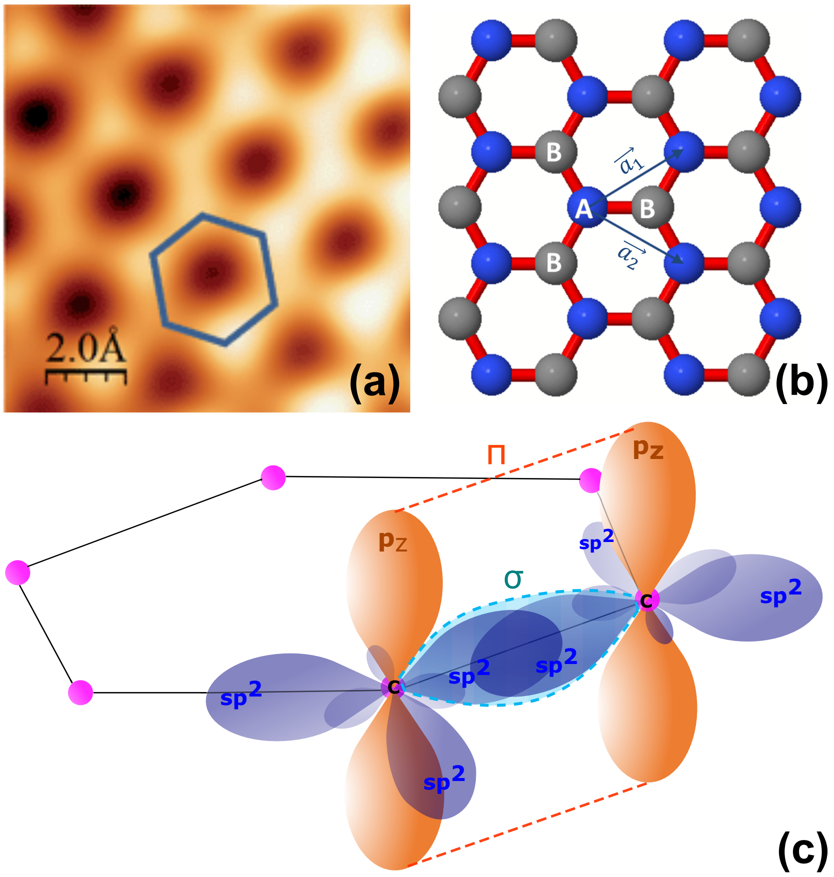

Figure 2.1: (a) High resolution STM image of monolayer graphene (FFT filtered image) [5]. (b) Triangular sublattices of graphene [6]. (c) Schematic representation of carbon hybridization in graphene. $2p_z$ orbitals are represented in orange, sp^2 hybridized orbitals in blue, carbon atoms in pink, pi and sigma bonds are outlined by the orange and green doted lines.

of graphene [6].

Crystallographic structure

The hexagonal geometry of graphene can not be directly characterized by one Bravais lattice. It can be considered as the result of two interleaving triangular lattices, or equivalently as a primitive hexagonal Bravais lattice with 2 atoms labeled A and B represented on Figure 2.1-b in blue and grey respectively. The distance between two carbon atoms sharing a σ bond is about L = 1.42 Å and the primitive unit cell is defined by the lattice vectors $\vec{a}_1 = \frac{L}{2}(3, \sqrt{3})$ and $\vec{a}_2 = \frac{L}{2}(3, -\sqrt{3})$. The lattice parameter is thus $a = 2.46$ Å.

The direct and reciprocal lattice of graphene are depicted on Figure 2.2-a and b. The first Brillouin zone is characterized by three highly symmetrical points: Γ, K, and M. It must be mentioned that there are two sets of three Dirac points, so that the K points can be differentiated into K$_+$ and K$_-$, that are not equivalent (K$_+ = \frac{2\pi}{3L}\left(1, \frac{1}{\sqrt{3}}\right)$ and K$_- = \frac{2\pi}{3L}\left(1, -\frac{1}{\sqrt{3}}\right)$).

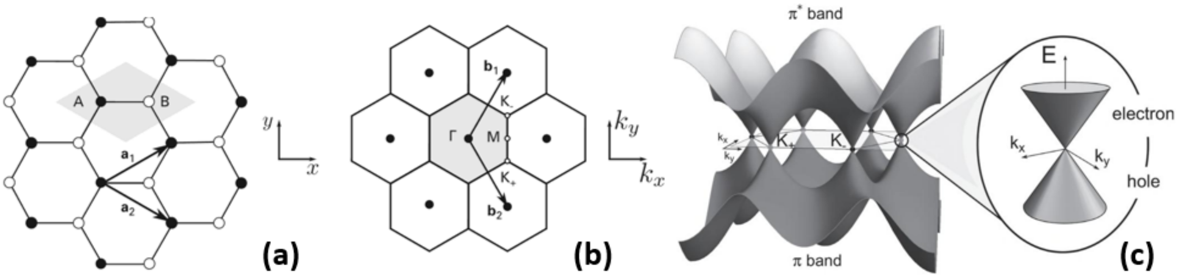

Figure 2.2: (a) Direct lattice of graphene, with $\mathbf{a_1}$ and $\mathbf{a_2}$ the basis vectors (b) Reciprocal lattice of graphene with the associated basis vectors $\mathbf{b_1}$ and $\mathbf{b_2}$. The unit cell and first Brillouin zone are colored in gray in (a) and (b). (c) π and π^* electronic bands. All figures from ref. [7]

Electronic properties

In the past 15 years, various experiments, simulations and theoretical works demonstrated that graphene exhibits all kinds of exceptional properties: mechanical (it is extremely stiff), thermal (it has one of the highest thermal conductivity coefficient), or optical, ... But the features of interest in this work are related to its surprising electronic properties, arising from the confinement of electrons in 2D systems in the π and $\pi^\star$-bands.

The band structure of graphene, that can be seen on Figure 2.2-c is truly unique and correlated to many novel physical phenomena. The conduction and valence bands meet at the Dirac points K_+ and K_-, forming a cone shape called the Dirac cone. In undoped graphene, the point where the bands meet coincides with the Fermi level. Graphene is thus considered as a semimetal or a zero-gap semiconductor. Around these points, instead of the usual parabolic curve, the dispersion of energy is linear.
The latter dispersion relation can be computed with a tight binding method. It was done for the first time by P.R. Wallace [8] in 1947 taking only into account the interaction between the nearest neighbor atoms with hopping energy γ_0, and the resulting expression of energy:

$$E_\pm(\mathbf{k}) = \pm\gamma_0\sqrt{1 + 4\cos^2\left(\frac{\sqrt{3}k_y a}{2}\right) + 4\cos\left(\frac{3k_x a}{2}\right)\cos\left(\frac{\sqrt{3}k_y a}{2}\right)} \tag{2.1}$$

can be developed in Taylor series near the points $\mathbf{k} = \mathbf{K}_+ + \delta\mathbf{k}$ and $\mathbf{k} = \mathbf{K}_- + \delta\mathbf{k}$, yielding:

$$E_\pm(\mathbf{k}) \approx \pm\hbar v_F|\delta\mathbf{k}| \tag{2.2}$$

where v_F is the electronic group velocity [7].

The linear dispersion obtained in Equation 2.2 leads to the conclusion that the free charge carriers in graphene mimic the behavior of massless relativistic Dirac fermions (quasi-particles), moving with a speed v_F independent of their energy, analogous to an effective "speed of light". Therefore, electrons and holes in graphene are described by the Dirac equation.

The pseudo-relativistic Dirac fermions model describing the behavior of charge carriers has several consequences such as the minimum conductivity in graphene, which can not decrease below a quantum unit of conductance ($G_0 = \frac{e^2}{h}$) and the "half-integer" quantum Hall effect (QHE) [9].
Another consequence is the linear dependence of the density of states (DOS) as a function of energy. Due to this, graphene exhibits a strong ambipolar field effect: the charge carriers concentration can be tuned continuously from electrons to holes under the effect of a gate voltage V_G. This phenomenon is described as an electric field effect (EFE) induced carrier doping. The effect on the filling of the bands is illustrated in Figure 2.3: the gate voltage shifts the Fermi energy, determining the maximum level in the valence or conduction band filled with electrons or holes. When $V_G = 0$ V, the density of state is zero and the conductivity would be expected to be zero too, although it keeps a finite value of $\frac{e^2}{h}$, as pointed out earlier.

It is also worth mentioning that the relativistic character of charge carriers grant them an exceptionally high mobility, that can exceed 15 000 cm^{2}V^{-1}s^{-1} under ambient conditions [10]. Mobilities higher than 200 000 cm^{2}V^{-1}s^{-1} have proved to be achievable, when extrinsic disorder is eliminated [11], and even 1 000 000 cm^{2}V^{-1}s^{-1} in suspended devices [12–14] (at room temperature in both cases). In contrast, the mobility in silicon MOSFET devices lies typically well below 10 000 cm^{2}V^{-1}s^{-1}.

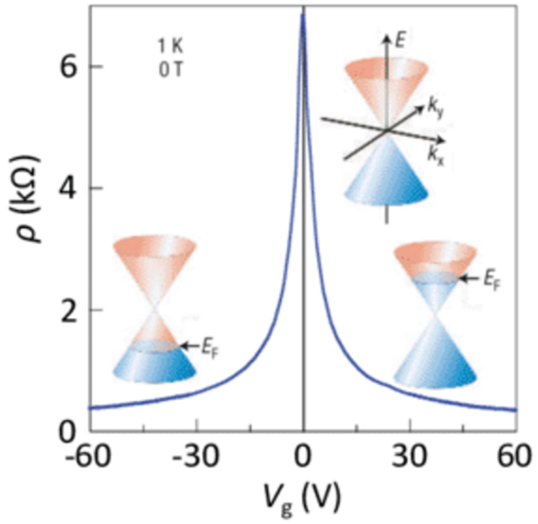

Figure 2.3: Electric field effect in graphene at T = 1 K, and in absence of magnetic field. The evolution of the resistivity is plotted as a function of gate voltage V_g [10].

2.2 Bilayer graphene

Bilayer graphene (BLG) is formed by a stack of two monolayer graphene (MLG) sheets, linked by van der Waals interactions. The most stable form of stacking is called Bernal stacking (AB stacking) and corresponds to the type of stacking found in nature in graphite. In this stacking structure, the planes are shifted with respect to one another. Perfectly aligned layers (AA stacking) can also be manufactured but are extremely difficult to obtain. These two types of stacking are shown on Figure 2.4.

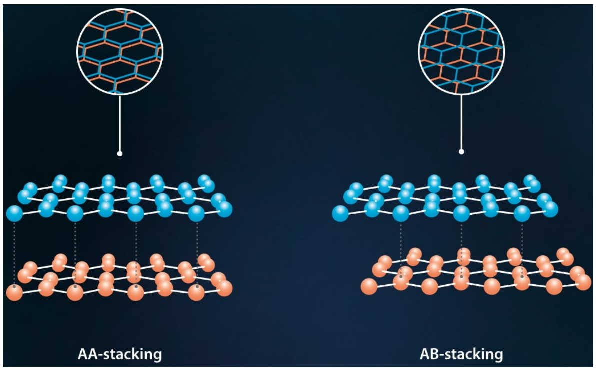

Figure 2.4: Schematic representation of AA and AB stacking of graphene bilayer [15].

Electronic properties of Bernal-stack bilayer graphene

Surprisingly, graphene systems with a few layers behave both differently from monolayers and from graphite. Bilayer graphene has the particularity to exhibit a tunable band gap, which probably makes it the most interesting type of multilayer graphene for electronic device application purposes. Indeed, by applying a perpendicular electrical field via a gate voltage (or by chemical doping or creation of defects in the lattice), a band gap can be induced, reaching up to 0.25 eV. When the Fermi level lies within this gap, the bilayer can become insulating at 0 K [16].

This phenomenon is due to the high sensitivity of graphene band structure to the lattice symmetry. If an hexagonal lattice contains nonequivalent elements, the broken lateral symmetry gives rise to the formation of a gap between π and π^* states. This explains the insulating behavior of hexagonal boron nitride (as will be discussed later) as well as the gap appearing when doping or when defects are present. In the vertical direction, the symmetry can also be broken, notably when two layers of graphene are assembled in Bernal stacking, by applying an electric field for instance. [17]

The band structure of bilayer graphene is shown on Figure 2.5-a. At first sight, it seems similar to the band structure of graphene: conduction and valence band coincide at the Dirac points in absence of perturbation. However, as the unit cell of the bilayer contains four atoms (see Figure 2.6-a), two additional bands emerge (one additional valence band and one additional conduction band) because of interlayer coupling effects that lead to duplication of bonding and antibonding orbitals.

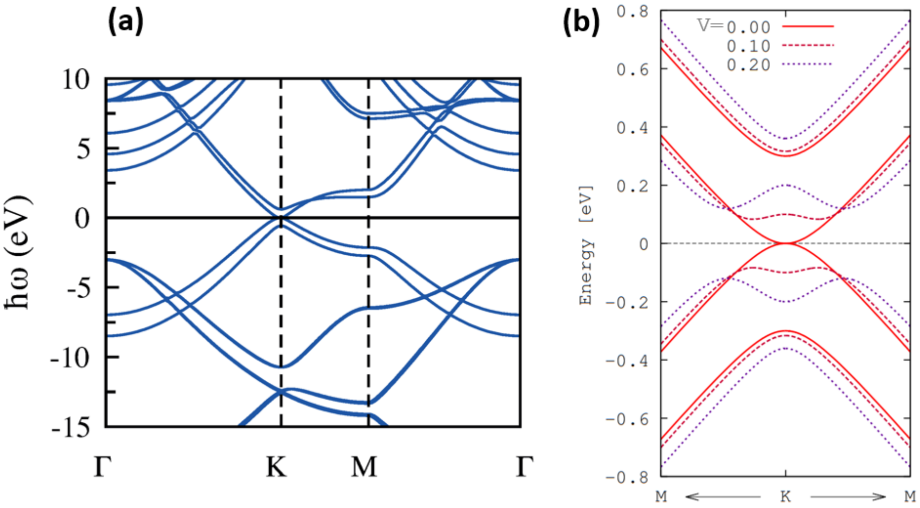

Figure 2.5: (a) Band structure of bilayer graphene along the direction $\Gamma - K - M - \Gamma$ (high symmetry points in reciprocal space) [18]. (b) Low-energy tight-binding band-structure of bilayer graphene under the effect of different (vertical) bias intensities V [19].

The dispersion is computed with a tight binding model, very similarly to graphene. But this time, in addition to the in-plane interaction with hopping energy γ_0, the strongest inter-layer interactions γ_1 ($B_1 - A_2$, see Figure 2.6-b) are taken into account.

In absence of electric field, the result is approximated as a function of p, the momentum close to the Dirac points:

$$E_{\pm}(p) \simeq \pm\frac{\gamma_1}{2}\left[\sqrt{1 + 4v^2p^2/\gamma_1^2} - 1\right] \tag{2.3}$$

giving thus a parabolic band structure at small momentum ($p \ll \gamma_1/2v$), in contrast to monolayer [20]. Charge carriers are then associated to massive Dirac fermions of effective mass $m^* = \frac{\gamma_1}{2v_F^2} = 0.054\ m_e$ (with m_e the electron mass)

Applying a gate voltage renders individual layers of graphene inequivalent and opens an energy gap at the Dirac point.
This is translated in the tight binding model by the term Δ representing the asymmetry between on-site energies of the two lattices. The expression in Equation 2.3 is modified and becomes [21]:

$$E_{\pm}(p) = \pm\sqrt{\frac{\gamma_1^2}{2} + \frac{\Delta^2}{4} + v_f^2p^2 - \sqrt{\frac{\gamma_1^4}{4} + \left(\gamma_1^2 + \Delta^2\right) v_f^2p^2}} \tag{2.4}$$

displaying a distinctive 'Mexican hat' shape and a band gap Δ_g:

$$\Delta_g = \frac{|\Delta|\gamma_1}{\sqrt{\gamma_1^2 + \Delta^2}}. \tag{2.5}$$

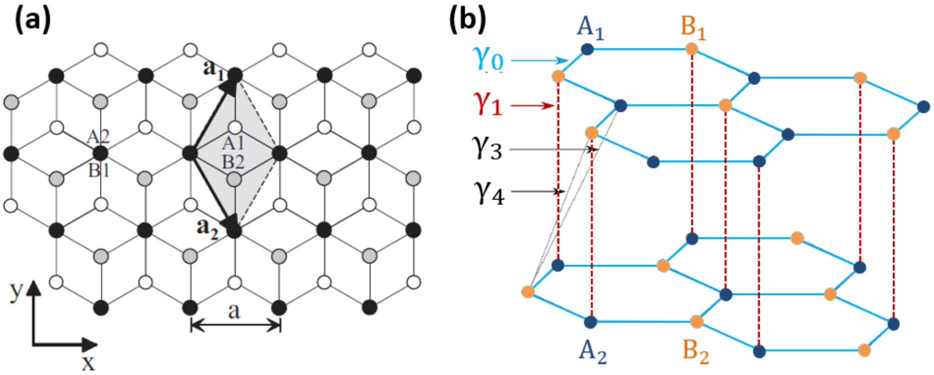

Figure 2.6: (a) Plane [21] and (b) side view of the crystal structure of Bernal bilayer graphene (adapted from [22]).

Figure 2.5-b shows the effect of different intensities of a perpendicular electric field on the low-energy region of the band structure.

Twisted bilayer graphene

Stacks of graphene exist not only under the form of aligned layers. Bilayer structures can be assembled with a certain twist angle, which yields ”twisted bilayer graphene” (or tBLG).

Although this topic is not at the center of this work, it is worth mentioning that the world of nanoscience was recently revolutionized by the discovery of some exceptional behavior in twisted bilayer graphene (tBLG): when the twist corresponds to a certain angle called ”magic angle”, the tBLG turns into a superconductor, among other interesting new properties [1]. The latter properties stem from the periodic moiré superlattice that arises from the superposition of periodic patterns differing by their relative orientation (i.e. the twist angle) and/or periodicity (more information about moiré can be found in section 2.4).

Since this discovery, signatures (or mere traces) of unconventional superconductivity have been reported in a few other heterostructures (twisted double bilayer graphene [23, 24], ABC-stacked trilayer graphene/hBN superlattice [3], bilayer graphene/hBN superlattice [2]...)

2.3 Hexagonal boron nitride

Hexagonal boron nitride (hBN) is another well-known material presenting a honeycomb structure (in Bernal stacked layers).

Also called ”white graphite”, its structure is analogous to that of graphite, with boron and nitrogen atoms instead of each pair of carbon, and a slightly different lattice parameter compared to graphene or graphite (see Figure 2.7). In addition to being a close analogue of graphite, hBN is, unlike graphene, a large-bandgap insulator (6 eV) and can

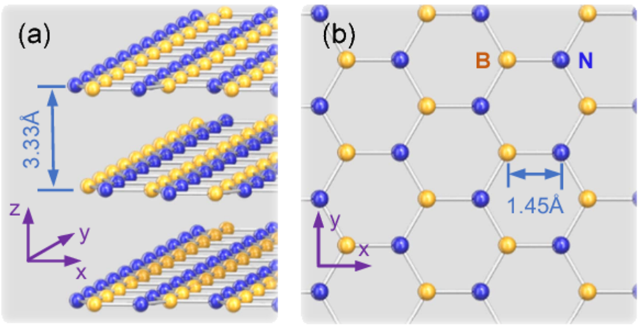

Figure 2.7: Crystal structure of hBN. (a) 3D side view of the crystal. Layers are kept together by van der Waals forces. (b) Top view of the crystal. [25]

be exfoliated into few atomic layers, just like graphite. These properties justify its wide use as an ultraflat insulating substrate for graphene-based heterostructures [25].

The band structure can again be explained by a very similar tight-binding model as the one used for graphene. Indeed, taking the nearest-neighbor interactions into account, the solution for the energy of any hexagonal lattice can be generalized as:

$$E = \frac{1}{2N}\left[\mathcal{H}_{AA} + \mathcal{H}_{BB} \pm \sqrt{(\mathcal{H}_{AA} - \mathcal{H}_{BB})^2 + 4\left|\mathcal{H}_{AB}\right|^2}\right] \tag{2.6}$$

$\mathcal{H}_{AA}, \mathcal{H}_{BB}, \mathcal{H}_{AB}$ are the matrix elements of the Hamiltonian for sites labeled A and B. Whereas in graphene $\mathcal{H}_{AA} = \mathcal{H}_{BB}$ (A and B are both associated to carbon atoms), simplifying the expression as $E = \frac{1}{N}\left[\mathcal{H}_{AA} \pm |\mathcal{H}_{AB}|\right]$, in hBN, sites represent different atoms (B and N), breaking thus the lateral symmetry. The simplification is no longer valid and the expression for the energy becomes:

$$E = \frac{1}{N}\left[E_m \pm \frac{1}{2}\sqrt{E_g^2 + 4\left|\mathcal{H}_{AB}\right|^2}\right] \tag{2.7}$$

where $E_m = (\mathcal{H}_{AA} + \mathcal{H}_{BB})/2$ and $E_g = |\mathcal{H}_{AA} - \mathcal{H}_{BB}|$ is the bandgap. This non-zero E_g term obviously prevents the expression under the square root to cancel, which means that the valence and conduction band can not meet. The gap is direct in a monolayer while indirect in bulk hBN, as is the case for many 2D crystals.
The band structure is shown on Figure 2.8. The bandgap is underestimated using DFT techniques, because of strong approximations used in the calculations [7].

2.4 van der Waals heterostructures

2.4.1 General considerations

The rise of graphene paved the way to the creation of new two-dimensional (2D) atomic monolayer crystals such as hexagonal boron nitride, transition metal dichalcognenides (MoS_2, WSe_2, etc..), thin oxide layers (TiO_2, MoO_3, WO_3, etc.), but also silicene,

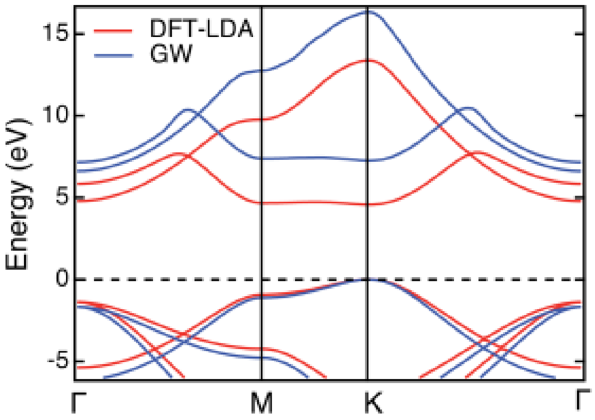

Figure 2.8: DFT-LDA (red) and GW (blue) *ab initio* band structures of a single hBN layer in the MK region [26]

germanene, etc. In recent years, an extensive library of those miscellaneous crystals has been built up. This in turn led to the idea of combining such 2D materials into novel hybrid heterostructures by stacking them, layer by layer, in a chosen sequence. The emergence of these so-called van der Waals (vdW) heterostructures marked the coming of a new era in nanoelectronics.

According to A. Geim and I. Grigorieva [27], although the fundamental science of graphene is far form being exhausted, the focus of research has somewhat shifted from studying graphene itself to its use in applications and the other promising 2D crystals. VdW heterostructures represents thus a new field of choice: assembling highly disparate materials (with no constraint of crystal matching [25]) has proven to give rise to new synergic properties and phenomena. These properties are singular as they are not a simple superposition of the properties of the individual components, and sometimes can be tuned by modifying the sequence of 2D crystals. The infinite number of possible combinations forecasts the longevity of the field.

Graphene, that is an undeniable champion in terms of mechanical strength and electronic qualities, plays a central role in many of them, remaining a unique platform for exploring low-dimensional physics, especially in combination with more versatile materials. The latter have the advantage of exhibiting a large range of direct bandgaps (as illustrated on Figure 2.9), which is an important asset to exploit in order to design new electronic devices [7].

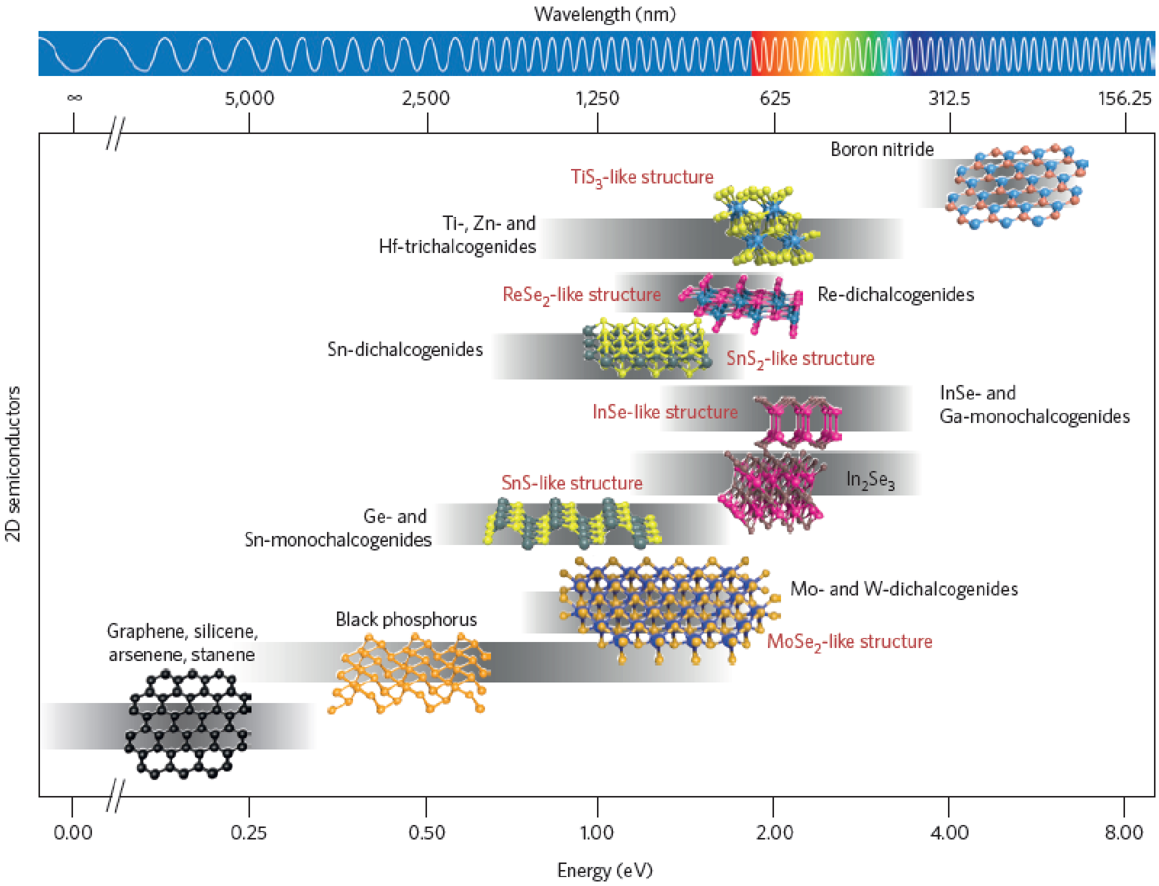

Figure 2.9: Comparison of the bandgap values of different 2D crystal families [28].

2.4.2 Graphene-hBN heterostructures

Graphene on hBN can be considered as the first model of vdW heterostructure [27] and remains nowadays a subject of great interest.

Graphene on hBN: the perfect substrate

Dean *et al.* [29] demonstrated that hBN could serve as a high-quality substrate for graphene and provided a comparison with graphene on SiO$_2$ substrates, mainly used until then. Charge carrier mobilities measured on SiO$_2$ reach values of the order of 10 000 cm^{2}V^{-1}s^{-1} [10], and are limited by scattering from charged surface states and impurities, substrate surface roughness, and optical phonons [29]. The quality is also impacted by substate-induced disorder breaking up the 2DEG into inhomogenous network of electron and hole puddles [30], and causing uncontrolled doping. Mobilities obtained in suspended devices are naturally substantially higher, exceeding 100 000 cm^{2}V^{-1}s^{-1} and 1 000 000 cm^{2}V^{-1}s^{-1} respectively near room and liquid-helium temperature (for a low carrier concentration $n \sim 10^{11}$cm^{-2}) [31, 32], but this configuration imposes severe limitations (extreme fragility, susceptibility to the ambient atmosphere, stress and strain issues, etc.).

Thanks to its lattice constant relatively similar to that of graphene, its large bandgap and its atomically smooth surface, hBN substrates allow to enhance mobility, reduce carrier inhomogeneity, as well as intrinsic doping, in comparison with SiO_2 substrates (as proven by transport measurements) [29].

Going one step further, graphene can be encapsulated in hBN (an additional flake of hBN placed on top offers a protection from environmental factors), enabling devices of impressively high quality, reaching mobility higher than 100 000 $cm^2V^{-1}s^{-1}$ even at room temperature (at $n \sim 10^{11}cm^{-2}$) [33], and thus rivalling those of suspended devices.

Moiré superlattice effects

The interatomic distance (1.45 Å) in hBN is a little larger than in graphene (1.42 Å), resulting in a small mismatch ($\sim 1.8\%$) between the lattices when assembled together. The combination of periodicity of the two lattices and this mismatch engenders a larger periodic pattern called "moiré" and thus, in terms of potential, a superlattice with a larger unit cell : the moiré superlattice.

A slightly different moiré superlattice is also obtained when the layers of graphene and hBN are twisted of certain angles as shown on Figure 2.10.
The large moiré superlattice generated at small twist angles is characterized by a moiré wavelength λ that can be written as a function of θ, the rotational mismatch angle between the two crystals :

$$\lambda = \frac{(1+\delta)a}{\sqrt{2(1+\delta)[1-\cos(\theta)]+\delta^2}} \tag{2.8}$$

where a is the lattice constant of graphene and δ is the lattice mismatch between graphene and BN ($1+\delta$ is the ratio between the hBN and the graphene lattice constants, which is $\simeq 1.018$).

Although hBN was chosen in order to reduce the influence of the substrate on electronic properties, the relatively weak interactions between the stacked 2D crystals still impact the potential map. Electron orbitals extending out of the plane affect charge carriers in graphene, generating the superlattice potential. This potential is responsible for modulations in the DOS, resulting in novel quantum phenomena such as Hofstadter's butterfly and fractal quantum Hall effect [35]. Multiple minibands are observed [36] and the lattice mismatch is expected to induce a bandgap in graphene at the charge neutrality points (CNP) [37]. An important consequence is the appearance of additional Dirac cones called "secondary" or "satellite" Dirac points, at higher energies than the CNP [38], as shown on Figure 2.11. Pronounced peaks in resistivity were the first signature observed of these satellite points as shown on Figure 2.12 [37, 39]. The superlattice effect is actually so strong that the Hall effect changes its sign and the new secondary Dirac cones exhibit their own sets of Landau levels.

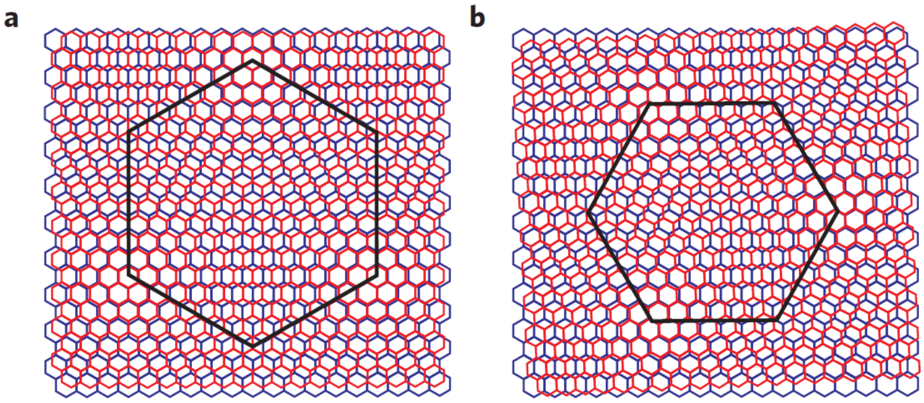

Figure 2.10: Schematic representation of the moiré pattern of graphene (red) on hBN (blue) for a relative rotation angle between the crystals a) $\theta = 0°$ and b) $\theta = 3°$ [34]. The mismatch between the lattices is exaggerated (10%). Black hexagons highlight the moiré supercell.

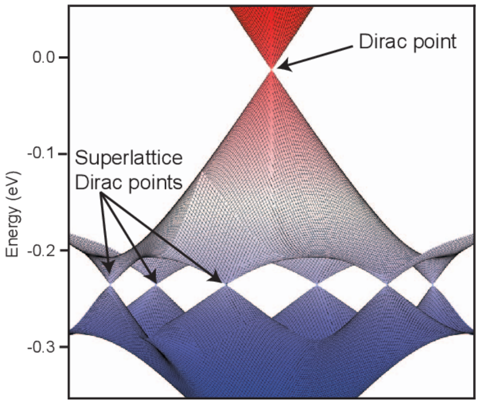

Figure 2.11: Band structure of graphene on hBN [40]. The appearence of six secondary Dirac points (superlattice Dirac points) is shown in addition to the original Dirac point.

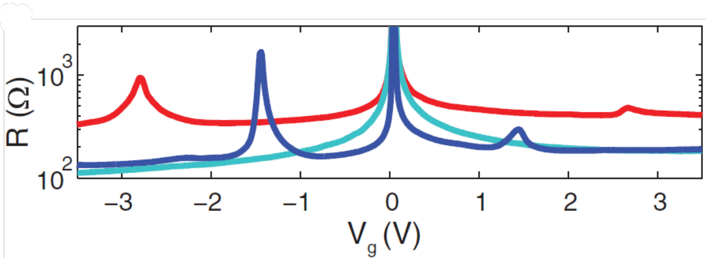

Figure 2.12: Measurement of the resistance as a function of the gate voltage at zero magnetic field, in three hBN-graphene devices (indicated by the different colors) with different misalignment angles [37]. The resistance peaks indicate full filling of the lowest superlattice miniband in two of the measured devices (dark blue and red curves) within the experimentally accessible density range.

2.4.3 Twistronics

As mentioned previously, devices with arbitrary rotational order can be created thanks to the weakness of the van der Waals forces acting between planes in two-dimensional materials. These materials are generally exfoliated and then positioned on top of another with a targeted and fine-tuned misalignment. The approach consisting in manipulating the 2D materials properties by controlling the relative twist angle between successive layers is referred to as twistronics [41]. The twist can destroy the alignment and thus break the translational symmetry, giving birth to interesting twist-dependent features, as illustrated previously with the case of tBLG (section 2.2).

When layers of materials with different lattice parameters are twisted on top of each other, another aspect is important to take into account: commensurability. Interestingly a commensurate-incommensurate transition was observed in graphene-hBN systems at a certain angle of the order of ∼1° [34]. At smaller twist angles, relatively large areas form where graphene stretches to adapt to the hBN periodicity with matching lattice constants. These areas are separated by domain walls where the generated strain is accumulated, in order to reach an energetically favorable state for vdW interactions.
For a misorientation larger than this angle however, the elastic energy is too large to be compensated by vdW interactions and graphene exhibits little adjustment. The lattices then remain unsynchronized.

2.5 Graphene-hBN rotatable heterostructures

In 2018, Rebeca Ribeiro-Palau achieved an important breakthrough in the field of Graphene/hBN heterostructures: she created with her team a device architecture in which an h-BN layer (shaped as a wheel or a rudder) can be dynamically twisted in situ, on a graphene layer with an AFM tip [42] (this section is entirely based on Ref. [42]). The prototype is schematized on Figure 2.13A and imaged by AFM on Figure 2.13B-D.

Until then, all the heterostructures developed in previous studies, with controlled rotation between the layers [35,37–39,43–45] required a presumed knowledge of orientation of each layer before assembly. With this architecture, for the first time, the twist angle can be modified after assembly of the device.

The on-demand control of the orientation between layers allows to investigate properties of the heterostructure at arbitrary rotation angles. Optical, mechanical and electronic properties were probed by measuring optical Raman spectrum, friction between the hBN wheel and graphene, and four-terminal transport for a large range of angles and thus also as a function of the moiré wavelength.

Raman spectroscopy

The technique is described in section 3.2.3. The measured spectra shown on Figure 2.14) allowed to identify and calibrate the angle θ, mainly by using the relation between the

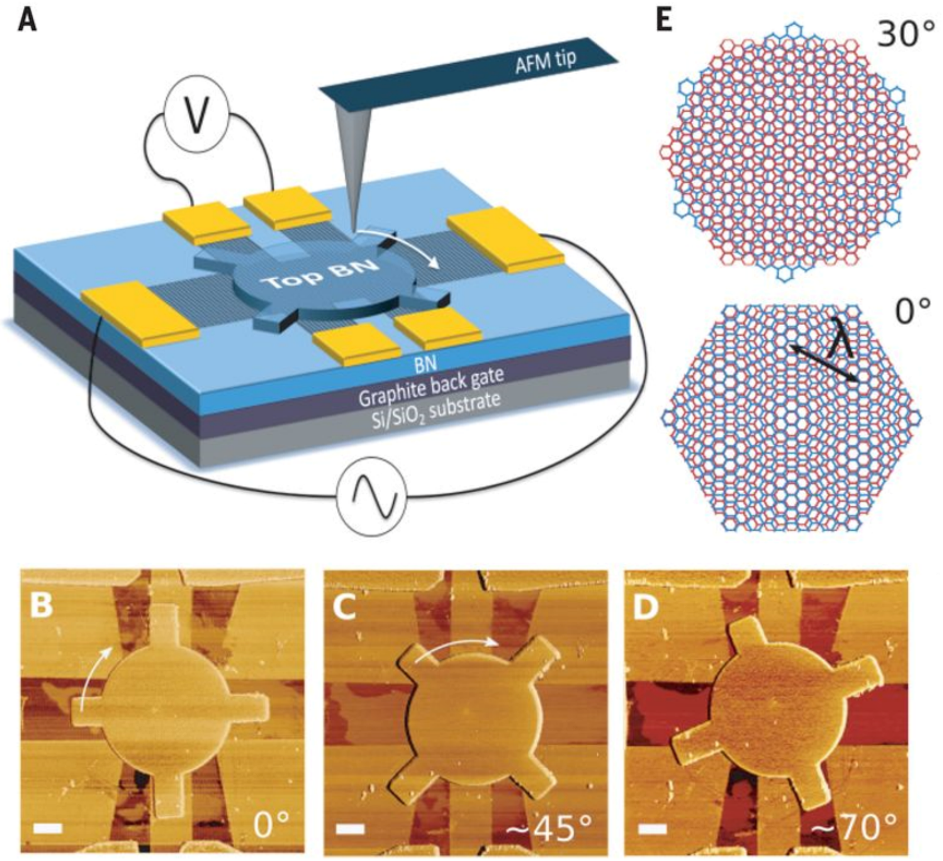

Figure 2.13: (A) Schematic of the device structure and the experimental technique used. (B to D) AFM image of the device with the hBN wheel rotated at three different orientations. The angle value labeled in each panel is an absolute angle referenced to the AFM coordinates (θ_A). Scale bars: 1 mm. (E) Schematic drawing of the moiré superlattice appearing between graphene (red) and hBN (blue) at zero angle and 30°. The length λ is the moiré wavelength. [42]

full width at half maximum (FWHM) of the 2D peak and the angle or moiré wavelength, that was already highlighted in previous studies [34,46]. A peak arises at an orientation corresponding to the zero-angle (Figure 2.14.

The results also brought a new light to the question of commensurate states in encapsulated graphene devices, requestioning its very existence. Indeed, the same trend in Raman FWHM evolution is observed for orientations at which no commensurate regions are expected and for commensurate angles (for which linear and narrower 2D linewidth is expected than in non-encapsulated devices).

Friction

In this study, for the first time the dynamic friction between hBN and a single layer of graphene could be characterized. The measurement principle is well described by the

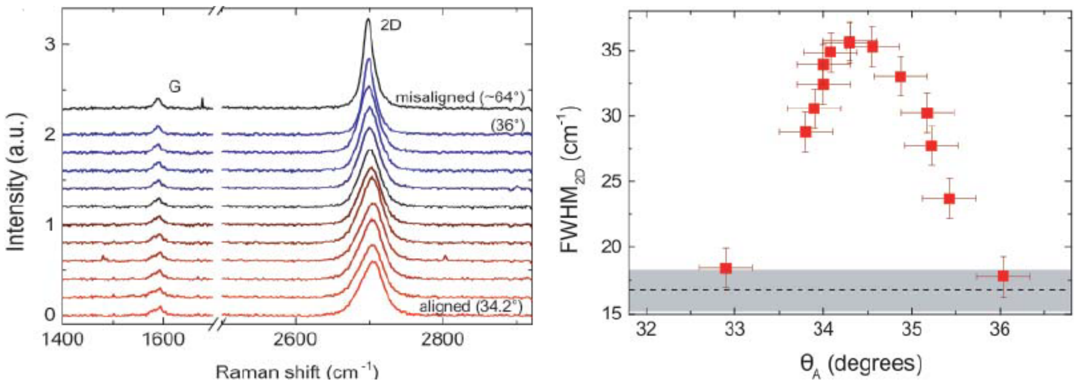

(a) (b)

Figure 2.14: (a) Raman spectrum of the heterostructure for an absolute angle θ_A between 34.2 and 36.0°. An additional measurement at $\sim 64°$ is also shown on the black curve. a.u., arbitrary units. (b) FWHM of the 2D peak in function of the absolute angle. The gate bias is held at $V_g = 0$ V for every measurement. Zero-angle crystallographic alignment is identified by the maximum FWHM position. The dashed line shows the FWHM measured for every angle larger than $\sim 2°$ from perfect alignment (the shaded region representing the associated uncertainty). [42]

illustration on Figure 2.15: when the AFM tip encounters an obstacle, it undergoes a torque and cants away from its vertical position, which causes a lateral deflection of the laser spot on the four-quadrants photodetector, and thus yielding a voltage difference (Figure 2.15-A ; note that the principle of AFM is explained in chapter 3).
To start moving the wheel, the AFM must go through 3 steps or regimes, that are revealed by the tip deflection as shown on Figure 2.15-B: the AFM tip slides on the surface (regime (i): tip-substrate dynamic or sliding friction) until it meets the hBN wheel causing it to cant away from the vertical direction (regime (ii): hBN-graphene static friction); then at some point the tip starts to push the wheel over the surface (regime (iii): hBN-graphene dynamic friction).

Under uninterrupted rotation, the dynamic friction between the two layers was also continuously measured. The deflection is plotted on Figure 2.15-C, exhibiting two prominent peaks separated by 60°.
The friction response represents thus another method for controlling the alignment in situ.

Electronic transport

Finally, electronic transport was also measured for various relative orientations of the overlayer. The plot of the four-terminal resistance (for different values of θ) shown on Figure 2.16 shows good agreement with the previous studies, with the appearance of satellite Dirac points near $\theta = 0$ (cfr. section 2.4.2) [37], due to the scattering from the superlattice potential.

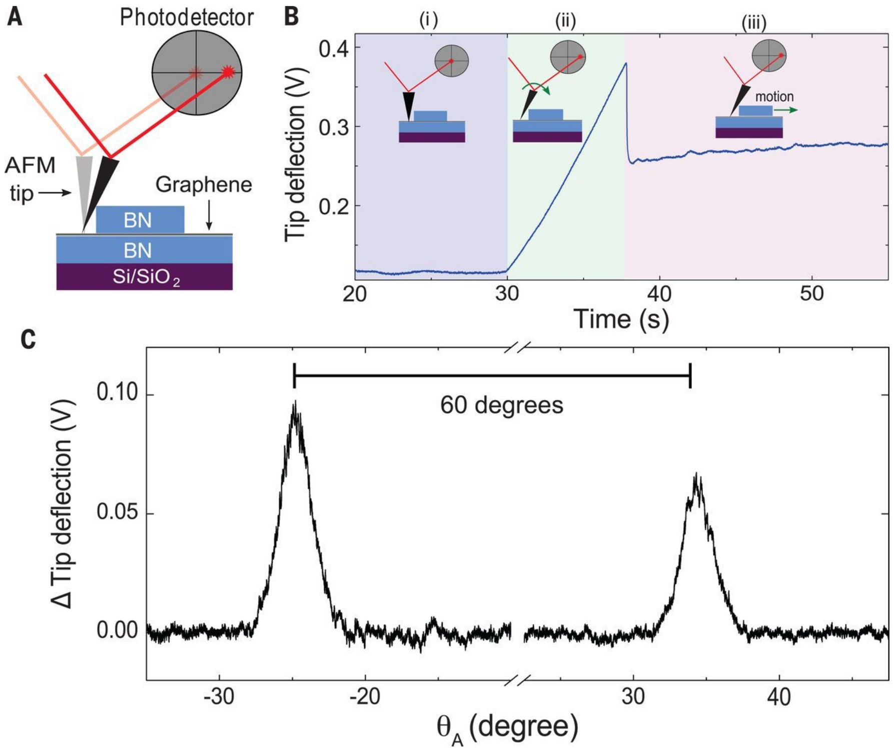

Figure 2.15: (A) Schematic representation of the friction measurements principle: as the AFM tip is canted away from its vertical postion when pushing against the hBN structure, the laser spot is repositioned on the four-quadrant photodetector, and the measured voltage difference is proportional to the tip deflection. (B) Tip deflection measurement as a function of the time, during a translational push of the hBN wheel. The three regimes identified on the curve are: (i) tip-substrate friction (resulting in a steady-state tip deflection); (ii) hBN-graphene static friction (the tip has encountered the hBN but the latter still resists to the translation motion); (iii) hBN-graphene dynamic friction (once the hBN moves, the tip deflection relaxes a little). (C) Measurement of the relative tip deflection as a function of the absolute angle, during continuous rotation of the wheel. Two prominent peaks appear 60°apart. [42]

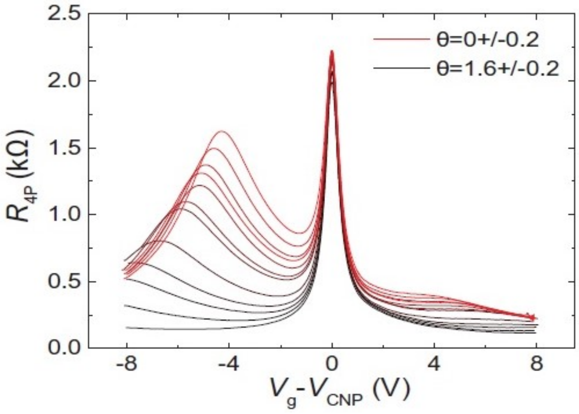

Figure 2.16: Four-terminal resistance (R_{4P}) plots as a function of the back-gate voltage V_g for different relative rotation angles of the graphene/hBN lattices (acquired at room temperature) [42].

Interestingly when increasing the misalignment angle, the intensity of the satellite peaks diminishes, and the distance between those peaks and the CNP (which remains steady) increases. The position and amplitude of the secondary peaks are plotted as a function of the angle θ and the moiré wavelength λ on Figure 2.17.

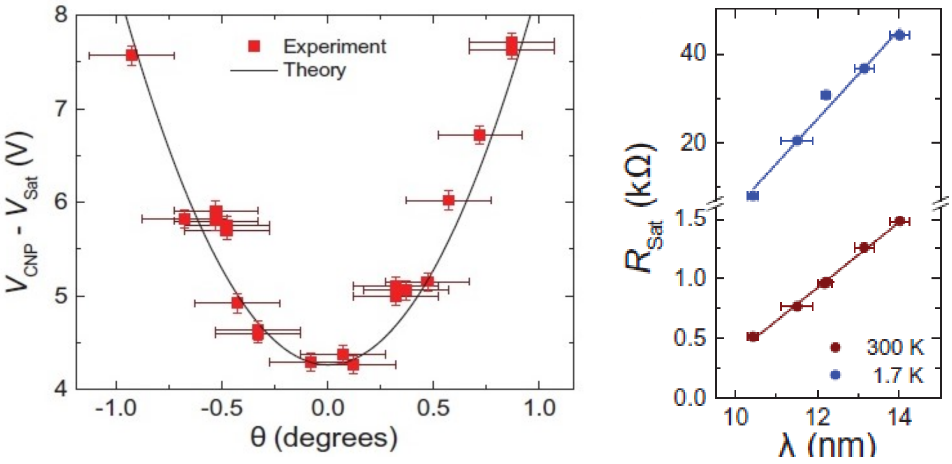

(a) (b)

Figure 2.17: (a) Satellite peak position (in gate voltage, relatively to the CNP position) as a function of the relative angle. (b) Linear evolution of the satellite peak resistance in function of the moiré length λ, at 300 K (red) and 1.7 K (blue). [42]

The voltage interval between the satellite peak and the CNP varies with the angle following a trend that agrees with known mathematical equations relating the carrier density n and gate voltage V_g on the one hand:

$$n = C_g(V_g - V_{CNP}) \tag{2.9}$$

and the carrier density and moiré wavelength λ (with λ given by Equation 2.8) on the other hand:

$$n = \frac{8}{\sqrt{3}\lambda^2}. \tag{2.10}$$

Thus this new approach to determine the angle θ allows more accurate measurements (uncertainty of less than ±0.1°), but is limited to a few degrees, i.e. only when the satellite resistance peaks are measurable.

The appearance of a linear variation in the magnitude of the satellite peak resistance (whereas the CNP peak shows no linear behavior) is a completely new observation and the origin of that linear dependence is still unknown. This constitutes a good example of how varying the rotation in a single sample allows to detect phenomena that were obscured in the previous sample-to-sample studies.

2.6 BLG-hBN heterostructures

2.6.1 Simulations

Considerably fewer studies can be found in literature about the moiré effect in BLG-hBN systems at small twist angle than about MLG-hBN systems. However, the expected band structure of BLG stacked on hBN (at zero-angle) has already been simulated [47, 48], as shown on Figure 2.18.

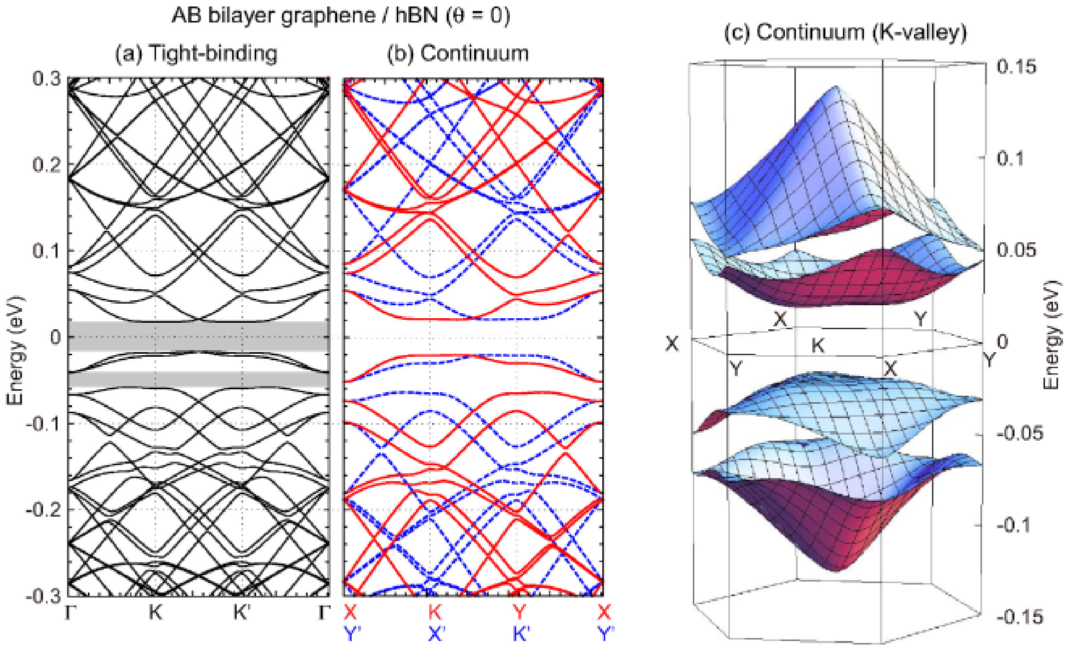

Figure 2.18: Band structures of AB-bilayer graphene / hBN system with θ = 0° calculated by (a) the tight-binding model and (b) a continuum model, on the K-space path (c) Three-dimensional plot of the first and second electron and hole bands of K-valley (continuum model) [47].

A few strong differences with the band structure of graphene-hBN emerge. There is a relatively large band gap ($\sim$ 40 meV) at zero energy and flat band edges, due to the interlayer potential difference (some moiré potential terms are expected to act only on one layer of graphene). Moreover, due to the special characteristics of BLG mentioned in section 2.2, the width of that gap should naturally vary under application of a gate electric field, or other electrostatic environment changes.
A band gap is also expected between the first and second band (at secondary Dirac points), due to the inversion symmetry breaking. This gap is larger on the hole side than on the electron side (same feature as in monolayer graphene-hBN).

2.6.2 Experimental signature of unconventional superconductivity

Recently, Moriyama *et al.* reported the observation of a superconductivity dome in the phase diagram of an hBN/BLG/hBN device, upon in situ electrostatic doping [2].

The findings of this study are still controverted and the article has not been published yet (at the moment of writing this master thesis). The results are indeed surprising: a critical temperature of 14K was reported.

In the measured device, there is an approximate zero-angle alignment between the upper hBN layer and the BLG, and no fine tuning to a magic angle was necessary.
Figure 2.19-a shows the evolution of the longitudinal resistance (R_{xx}) as a function of the density n at different temperatures, and at zero magnetic field. A sudden drop around an "optimal doping" of $n = -3,48 \times 10^{12}\text{cm}^{-2}$ was observed. Secondary resistance peaks seem to appear, indicating the presence again of satellite Dirac points. Another signature appears in the magnetic spectrum: 2nd generation Landau fans.
Figure 2.19-b displays the evolution of the resistance as a function of the density n and the temperature (again at zero-magnetic field). A dome-shaped superconducting phase appears between $n \sim -3.2 \times 10^{12}\text{cm}^{-2}$ and $-3.6 \times 10^{12}\text{cm}^{-2}$ and the critical temperature of 14 K and saturates near the optimal doping of $-3,48 \times 10^{12}\text{cm}^{-2}$.

In case of confirmation of this discovery, a new class of superconducting family would arise. This represents a considerable step in the field, opening doors both in fundamental physics research and in development of applications such as quantum information devices.

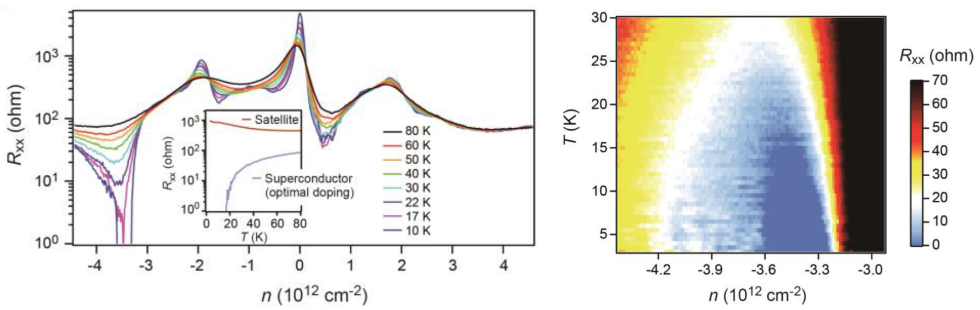

(a) (b)

Figure 2.19: (a) Longitudinal resistance R_{xx} of the device as a function of the density n at zero-magnetic field, for temperatures ranging between 10 K and 80 K. The inset shows the resistance as a function of the temperature T at the density corresponding to one of the satellite resistance peaks ($-1.93 \times 10^{12}\text{cm}^{-2}$), showing non-metallic behavior due to the bandgap, and at the "optimal doping" ($n = -3,48 \times 10^{12}\text{cm}^{-2}$), showing the superconducting behavior with the highest transition temperature. (b) Longitudinal resistance R_{xx} as a function of the density n and T (the temperature). The superconductivity dome is visible (blue-colored region). [2]

2.7 Motivations of this work

This work aims at investigating different properties described in this chapter in the case of a tunable moiré formed by a bilayer graphene and an hBN lattices.

The rotatable architecture presented in section 2.5 allows to dynamically rotate an hBN lattice over a graphitic surface, and different types of features can be probed: friction, Raman and electrical transport can be measured to determine and control the misalignment angle on one hand, and to study the particular properties of the superstructure on the other hand. The first objective will be to reach alignment of the layers and to control the rotational order by at least one of these techniques. In particular, the impact of the angle between the lattices crystalline orientation on those properties can be examined and compared with the case of monolayer graphene.

Besides, it would be most interesting to check whether the unconventional superconductivity measurements of Moriyama *et al.* can be reproduced in such a rotatable architecture, tuned near or at zero-degree alignment angle and cooled down at ultra low temperature.

Chapter 3

Fabrication process

This chapter details all the steps of the fabrication of the rotatable heterostructure, as well as the structural characterization techniques used during the fabrication process, and their results.

3.1 Device architecture

The heterostructure design, as well as the fabrication process were noticeably inspired by the one described in [42] (introduced in section 2.5). The aim is to obtain a Hall bar of Bernal-stack bilayer graphene (BLG) sandwiched between a flake of hBN and another layer of hBN, shaped in a wheel that can conveniently be rotated with an AFM tip.
The Hall bar shape is chosen to allow a wide range of electrical measurements.

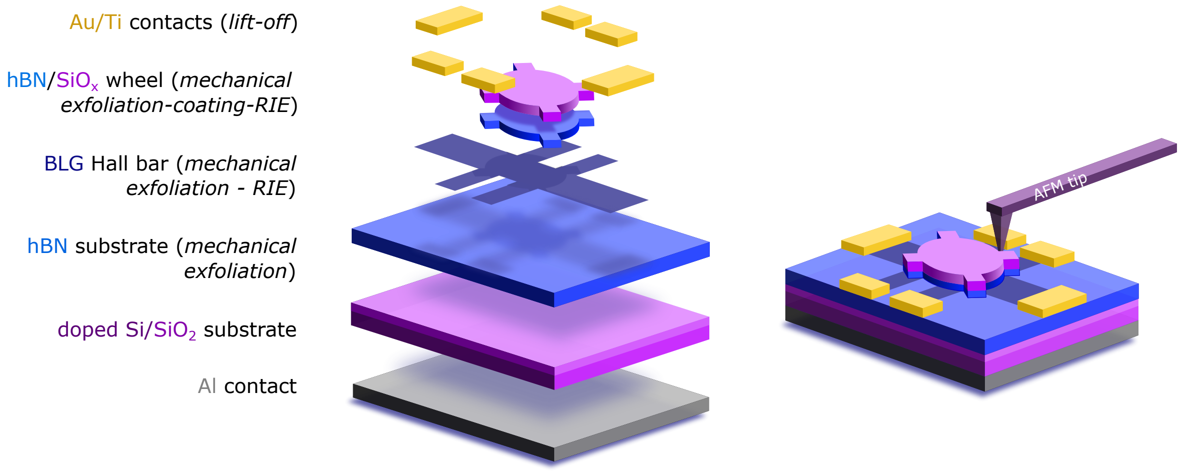

Figure 3.1: Schematic representation of the device structrure: exploded vue and experimental rotation technique (inspired by the scheme shown on Figure 2.13-A, from ref. [42])

Each layer of the vdW heterostructrure (BLG and hBN) is synthesized by mechanical exfoliation and transferred on a marked wafer especially provided for vdW heterostructure devices: the backgate is inherent to the wafer: it consists in a bulk of heavily P-doped Si contacted on the bottom with aluminum and topped by a 90 nm-thick SiO_2 layer that insulates it from the BLG.

The complete device architecture is represented on Figure 3.1.

3.2 Mechanical Exfoliation

3.2.1 Introduction to graphene films fabrication techniques

Many different techniques exist to create graphene for nanotechnologies, with different advantages and drawbacks making each of them more suited for different purposes. The main ones are chemical and mechanical exfoliation, Chemical vapor deposition (CVD), graphitization of SiC crystals, and epitaxy.

The most populars in the field of nanoelectronics are exfoliation and CVD.

CVD, that is more adapted for industrial production, allows to create large-area graphene and therefore, more flexible desired shapes, but its quality is limited by grain boundaries and processing-induced contamination. Indeed, CVD graphene needs to be grown on a specific substrate, usually metal (Cu, Ni, ...), and is strongly attached to it. Thereafter, in most cases it must be transferred and it is not easy to separate the grown layer of graphene without damaging its structure or alter its properties (the substrate is often dissolved in harmful acids, which affects the quality of the graphene). Nevertheless, CVD is continuously evolving and the ongoing developments of the technique seem promising for the future.

Although mechanical exfoliation is arduous and not scalable, to these days this technique yields the highest quality material, and remains the most suited for fundamental studies. Therefore, in this work, mechanical exfoliation was used, enabling higher electronic mobility and better overall electronic qualities to investigate the desired properties.

3.2.2 Working principle

Exfoliation working principle is well described in Ref. [4] (especially the supplementary materials document). It consists in the isolation of graphitic films of random thickness (i.e. number of layers) by repeatedly peeling flakes of graphite (or hBN) off using scotch tape, tearing appart different layers.
After that step very clean Si/SiO_2 wafers (of about 1x1 cm) are placed on the tape (on its SiO_2 side). These are then heated together at 90°C, in order to increase the adherence and contact area between the flakes and SiO_2, and finally the tape is peeled of the wafer. By doing this, a very big number of flakes are left on the substrate, but only very few will have the desired thickness (in this case, 2 layers) due to the randomness.

Presumably, thanks to van der Waals and/or capillary forces, thin flakes tend to remain attached to the SiO_2 substrate.
Exfoliation of hBN requires roughly the same steps, except that the heating step is not necessary and the thorough cleaning of the wafers is not mendatory.

In this work, the exfoliation process of graphene/graphite and hBN flakes was executed following the precise procedure described in more extensive details in the work of Alexis Warnier [49].

After exfoliating those flakes, observation with an optical microscope allows to identify, select, and reference potentially useful flakes. The color gives a good first idea of the thickness. Due to the high reflection at the Si/SiO_2 interface, and SiO_2 transparency, the colors perceived are a result of Fabry-Perrot interferences. Flakes appear in different colors as the added optical path shifts the interference colors. The thinnest flakes are quite transparent (1-2 layers) and thus appear violet, with some contrast to the violet background (graphene absorbs $\sim 2.3\%$ of the incident light [50]). Thicker graphitic films absorb more the light and shift progressively the color to darker violet, then blue or even white (very thick flakes) when the absorption becomes so high that the flake becomes opaque. Flakes obtained by exfoliation that are representative of these contrast and color observations are shown on Figure 3.2.
In the case of hBN, few-layers flakes are roughly never observed after exfoliation. Ideally, large blue flakes are chosen (at least larger than the targeted graphene flakes). The thickness of those flakes is then usually in the range of 20 to 50 nm. Flatness and thickness of the flakes can be checked by AFM imaging.

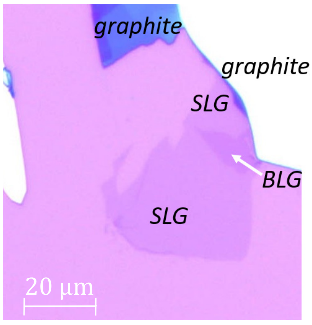

Figure 3.2: Optical microscope image of (exceptionally large) flakes obtained by mechanical exfoliation. Areas with single layer and bilayer graphene (SLG and BLG) can be identified, as well as multiple layers (graphite) of different thickness (the white areas are thicker than the blue areas).

After a first selection, by discrimination of the color and size (for the further fabrication steps, the flakes must be at least $\sim 7-10\ \mu m$ long) of the interesting flakes, the exact number of layers must be known with accuracy and certainty. For this purpose, Raman spectroscopy is used, as explained in the following section.

3.2.3 Raman spectroscopy intermediary characterization

Raman spectroscopy is a powerful chemical analysis tool that allows to measure a spectrum of the light scattered by a material, that provides a fingerprint of its chemical structure.
Identification of graphitic materials and its number of layers requires fast, non-destructive and high-resolution method. Raman spectroscopy has long been demonstrated to fulfill all these requirements [51] and is now commonly used for that purpose.

Raman spectroscopy can also provide valuable information on strain variations in graphene (or multilayer graphene), on the manometer-scale [52]. This is illustrated by the Raman analysis in Ref. [42] summarized in section 2.5, and in the work of Ref. [53], as explained in section 4.3.

Working principle

When a crystal is exposed to light, part of the photons are simply transmitted through it, and the other photons interact with the lattice through different absorption or scattering processes, in a unique way depending on the electronic and vibrational properties of the material. And those various phenomena (photoelectric effect, IR absorption, photoluminescence, scattering, etc.) occur in different ranges of photon energy.

Raman spectroscopy uses a monochromatic laser that radiates incident photons with a certain incident frequency ν_i on a spot of the sample. A part of light is scattered in all directions and most of the scattered photons are re-emitted with a scattering frequency $\nu_s = \nu_i$. This corresponds to elastic scattering called Rayleigh scattering. But in the case of a very small portion of the scattering events, the laser light interacts with phonons (or sometimes other excitations in the system) and the scattering frequency is different than the incident frequency $\nu_s \neq \nu_i$: these inelastic scattering events are called Raman scattering.

The scattering effects at stake in the case of the features measured in Raman spectroscopy in a crystal are described with more details hereafter.

In the visible range, a photon may be ”virtually” absorbed by a material: this means that the oscillating electric field of the photon just ”shakes” the electrons, exciting them to an intermediate state called ”virtual” state[1]. Those electrons will then scatter this energy back to another photon.
In the case where the incident and scattered photons have the same energy, the scattering process is elastic and is called Rayleigh scattering.
If, on the other hand, the ”shaking” of the electron causes vibrations of the atoms at their natural vibrational frequencies (thus generating or interacting with phonons), the scattered photon will have lost (gained) energy to (from) the vibration of the atoms. This scattering process is inelastic and can either create or absorb a phonon. This type

---

[1] a virtual state is a short-lived, unobservable quantum state and does not match with the eigenfunction of any operator. In contrast, after ”real” absorption, a photoexcited electron can be in the excited states for a sufficient time to allow measurement

of scattering phenomenon is named Raman scattering.
The characteristic vibrational modes of the lattice are called normal modes and are related to chemical and structural properties. As every material has a unique set of those normal modes, Raman spectroscopy allows to probe properties in detail and to provide an accurate characterization of Raman active phonon modes in a specific material [54].

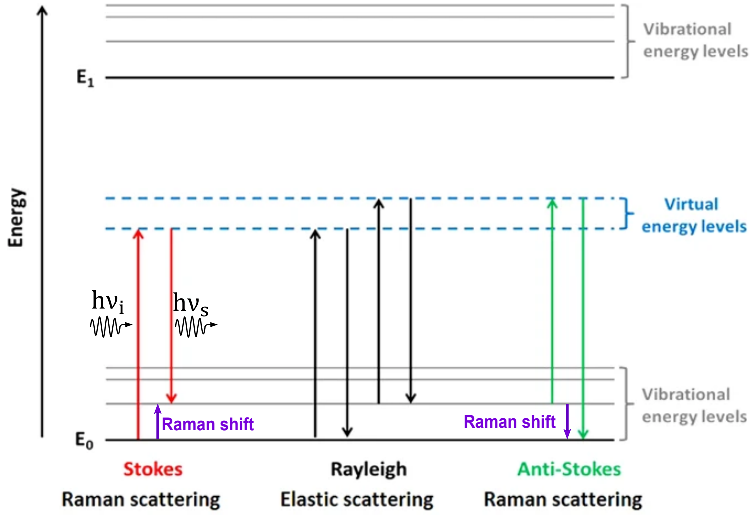

Figure 3.3: Diagram of energetic transitions involved in Raman scattering (adapted from [55]). Rayleigh scattering (black arrows) is elastic; the incident photon is of the same energy as the scattered photon. Raman scattering is inelastic; in Stokes scattering, the incident photon is of greater energy than the scattered photon, while in anti-Stokes scattering, the incident photon is of lower energy.

The scattering events in are commonly summarized in terms of energy transitions shown on the diagram on Figure 3.3.
However, as the laser excitation energies are usually much higher than the phonon energies in a crystal, light–matter interaction is mediated by electrons (although the exchange in energy between light and the medium is transferred to the atomic vibrations).

When the photon loses energy in creating a phonon the Raman scattering process is called Stokes process and when the photon gains energy by absorbing a phonon, it is called an anti-Stokes process (which is generally weaker than the Stokes process and temperature-dependent). By convention, the energy spectrum of the Stokes process is represented at positive energy while the anti-Stokes process occurs at a negative energy.

The Raman spectrometer detects the scattered light energy and and maps the energy transitions caused by Raman effect called Raman shift. This Raman shift is however displayed in units of cm^{-1} (wavenumber units) as phonon energies are usually too small a number to be displayed in nanometers, and moreover, the accuracy of common Raman spectrometers is on the order of 1 cm^{-1}:

$$\text{Raman Shift } \Delta\tilde{\nu}\,[\text{cm}^{-1}] = \left(\frac{1}{\lambda_i[\text{nm}]} - \frac{1}{\lambda_s[\text{nm}]}\right) \times \frac{[10^7\text{nm}]}{[\text{cm}]}$$

where λ_i is the wavelength of the incindent excitation laser, and λ_s is the wavelength of the scattered light.

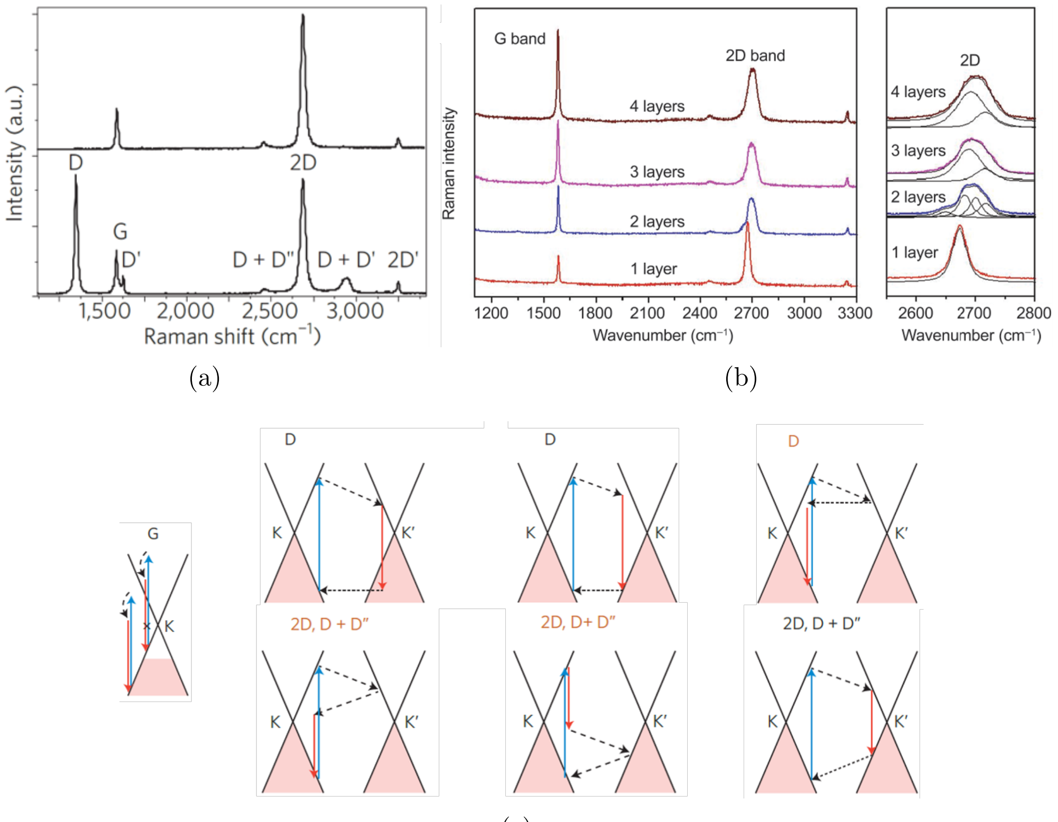

(a)

(b)

(c)

Figure 3.4: (a) Raman spectra of pristine (top) and defected (bottom) graphene, with the main peaks indicated by labels [56]. (b) Raman spectra of 1- to 4-layer graphene [57] (c) Representation of the Raman processes on the electronic dispesion diagram (solid black lines) for each of the main peaks [56]. The shaded areas represent the occupied electronic states, the electron transitions are represented by blue and red arrows respectively when accompanied by photon absorption or emission, dashed arrows when accompanied by phonon emission, horizontal dotted arrows when due to electron scattering on a defect. The processes indicated by the orange peak labels give a small contribution.

Figure 3.4-a allows to identify the different peaks (or "bands") appearing in the Raman spectrum of graphene, and more generally in graphitic systems. A few of those peaks are very useful to accurately identify the system (number of layers,...) and analyse different properties: the most important peaks that are examined in this work are the

D, G, D+D" and 2D peaks (the G and 2D peaks are the most prominent and are always present in the spectra of any graphitic systems).

To be able to perform this analysis, it is useful to understand the mechanisms of interaction between the electrons and the phonons of the system at the origin of each of these peaks. Figure 3.4-c shows the different interband and intraband transitions of the electrons on the electron dispersion diagram of graphene for each of the main Raman processes (D, G, D+D", 2D): transitions accompanied by photon absorption are represented by blue arrows, photon emission by red arrows, phonon emission by dashed arrows and electron scattering on a defect by horizontal dotted arrows.
This figure is very useful and representative because it shows both the transitions in energy and in momentum, and their conservation along the processes.

More information about each of these Raman processes is provided in Table 3.1. Properties such as resonance and the order of the Raman process are also important in their description.
Resonance Raman scattering (RRS) occurs when the laser energy matches the energy between optically allowed electronic transitions between an occupied initial state and an unoccupied final state. As a result, the probability for the scattering event to occur increases and thus the intensity of the signal is enhanced. The same happens if it is the energy of the scattered light that corresponds to an allowed electronic transition. The resonance effect is important in nano-scale systems because the Raman signal from nanomaterials is generally very weak. In Graphene, a lot of Raman processes are resonant (partly because there is no bandgap).
Furthermore, we talk about "double resonance" if, in addition to the electron-photon resonance, there is a phonon in the vibrational that can connect the two unoccupied conduction electronic states (this phonon scattering process will be resonant) [54].
The order of the Raman process represents the number of scattering events that are involved in the Raman process. Due to the symmetry of the hexagonal lattice, only one first order Raman band is allowed in graphene: the G-band.

Figure 3.4-b shows the differences arising in the Raman spectrum depending on the number of layers of few-layer graphene. The most remarkable difference resides in the shape of the 2D-peak, which reveals to be the most useful to probe the changes in layer stacking quite sensitively.
In bilayer graphene, the 2D peak is a convolution of 4 Lorentzian peaks (when in monolayer, the 2D peak is a single Lorentzian peak): P_{11}, P_{12}, P_{21} and P_{22} (also sometimes labeled $2D_{1A}$, $2D_{1B}$, $2D_{2A}$, $2D_{2B}$ in the literature) as shown on the right side of Figure 3.4-b and on Figure 3.7.
This is explained by the fact that in bilayer graphene, the π and $\pi^\star$ electronic bands are divided into four bands. The 2D Raman process relies on a double resonance process linking two phonons with opposite wave vector with the electronic band structure. The transition can thus occur following 4 possible combination of scatterings, respecting the double resonance condition, as illustrated on Figure 3.5 [56].

Each of those four possible transitions give birth to one of the Lorentzian peaks, with

Table 3.1: Characteristics and description of the four most important Raman peaks of single and multi-layer graphene (the included illustrations are from Ref. [56]).

	$\Delta\tilde{\nu}$ [cm^{-1}]	**Dispersion diagram**	**Vibrational mode**	**Order of the Raman process**	**Resonance**	**Description**
D-peak	1350	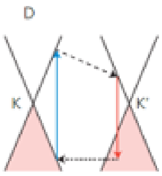	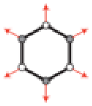	2nd order (1-phonon process)	Double resonance	The D-peak is the main peak that appears due to defects (symmetry-breaking effects). The presence and intensity of this peak is representative of the imperfections. It is due to breathing modes of 6-atoms rings (illustration) corresponding to transverse optical phonons around the Brillouin zone corner (K) [56].
G-peak	1580	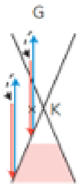	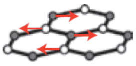	1st order (1-phonon process)	Single resonance	The G-peak is found in the Raman spectra of all graphitic systems. It is due to in-plane C–C bond stretching modes (high-frequency E2g phonon at Γ) and gives rise to both the optical in-plane transverse optic phonon and the longitudinal optical phonon branches. As the C–C bonding is strong and mass of the C atoms is small, the G-band shows a high Raman frequency with a sharp peak. It has the particularity to be a first-order process and one of the only ones to be not completely resonant [54].
D+D”-peak (or G*)	2450	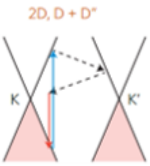	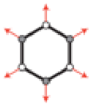	2nd order	Double resonance	The main contribution of this peak originates from so-called inner processes, i.e., phonons from the K direction (resonance processes occurs along the KΓ line). The D + D” peak is related to what is called a combination mode: it is due to the association of a phonon from the branch responsible for the D-peak and an acoustic phonon [58].
2D-peak (or G’)	2680		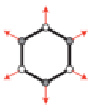	2nd order (2-phonon process)	Double resonance	The 2D-peak (also labeled G’-peak) is due to double resonance processes between the K and K’ point [54]. In this Raman process, momentum conservation is satisfied by two phonons with opposite wave vectors [56]. Thus, although it is related to an overtone of the D-peak with the same vibrational mode, no defects are required for the activation of 2D processes, and so they are always present in graphitic systems.

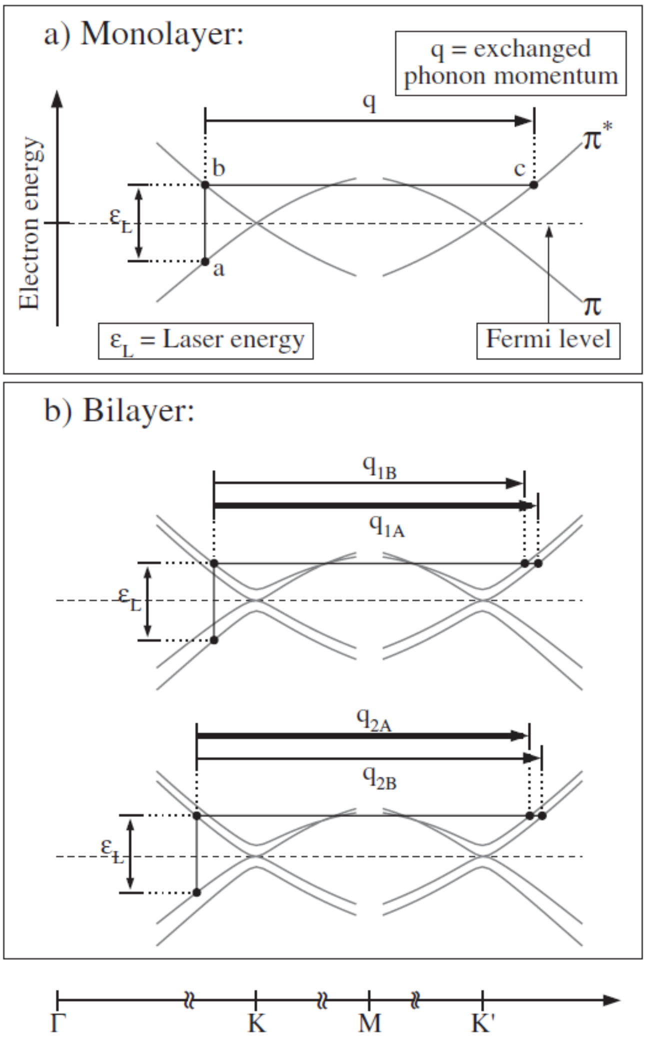

Figure 3.5: Possible electronic transitions in the 2D resonant Raman processes in monolayer (a) and in bilayer graphene (b) [51]. In monolayer graphene, the π and $\pi^\star$ bands allow for one set of resonant transitions, involving one type of phonon with a specific momentum q, and in bilayer graphene, because of the additional conduction and valence bands, 4 sets of resonant transitions are made possible involving different phonons with slightly different energy and momenta q_{1B}, q_{1A}, q_{2A}, and q_{2B}.

a slightly different Raman shift (as the photon emission is related to a slightly different electron energy loss).

Another difference is the shape of the D+D”-peak, which is less sharp and larger in bilayer than in monolayer graphene. The reason is similar to what was described for the 2D-peak: due to the additional electronic bands, additional scattering processes can occur involving different phonon wave vectors, resulting in sub-peaks at slightly diverging Raman shifts [58].

In the case of graphitic structures, 514, 532 and 633 nm lasers are commonly used as incident laser, and the 514 nm green laser is the most popular choice.

Measurements

Thin transparent flakes are thus exposed to the green laser (514 nm) and the Raman spectrum is measured. The number of layers can be easily identified looking mainly at the 2D-peak (and the D+D”-peak looks also larger and flatter in BLG as expected).

A typical and representative Raman measurement of a sample containing both monolayer and bilayer graphene is shown on Figure 3.6.

To illustrate the subpeaks of the 2D-band introduced previously, the spectrum of bilayer graphene portion can then be deconvoluted to identify clearly the four different peaks, as shown on Figure 3.7.

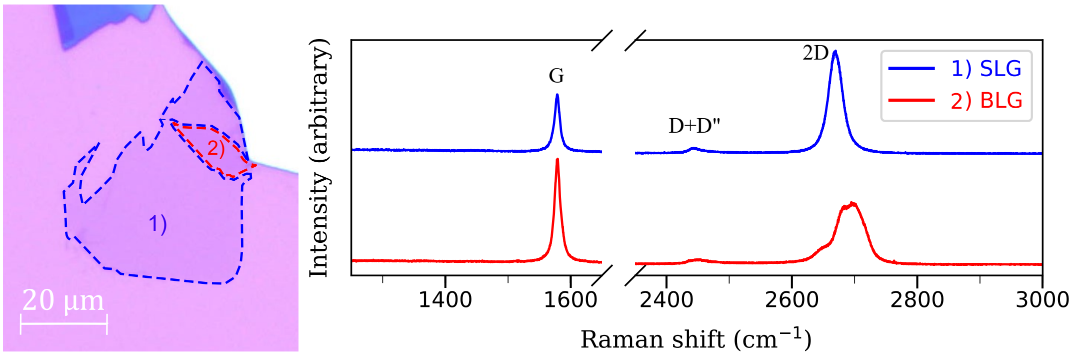

(a)

(b)

Figure 3.6: Raman spectra from one of the samples previously shown on Figure 3.2. (a) Optical image of the characterized flakes; the homogeneous areas inside which the Raman measurements were made are highlighted in blue and red dotted lines, and l. (b) Raman spectra measured for each area. The peaks on the blue curve (area 1) are typical of single layer graphene (SLG). The shape of the peaks on the red curve (area 2) are typical of Bernal-stack bilayer graphene (BLG).

Between the numerous flakes obtained by exfoliation, only a few were selected as potential candidates for the fabrication of heterostructures. Among those, 3 flakes shown on Figure 3.8 were confirmed to be bilayer graphene, with Raman measurement.

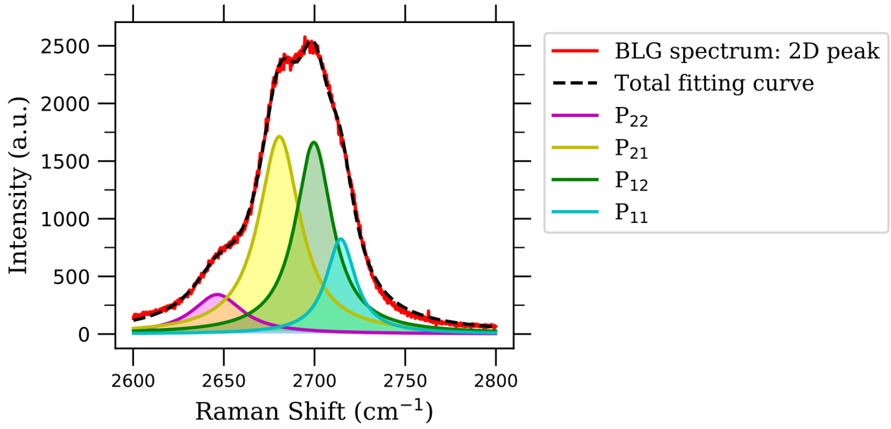

Figure 3.7: 2D peak in the Raman spectrum of the BLG flake area previously shown on Figure 3.6. The spectrum is fitted with 4 Lorentzian sub-peaks: P_{11}, P_{12}, P_{21} and P_{21}.

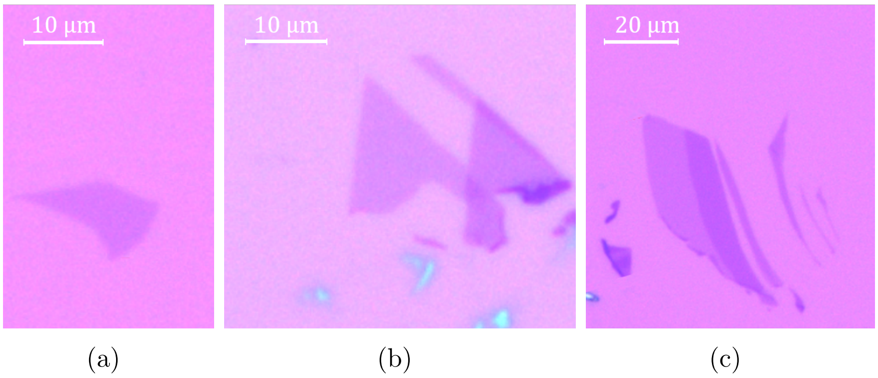

(a) (b) (c)

Figure 3.8: Optical microscope images of exploitable flakes of BLG, that where used in this work to fabricate samples, labeled later as (a) Sample 1, (b) 2, and (c) 3.

3.3 Dry transfer

The obtained and selected flakes of bilayer graphene and hBN must then be assembled in stacks. To stack the layers and obtain heterostructures, various wet and dry transfer methods for 2D materials have been explored [59]. Wet transfer methods means that the graphene films are put in contact with liquid solutions at some point of the process, which might cause more contamination. In addition, there is no way to obtain a precise and deterministic positioning of one flake with respect to another with the wet transfer method. Dry transfer is thus preferred here.

The mechanical assembly technique followed in this fabrication process is described in Ref. [60] (supplementary information).

Globally, the dry transfer method consists in picking flakes exfoliated on the SiO_2

substrates catching it on the surface of a (sticky) polymer film, e.g. a poly-propylene carbonate (PPC) film, allowing either to transport it to another substrate, or to repeat the picking process, taking advantage of the strong adhesion (due to vdW interactions) between hexagonal structures (hBN, graphene, BLG...) to pick a second different layer (by simple contact with the first one). This way, stacks with arbitrary numbers of layers can be assembled before placing the whole stack on the substrate as illustrated on Figure 3.9, and all this without exposing the interfaces to polymers.

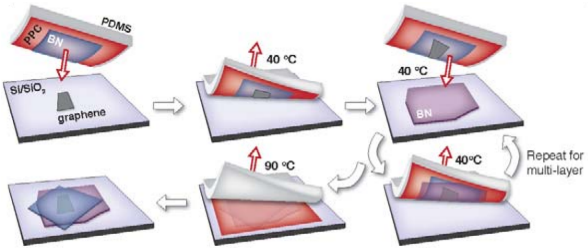

Figure 3.9: Step-by-step schematic diagram of the multiple-layer stack vdW heterostructure assembly technique [60].

3.3.1 Tools

Transfer slides

In order to pick and stick the flakes from the substrate and stack it or transfer it elsewhere, transfer slides are used. These are made of:

- a microscope slide;
- a cubic ($\sim$ 1.5x1.5x1.5 mm) transparent elastomer stamp made of polydimethyl siloxane (PDMS);
- a transparent tape: to fix the PDMS stamp on the microscope slide and to obtain a bump shape (more efficient during the picking process);
- a circular PPC thin film ($\sim$ 1 μm thin) attached on another piece of tape, that was punctured beforehead to support the latter PPC film.

The PPC film is created by spin-coating two drops of a solution PPC (15%) dissolved in anisole (85%) at 2000 rpm during 1 min on a clean Si/SiO$_2$ wafer ($\sim$ 1 x 1 cm). The wafer is then heated to $\sim$ 100 to 120 °C, evaporating the anisole. Then the obtained polymer film is picked up with the punctured tape and attached on top of the slide (a PDMS square attached with transparent tape on a microscope slide).

A cross-sectional view of the transfer slide is shown on Figure 3.10.

Transfer table setup

The transfer table is equipped with micromanipulators and a temperature controller (in addition to an efficient heating/cooling system). It allows thus to manipulate the

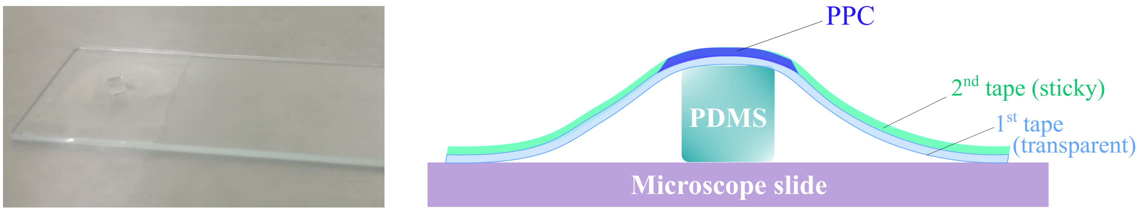

(a)

(b)

Figure 3.10: (a) Picture of a transfer slide. (b) Schematic representation of the transfer slide.

transfer slide (and the wafer) with precision under the microscope (enabling for instance to align flakes on the PPC with a flake on the wafer) and to heat and cool the sample on demand, in order to modify the state and consistency of the PPC when it is put into contact. A schematic representation of that tool is provided on Figure 3.11.

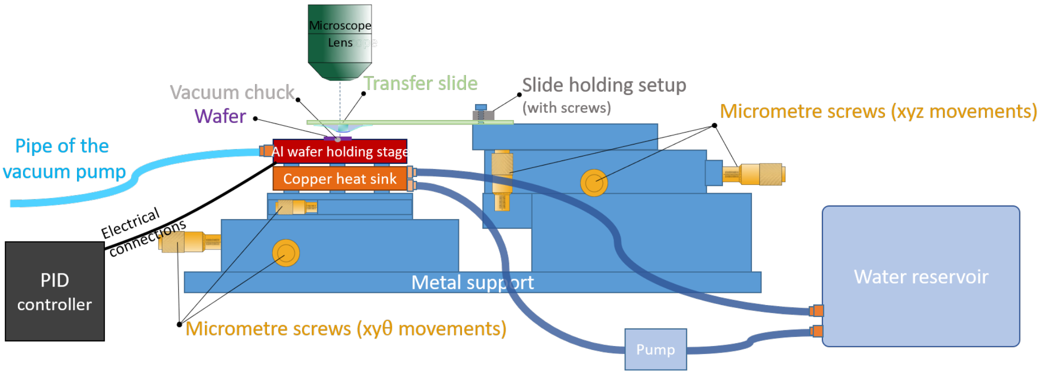

Figure 3.11: Schematic representation of the transfer table setup.

The wafer is held on an aluminum stage and is maintained and immobilized with the help of a vacuum chuck in the middle of the stage (which thus need to be connected to a vacuum pump). The stage can be heated or cooled thanks to the Peltier heater and cooler hidden between the aluminium stage and the copper disk. Thanks to the low density and relatively high thermal conductivity of aluminum, the stage conducts the heat very fast and efficiently. The stage also contains temperature sensors. Thanks to the PID controller, the temperature of the stage (and of anything put in contact with it) can thus be regulated. In order to measure and implement an absolute temperature value (Peltier devices only work with temperature differences), the copper heat sink is maintained to room temperature, with the help of a water cooling system.

The transfer slide is held above the wafer and below the microscope. It is entirely composed of transparent materials, so that every flake manipulated (on the wafer or on the PPC) are visible under the microscope.
Micrometer screws allow to move precisely both the transfer slide, and the stage supporting the sample. The latter can also be rotated, which also allows to adjust the twist angle at the first stacking step by misaligning the natural edges of the flakes for

instance.

3.3.2 Transfer procedure and steps

The whole procedure followed in this work to obtain the hBN/BLG stacks is illustrated on Figure 3.12.

The first step is to pick the first hBN flake on the transfer slide: the PPC is aligned above the flake with the micrometer screws, and progressively lowered until the first contact to the wafer (which appears randomly in the area of the PDMS square, near the flake). The contact zone is then expanded by increasing the temperature (to ~ 40°C), softening the PPC. When the contact zone covers the targeted flake, temperature is lowered (to a temperature between ~ 5 and 20°C) to firm up the PPC. Then the slide is lifted up very slowly and delicately. If the flake has been well caught on the PPC with sufficient adhesion, the flake is pulled away from the substrate.

The second step is to pick up the graphene flake on the hBN flake. The hBN flake still on the transfer slide can first be aligned with a certain accuracy above the graphene flake, thanks to the micrometer screws. Then they are put into contact, following the same procedure as in the first step (heating, cooling, and lifting...). Thanks to the vdW interactions, the graphene flake remains attached to the hBN flake, and again, if the adhesion between hBN and the PPC is sufficiently strong (stronger than the adhesion of the BLG to the substrate), the stack is lifted up with the transfer slide.

After assembling the stack, the latter must be dropped on a clean Si/SiO$_2$ wafer (a marked wafer is preferred, in order to perform lithography later in the process, and in this case, the wafer also contains the backgate of the device). Two methods are possible, depending on the desired orientation of the stack: stack-flip, which is the method used in this case, and direct contact, that will be useful later, when transfer the hBN wheel. The two methods make use of the fact that PPC heated to 100°C and put into contact with a substrate melts and sticks to that substrate.

- Stack flip allows to put the first flake picked (hBN) in contact with the substrate and the last flake picked (graphene) on top and facing upwards. This is done by peeling the upper tape supporting the PPC on which lies the stack of flakes, then sticking the tape on the marked wafer so that the stack is facing upwards and heating to 100°to stick the PPC against the substrate. The tape is then cut appart and removed, leaving the stack on top of a PPC large layer, on top of the marked wafer. The wafer was then heated to 350°C during 2 hours ideally under vacuum. In absence of the right equipment, the samples were put in RTA (Rapid Thermal Annealing) system instead, under H$_2$/Ar atmosphere. The stack-flip step is illustrated on Figure 3.12-c, d, e and f.
- With the second method, the first flake picked ends up on the top of the stack. The method is simpler: using the transfer table, the PPC transfer slide is directly put into contact with the marked wafer and the whole assembly is heated to 100°C, thanks to the transfer table Peltier heater. Then, when lifting up the slide, the

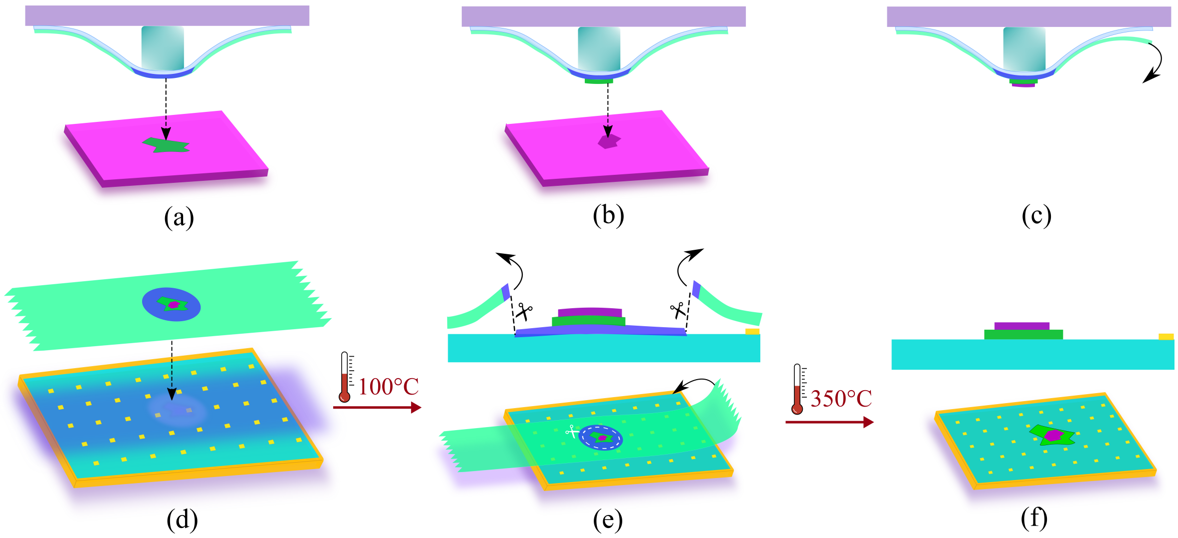

Figure 3.12: Step-by-step representation of the stacking procedure of a graphene flake over hBN. (a) An hBN flake is picked with the transfer slide. (b) Taking advantage of vdW interactions, the graphene flake is picked with the hBN flake. (c) The upper tape supporting the PPC (on which sticks the stack of flakes) is peeled off. (d) Stack flip: the tape is positioned on the marked wafer so that the graphene flake is facing upward and heated to 100°to stick the PPC against the substrate. (e) The outlines of the PPC film are cut and the tape is pealed and removed from the structure. (f) The PPC is evaporated by heating to a temperature of 350°C during 2 hours (ideally under vaccuum, or in H_2/Ar atmosphere). Note that the spacial scales used in these drawings are not representative of the real dimensions of the different objects represented.

melted PPC sticks and remains on the wafer, with the stack underneath. (This was illustrated on Figure 3.9. Other illustrations in section 3.5.2 on Figure 3.27.)

On Figure 3.13, a few optical images of the steps of the procedure described above illustrate the process.

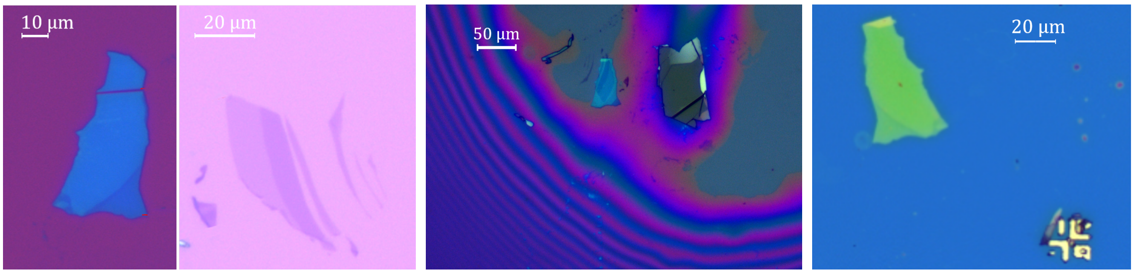

(a) (b) (c)

Figure 3.13: Optical microscope images of Sample 3. (a) The h-BN flake (on the left) and the BLG flake (on the right) before picking and stacking. (b) Image taken during the stacking of the two flakes, while the PPC is put into contact with the wafer. The contact zone (yellow zone) is expanding as the wafer is heated. The BLG is visible through the hBN flake. (c) Stack after transfer on the marked wafer.

More details about the same specific transfer slides fabrication, transfer table components, and picking process are provided in the work of Alexis Warnier [49].

Note that the transfer process may be at the origin of impurities or structural defects such as wrinkle formation or graphene tearing which impact graphene's integrity, properties, and performances [61].

3.3.3 Results: AFM imaging

Once stacked the BLG flakes are not really visible anymore on the optical microscope as seen on Figure 3.13-c. But the stacks can be better characterized using AFM imaging.

Tapping mode: Working principle

The use of an AFM equipment in tapping mode allows for very high resolution scanning probe imaging.
AFM imaging is generally based on using the interactions between a sharp tip and the surface of the sample to probe different properties; most often the topography is measured by probing the interaction force between the atoms of the very end of the probe and the atoms at the sample surface. The AFM equipment includes a cantilever at the end of which the sharp tip is suspended. Deflections of this cantilever (e.g. caused by interaction forces) are measured thanks to a laser beam focused on the extremity of the cantilever (on its back) and reflected on a four-quadrant photodetector (see Figure 3.14).

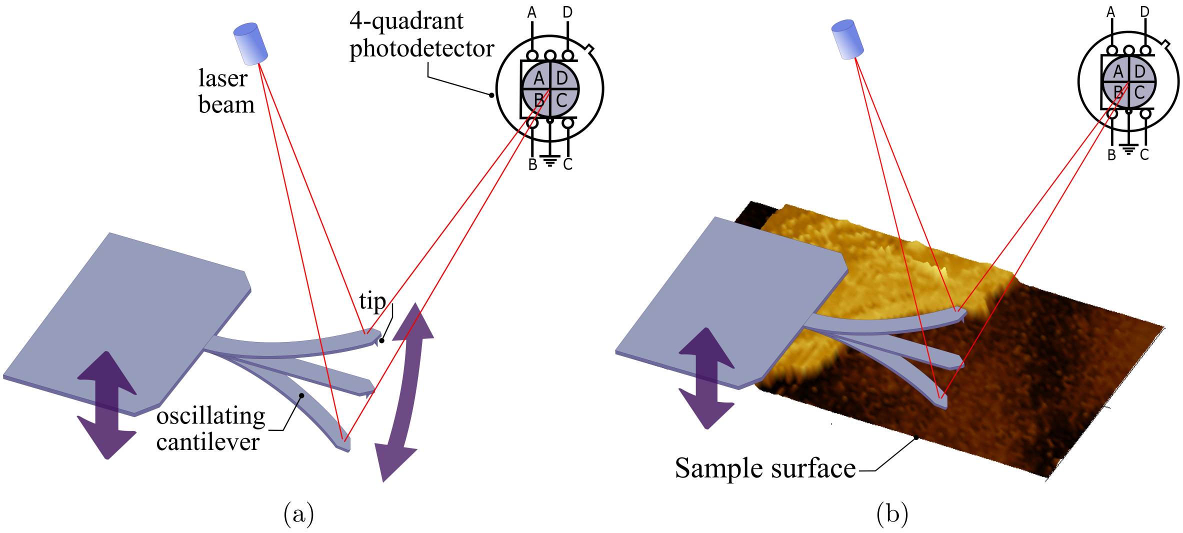

(a) (b)

Figure 3.14: Schematic representation of the AFM cantilever (a) Cantilever oscillating in free air at its resonance frequency. The laser beam reflected on the cantilever feeds a return signal to the four-quadrant photodiode (regular pattern in that case). (b) Cantilever tapping on a sample surface (the return signal is modified, depending on the topography).

In tapping mode, the tip is brought near the sample surface, while the cantilever is maintained in oscillation at its resonance frequency, thanks to a small piezoelectric bimorph in the cantilever holder. As long as there is no interaction with the surface, the amplitude of the cantilever oscillations is thus constant. But when the tip is close enough to the surface, interaction forces (Van der Waals, dipole-dipole, electrostatic forces, etc.) impact the oscillations and modify the amplitude and frequency of the tapping, and the signal measured on the photodetector can thus be converted into height measurement (Figure 3.14). While scanning, the height of the cantilever is adjusted to maintain a set oscillation amplitude.

At the same time, the phase-shift of the oscillation can be recorded as well, reflecting the energy dissipated by the cantilever during each cycle and providing simultaneously surface topography and other surface properties (elasticity, viscoelasticity, adhesion, stiffness...).

Results

Figure 3.15 to 3.18 show AFM images of the 3 stacks presented previously (labeled Sample 1 to 3). More AFM images can also be seen in Appendix A

These images make the BLG flakes much more visible than in optical microscope images, particularly in phase images. Thanks to the AFM, some of the defects of the stacks are made visible (especially wrinkles), and the height of the stacks can be measured (the hBN flakes in particular). In Sample 1 and 2, the hBN flakes are $\sim$ 40 nm high

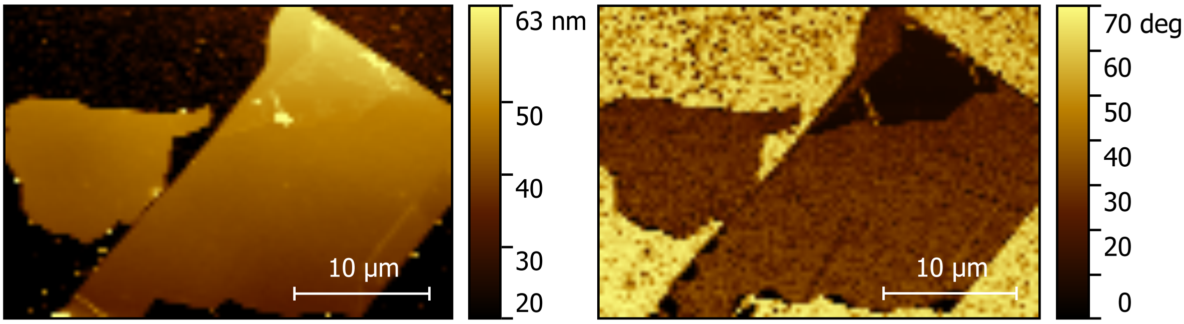

(a) (b)

Figure 3.15: Tapping AFM image of Sample 1. (a) Topography. (b) Phase.

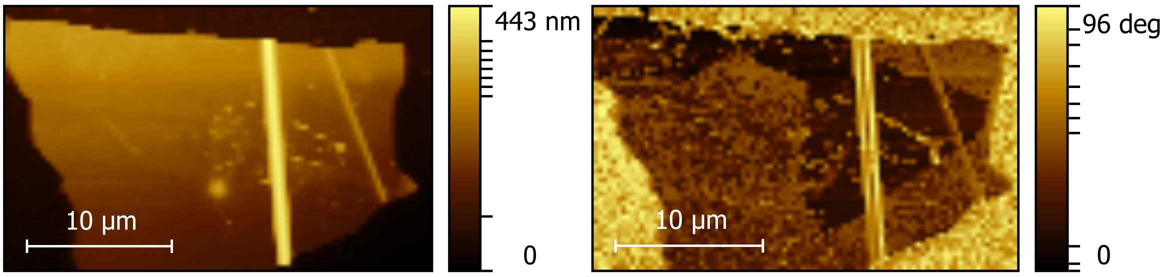

(a)

Figure 3.16: Tapping AFM image of Sample 2. (a) Topography. (b) Phase.

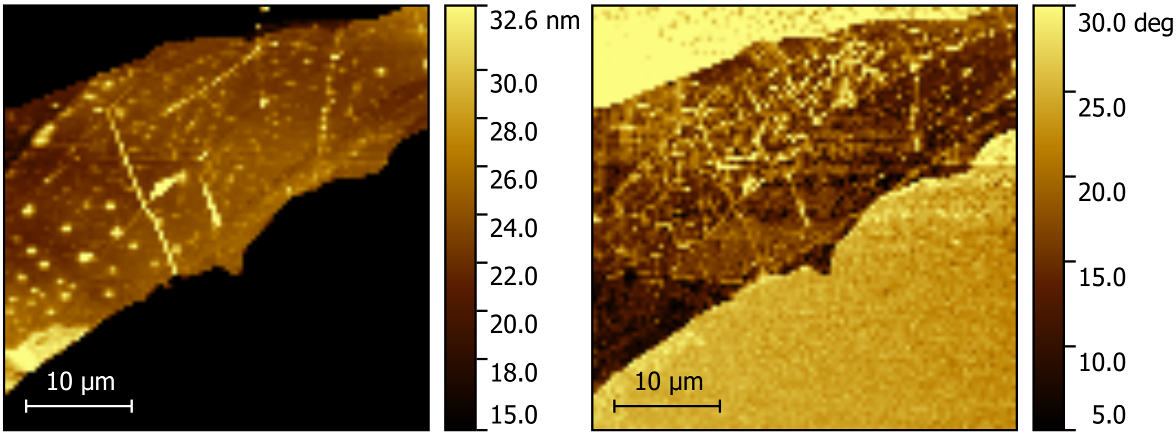

(a)

Figure 3.17: Tapping AFM image of Sample 3. (a) Topography. (b) Phase.

(distance between the SiO_2 surface and the top of the flakes) and 20 nm in the case of Sample 3 (the chosen flake is quite thinner - the AFM thickness profile can be seen in the Appendices). Note however that this is not strictly speaking the hBN thickness: the measurement of hBN lying on SiO_2 will always lead to larger dimensions than if

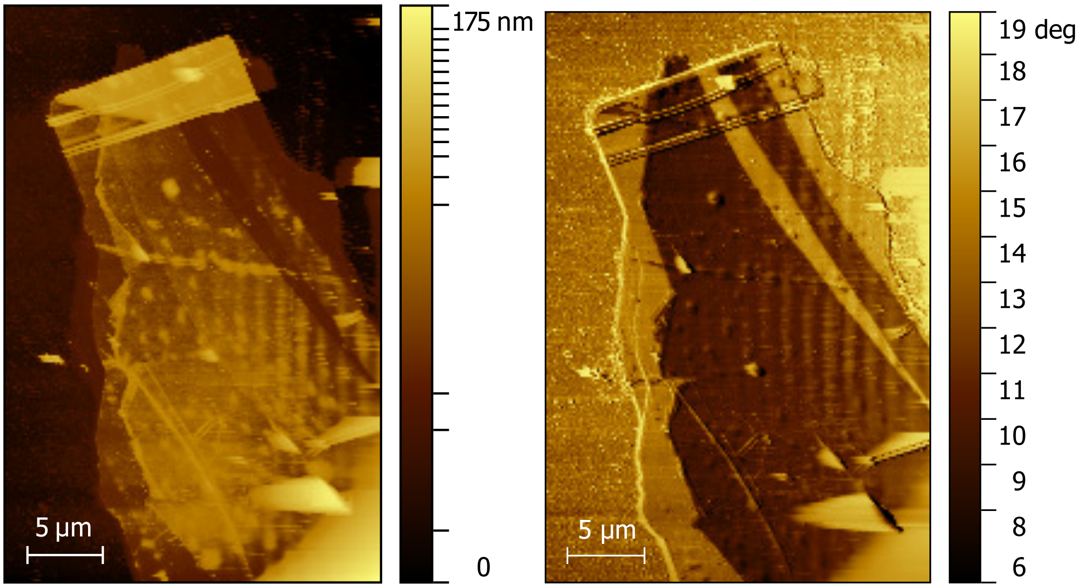

(a) (b)

Figure 3.18: Tapping AFM image of Sample 3 after a supplementary cleaning. (a) Topography. (b) Phase.

the hBN flake was stacked on hBN, because of the different kind of interaction between the surfaces.

In the case of Sample 1, the useful area of BLG is quite reduced because of stacking difficulties, and because of wrinkles or irregularities in the sample.
In Sample 2, the stacking was quite arduous and also caused the apparition of particularly big wrinkles in hBN and thus in graphene. The largest wrinkle crosses the BLG flake right in its middle.
In Sample 3, many small wrinkles appear on the sample, but these do not disqualify the sample for further experiments. Taking a look at Figure 3.17, the graphene is not very visible, porbably partly because of AFM-related issues (parameters, probe, ...), but also because there seemed to be a significant amount of impurities remaining on the surface: for instance remaining PPC from the transfer step. After using the RTA again to evaporate the remaining amount of PPC (2h at 350°C), the sample was imaged again (Figure 3.18) with higher resolution (longer scan). This also illustrates the role of the heating step on graphene wrinkles.

In the end, it appears from this characterization, that Sample 2 won't be of any further use in the frame of this study, because of the prominence of wrinkles, particularly in hBN.

3.4 Patterning and contacting

Two different strategies can be followed:

- First, the BLG Hall bar is etched, then the metallic contacts are patterned (that was the strategy tested for Sample 1).
- The metallic contacts are first deposited, then the BLG Hall bar is etched.

The most ”standard” way of working, which is the one followed in ref. [42], is the first one (presented for the case of Sample 1), which is why the steps are introduced in this order in this work. However, this process is quite flexible and can naturally be adapted. The choice made for Sample 3 to change the order of the steps was intended to fix alignment issues encountered with the lithography step.

3.4.1 Electron beam lithography

At this point of the fabrication process, a lithography step is needed to pattern the desired final features in the material of interest: the BLG Hall bar. Electron beam lithography is the most suitable choice for that purpose, as it allows to create on-demand shapes and dimensions with high resolution.

Working principle

Lithography is the fundamental process of transferring a geometric shape from a design to a thin layer of radiation sensitive material called resist which is covering the surface of the wafer.

The procedure steps can be summarized as follows. First, the substrate is coated with a thin film of resist: a polymer sensitive to electron radiations. The coating of the layer must grant a very controlled and uniform thickness over the substrate surface, spin-coating is generally used. Some pre-baking is done to remove excess solvent and to dry the resist.
Then comes the essential step: the resist exposure. An electron beam is scanned over the surface, exposing areas of the resist, thereby writing the pattern. Those exposed areas of resist are chemically modified, either reinforcing (in the case of a ”negative” resist) or weakening/breaking (in the case of a ”positive” resist) the chemical bonds. Development consists in immersing the wafer in a chemical bath that dissolves the parts of the resist that have not been polymerized or whose bonds have been weakened by the exposure.
Then to produce the final features in the material of interest, these resist patterns must be transferred once more by etching that selectively removes unmasked portions of a layer, or by lift-off (these steps will be described later).
At the end, the resist is generally not used anymore and can be removed by a so-called stripping process in solvents.

Process

The different steps of the process are presented on Figure 3.19, comprising the necessary preparation steps before the lithography, and the etching step after lithography allowing to obtain the Hall bar.

The main steps are spin-coating and baking, Electron Beam Lithography, development, Reactive Ion Etching, and resist stripping.

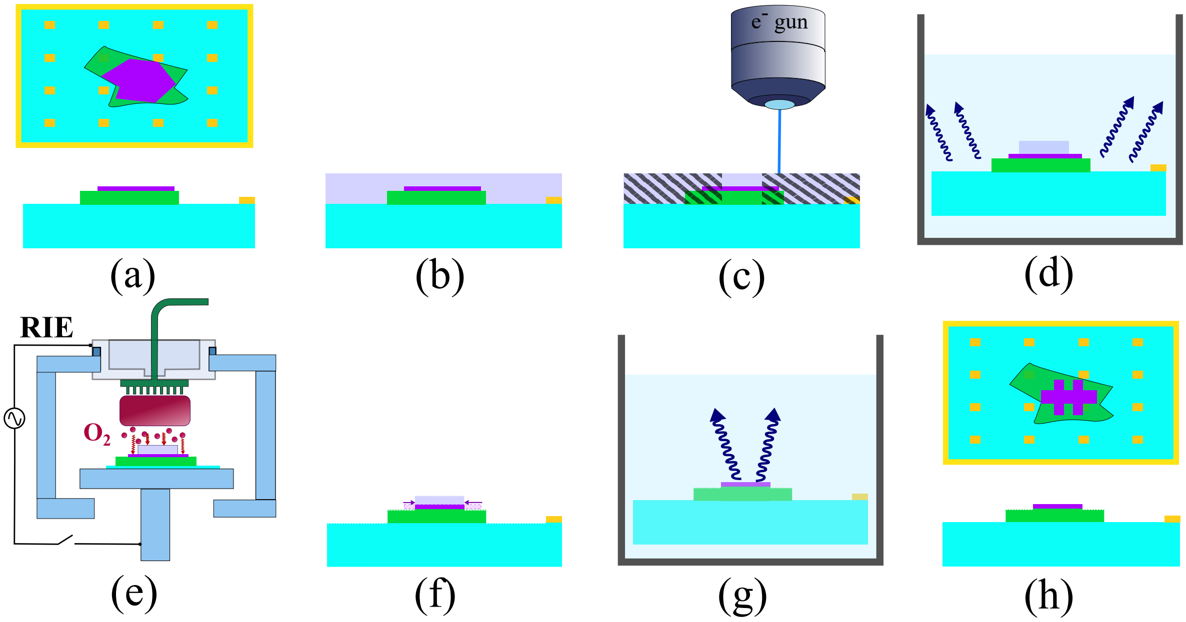

Figure 3.19: (a) The stack transferred on a marked wafer can be precisely located for accurate lithography. (b) A PPMA resist is spin-coated over the whole surface of the wafer and baked to evaporate the solvent. (c) The electron beam scans the PMMA surface, on all the spots that have to be removed, leaving un the areas where graphene must be preserved. (d) Development: the exposed, weakened resist areas are removed by dissolution in MIBK. (e) The stack is exposed to an oxygen plasma and (f) areas of graphene are removed by Reactive Ion Etching. (g) The remaining PMMA is removed in acetone. (h) The shaping of the BLG Hall bar is completed.

Preparation

Before anything else, one must precisely locate the stack by imaging it with the Scanning Electron Microscope (SEM)[2], using the gold marks on the wafer, as reference coordinates. This way, the negative of the Hall bar is drawn in a CAD file, in such a way that it is adapted to the position and shape of the flake.

The second step is to obtain a uniform layer of PMMA resist on the sample, with the right controlled thickness. As the RIE etching will also etch the PMMA layer (generally around 100 nm), the thickness of PMMA must be sufficient to prevent the whole PMMA thickness to be removed and ensure the protected areas to remain intact. The targeted thickness must be at least more than 150 nm, as the stacks are between 20 and 50 nm thick (measured with the AFM). The thickness of PMMA depends on the concentration of the solution used (PMMA is generally dissolved in anysole) and the spin-speed[3]. A

---

[2] the same apparatus will be used for the electron beam exposition

[3] Thickness vs. spin speed calibration curves are used to choose the right parameters.

4% PMMA solution was spin-coated at 4000 rpm. These parameters are known to yield a thickness of 219 nm.

The anysole is then evaporated by putting the wafer in an oven at 150°C for 15 min, leaving only the PMMA layer.

Exposure

The sample now ready for exposure can be placed in the SEM equipment (model: FEG XL30 (FEI)). The chamber is put under high vacuum (pressure of the order of 10^{-6} mbarr).

After alignment with the gold marks used as reference again (and taking care of not exposing the stack with the beam during this alignment), the exposure can be launched.

The beam current is fixed at 118 pA (which, for a certain aperture, corresponds to a certain beam size - a few nm) and the acceleration voltage is 30kV. A first test was made on an empty area of a wafer for calibration of the beam dose (the result is shown on Figure 3.20). Indeed, parameters such as the beam energy and the dose affect a lot the way electrons undergo forward scattering and back-scattering.
If the dose is too large, the resist risks to be overexposed: too many scattered, back-scattered and secondary electrons interact with the resist and too much PMMA is removed (for instance on Figure 3.20-f, the resist is so overexposed that there is no Hall bar left). If the dose is too low, at high acceleration voltage the electrons mostly penetrate through the resist with little interaction and scatter in a large volume and thus interact less with the resist than with the substrate. So the resist might be not completely removed in areas where it should be, because of insufficient electron interactions.

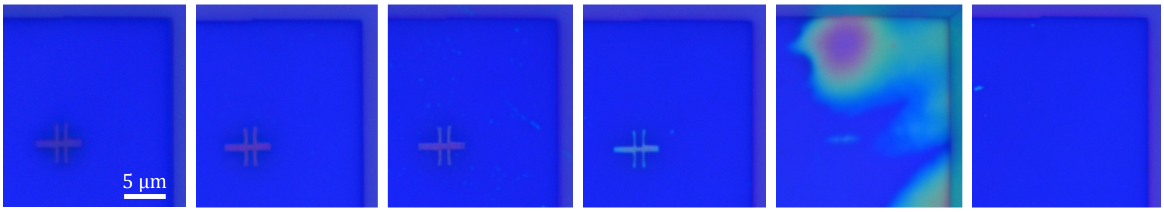

(a) (b) (c) (d) (e) (f)

Figure 3.20: Optical microscope images of a wafer on which lithography was tested for doses of (a) 125 µC/cm^2, (b) 150 µC/cm^2, (c) 175 µC/cm^2, (d) 200 µC/cm^2, (e) 225 µC/cm^2, and (f) 250 µC/cm^2. The wafer was coated with $\sim$ 200 nm of PMMA, different areas were exposed to the different doses of electron-beam, and developed in MIBK/IPA.

It appeared from the test that the ideal dose in this configuration is between 150 and 175 µC/cm^2. The samples are thus exposed with a dose of 160 µC/cm^2.

Development

After exposure, the sample is immersed in a Methyl isobutyl ketone (MIBK)/isopropanol solution for 1 min 30 sec. Only the exposed areas of PMMA, weakened by the electron beam, are made soluble in this solvent, and the unexposed PMMA will remain intact. The sample can be washed then in isopropanol to remove remaining traces of MIBK.

After that, in order to know if the lithography step should be started over or if the process can continue, the result (a Hall bar carved in PMMA) can be checked with the microscope, although the BLG flake is usually not visible.

3.4.2 Reactive ion etching

Now that a PMMA ”stencil” lies on the BLG flake, the latter must be etched to take its shape. Single or multi-layer graphene structures and devices are commonly etched using reactive ion etching (RIE) with O_2 or Ar gas plasma.

Working principle

Dry etching consists in using molecules in the gas phase, i.e. the ”dry” medium, typically in low or medium vacuum. The gas can become a reactive gas when brought to the plasma state.

The plasma is generated by a strong RF (radio frequency) electromagnetic field that ionizes the gas molecules, withdrawing electrons. Those electrons are accelerated up and down at each cycle of the RF field, while ions (that are more massive) move little in response to the electric field. The walls of the chamber are grounded so that electrons absorbed on it are ineffective, but the wafer platter isolated so that it builds up negative charge progressively as electrons are deposited on it, developing a large negative voltage. The plasma on the other hand is dominated by positively charged ions.
The voltage difference results in positive ions drifting towards the platter, and colliding with the sample. Ions can either react chemically with the compounds to etch or simply physically sputter material by transferring kinetic energy during the impact.

In the case of oxygen, atomic oxygen free radicals are formed in the plasma region and collide on the sample surface. These are very chemically reactive to carbon-based materials. The BLG flake will thus selectively be etched, much more than the hBN.

In the case of an inert gas such as Ar, there is no chemical reaction. However, negative voltage bias is applied to the wafer, Ar^+ ions are accelerated towards the wafer and remove matter by physical impact. The mask and BN substrate would be exposed to the physical impact and would be consumed.

In the case of this fabrication process, oxygen plasma is thus used.

Parameters

The samples are placed in the RIE chamber (Oxford Plasmalab 100 ICP RIE) and the pressure is lowered to 20 mTorr. 50 sccm of O_2 RF plasma is generated for 30 s at a power of 30 W.

3.4.3 Contacting

PVD of Ti/Au contacts and lift-off The metallic contacts are added on the leads of the Hall bar through a lift-off process.

These contacts are made of a 80 nm layer of gold, which is chosen because of its numerous qualities: resistance to oxidation, good conductivity, durability, heat resistance etc. However, gold adheres poorly to SiO_2 substrates. A 5 nm thick layer of titanium is thus added as an adhesion promoter between SiO_2 and gold.

Drops of PMMA solution are first spin-coated on the wafer (PMMA 7% at 5000 rpm, yielding a 590 nm thick film) and heated at 150°C during 15 min in the oven (to evaporate anisole). This time, the PMMA will serve as a sacrificial layer.

Then, areas of the PMMA film where the contacts will be placed are removed again using e-beam lithography and development (with an e-beam current of 180 pA and a dose of 260 $\mu C/cm^2$. Contact-shaped grooves are carved in the layer with vertical edges (or even tapered angle).

Titanium and gold are then deposited using electron beam evaporation. This deposition technique creates a very directional vertical flux of metal, ensuring uniform deposition only on the raised (PMMA surface) and recessed regions (grooves) of relief, but nothing is deposited on the vertical edges.

The remaining sacrificial PMMA is removed in acetone, taking away with it the areas of metal that were deposited on it.
In the end, only the metallic contacts remain where they were intended in the lithography drawing.

Schematical cross-sectionnal views of the sample between each of the important steps of the lift-off are shown on Figure 3.21.

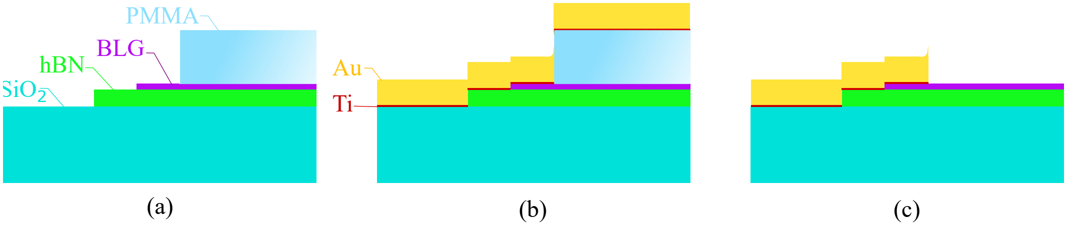

Figure 3.21: Schematical cross-sectionnal views of the sample (a) after lithography and development of the PMMA film, (b) after metallization: Ti(5 nm)/Au(80 nm), (c) after removal in acetone.

3.4.4 Results

The best way to check the result of the etching step is again to image the samples with an AFM. The BLG hall bar can be visualized both with topographic and phase imaging.

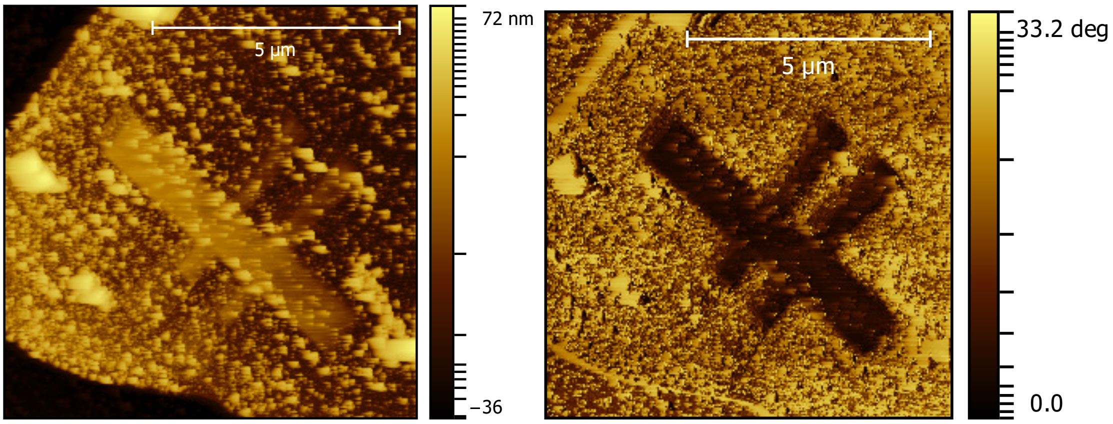

(a)

(b)

Figure 3.22: (a) Topographic and (b) phase AFM image of Sample 1, after etching the BLG Hall bar.

In the case of Sample 1, lots of misalignment issues were encountered with the lithography, ending up in a not very adequate result. As the Hall bar is very small, with little space between the leads to contact, and taking into account the misalignment troubles, it appeared that it wouldn't be possible, with the available SEM equipment, to obtain well aligned metallic contacts. Furthermore, it also appeared quite complicated to transfer a very small hBN wheel on the sample (the Hall bar being invisible under an optical microscope).

Thus for the rest of this study, only Sample 3, shown on Figure 3.23, is used in the following experiments. As the flake was large enough, the misalignment issues did not impact too much the device fabrication (also, the alignment technique was a little bit improved). The figure shows the successful etching (and lift-off) result, although some of the wrinkles (also seen earlier) might be problematic for experimentation. Fortunately, those were quite attenuated later, after heating the sample in an oven under vacuum at 360°C for cleaning. As shown on Figure 3.24, as a result not only did lot of the polymer residues disappear, but it seems that the wrinkles relaxed. Since this was not the case after heating in the RTA (under Ar/H_2 atmosphere), it appears that the role of vacuum is important in that regard. It seems likely that under vacuum, the gas trapped in under the wrinkles is forced to diffuse towards the edtes of the flake. Moving hBN wheels on the surface also helped.

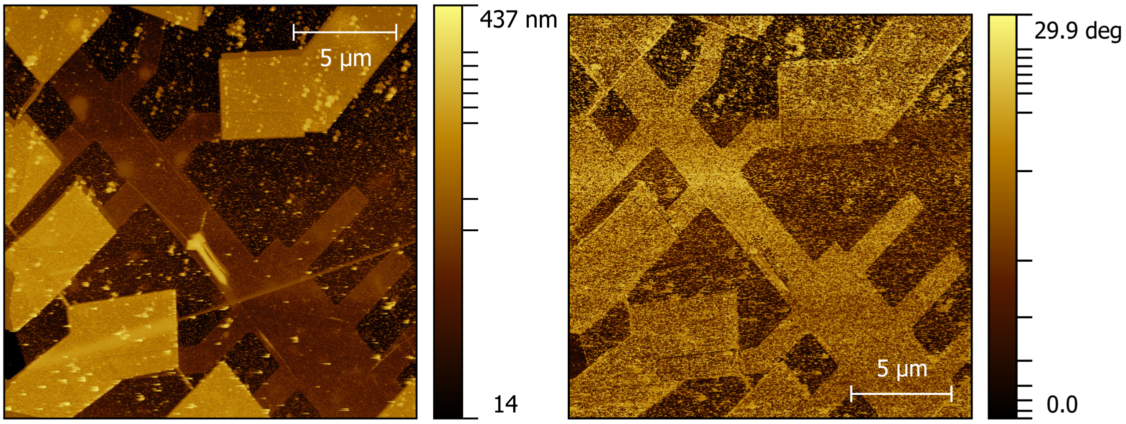

(a) (b)

Figure 3.23: (a) Topographic and (b) phase AFM image of Sample 3, after contacting and etching the BLG Hall bar.

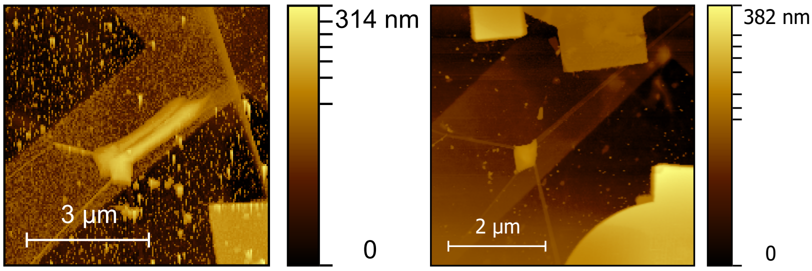

(a) (b)

Figure 3.24: AFM images of biggest wrinkles (a) before and (b) after cleaning under vacuum at 360°C

3.5 h-BN Wheels

Now that the main structure is fabricated, in order to obtain a tunable Moiré superlattice, a rotatable hBN structure must be added.

3.5.1 FIB milling attempts

A first method tested for the fabrication of the hBN wheel was to mill in exfoliated hBN flakes with a Focused Ion Beam.

A Focused Ion Beam (FIB) setup is an instrument that uses a focused beam of gallium ions to bombard a sample, very similarly to a scanning electron microscope (SEM) that uses a focused beam of electrons. But the FIB allows not only to image a sample but also to mill the material at well localized sites.

The apparatus is coupled with a SEM (for non-destructive imaging of the sample during process) and has become a very powerful tool both for characterization and nanomachining of of various 2D or 3D patterns, with very high resolution and precision.

Using this method for hBN wheels poses a risk of implantation of Ga ions at the spots scanned by the FIB, which can affect the experimental measurements.

Attempts were made to create simple squares in hBN flakes, adjusting the exposure time and area and the beam current at each test.

After a few tests, squares of hBN were defined by milling rectangles of 12µm x 1 µm exposed during 60s with a current of 50 pA (if the area targeted changes, either the exposure time or the beam current can be tuned to keep a constant exposure dose). The result is shown on Figure 3.25. The grooves carved in the flake (and the SiO_2) are $\sim$ 80 nm deep (which is larger than the thickness of the flake).

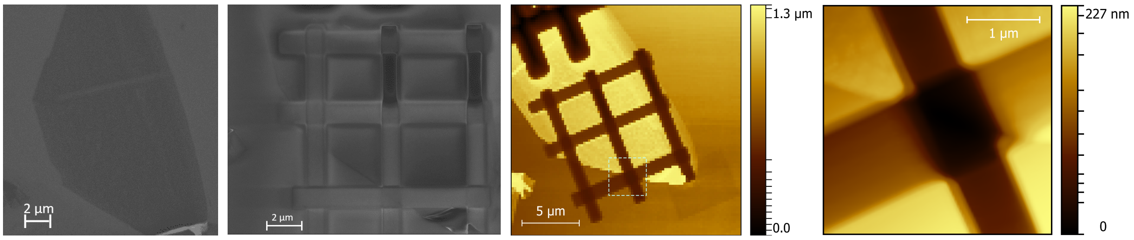

(a) (b) (c) (d)

Figure 3.25: hBN flake milled with the FIB. (a) SEM image before milling. (b) SEM image after milling. (c) AFM image after milling. (d) AFM image zoomed on a small area.

Surprisingly, it appeared that the milled hBN could not be picked and transfered after that, unfortunately. So these attempts ended up being unsuccessful for that purpose.

3.5.2 Electron beam lithography and RIE

The alternative is to etch the wheel after e-beam lithography on an exfoliated flake.

First hBN simple layer wheel

First a wheel made of a simple layer of hBN was transferred on the device. The lithography was realized the same way as described in section 3.4.1, and reactive ion etching was realized SF_6/Ar ionized gases in proportion 1:1, with a total flow of 20 sccm, an RF power of 100 W, and at a pressure of 10 mTorr during 20 s. As SF6 and Ar etching are dominated by physical sputtering effect rather than chemical reactivity, hBN is etched with very vertical angles (result of etching is shown on Figure 3.26-a).

hBN/HSQ wheels

But as seen later in section 4.1.2, the hBN sheet is too thin and fragile for the nanomanipulations intended. In order to have a three-dimentionnal block that can be moved

more easily, a supplementary thicker layer of material on top of the wheel would be useful. A good solution is to coat the sample with Hydrogen silsesquioxane (HSQ) instead of PMMA before lithography. Not only is HSQ a negative resist for EBL (which means that the electron beam will strengthen chemical bonds and the areas to conserve are exposed, i.e. the area of the wheel), but also has the peculiar property to transform into a different phase which approaches closely the structure of amorphous silicon oxide (SiO_x), when exposed to the electron beam.
Thus, after etching, the resist must not be stripped, and a 120 nm SiO_x (or HSQ/SiO_x) layer is obtained on top of hBN (see the result on Figure 3.26-b).

Note that, in order to obtain a better adhesion, the hBN flake was exposed to an oxygen plasma for 15 s before spin-coating HSQ, making the hBN surface more irregular and rough. In consequence the HSQ adheres well on the surface. Note also that e-beam lithography on HSQ requires higher dose ($\sim$ 3 times higher than on PMMA).

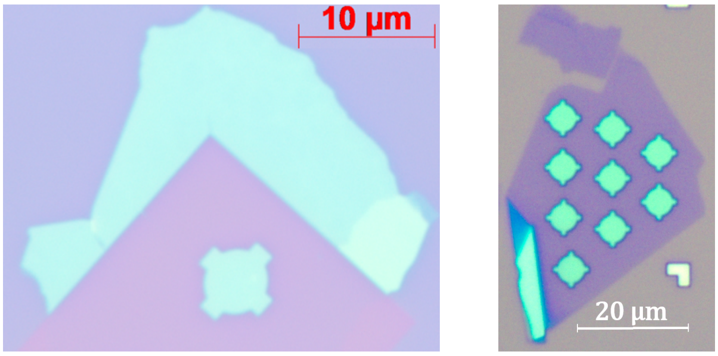

(a) (b)

Figure 3.26: Optical microscope image of etched hBN wheel, before transferring on Sample 3. (a) First simple hBN wheel. A very clean (and slightly etched) area of SiO_2 is visible on the area exposed to the plasma etching. (b) hBN/SiO_x wheels.

The wheels are then simply transferred on the Hall bar device in the same way as described in section 3.3. To be sure to have at least 1 or 2 ”useful” wheels correctly transferred on the bilayer graphene, an array with a large number of wheels was lithographied on the same flake. This is why many wheels are visible on the images.

The complete process of fabrication and transfer of an hBN/SiO_x wheel is summarized on Figure 3.27.

Images of the final resulting device are shown on Figure 3.28 and Figure 3.29. Note that the sample was first partly cleaned spending a short time in RTA under Ar/H_2 atmosphere when transfering the first hBN wheel (Figure 3.28-a), but was then cleaned under vacuum at 360°C for 2 h (before and after adding the hBN/SiO_x), which removed most remaining traces of PPC.

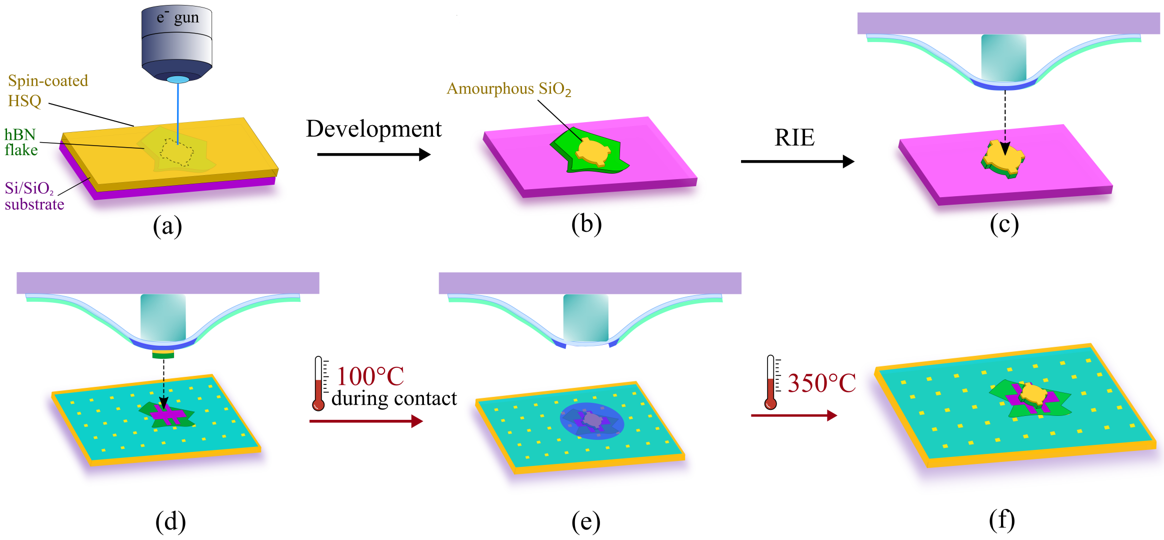

(a) (b) (c)

(d) (e) (f)

Figure 3.27: Step-by-step representation of the fabrication and transfer of hBN/SiO$_x$ wheels. (a) e-beam lithography. (b) Development and curing of HSQ, transforming into SiO$_x$. (c) RIE and Picking of the wheel in a PPC film. (d) Transfer on the Hall bar, put directly in contact with the BLG on the sample. (e) Heating of the wafer to 100°C and lifting of the transfer slide, leaving the PPC film on the wafer. (f) Cleaning under vacuum (or RTA under Ar/H$_2$ atmosphere) at 360°C.

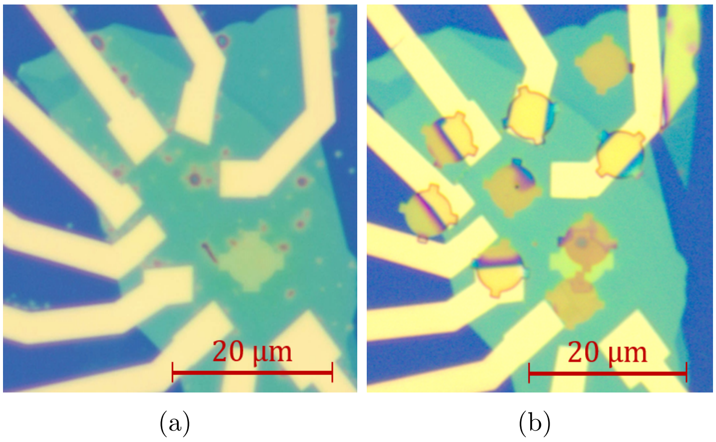

(a) (b)

Figure 3.28: Optical microscope image of the finished sample: (a) before and (b) after cleaning and adding the hBN/SiO$_x$ wheels.

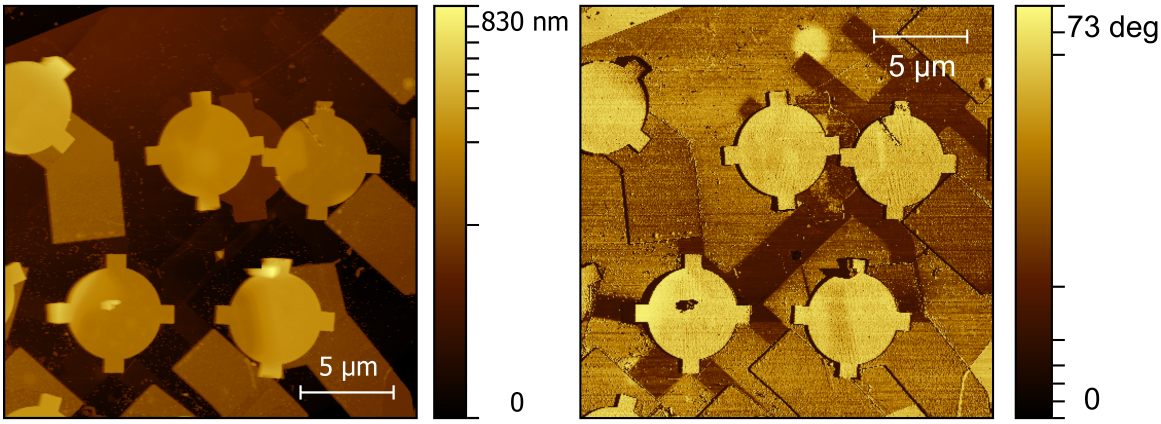

(a)

(b)

Figure 3.29: AFM image of the finished sample: (a) topography and (b) phase image.

Chapter 4

Experimental results and discussion

In this chapter, the experimental results of frictional, electrical, and Raman measurements are provided and discussed.

The nanomanipulation principle is first explained, then the setup and nanomanipulation procedure is described, and observations over the wheels sliding are provided. Tribology notions necessary to understand frictionnal mechanisms in graphitic structures at the nanoscale are explained and in the light of state-of-the-art researches, the friction measurements in the heterostructure are presented and analyzed. Electrical measurements (and device failure) and then Raman measurements are finally discussed.

4.1 AFM nanomanipulations and friction

4.1.1 Working principle

In addition to its remarkable imaging and measurement perfomances, the AFM is also a powerful Nanomanipulation tool that can be used to modify nanometric structures. Nanomanipulation consists in maneuvering the probe as a hand to perform computer-controlled manipulations. The AFM tip can be used to move, cut, push or indent samples with very high precision, taking advantage of the precise control and positioning of the probe (down to sub-nm scale). This technique is already widely used in different fields such as biology, genetics, photonics research and nanorobotics, and generally speaking, in bottom-up assembly of nanostructures.
Thus, using the same AFM equipment, the sample is imaged, modified in a controlled way, then re-imaged to see the result.

4.1.2 AFM nanomanipulations of the wheels

As explained in section 2.5, Ref. [42] showed that hBN wheels can be moved in a controlled fashion on a graphitic structure, using this technique. The nanomanipulation is made possible using the software Nanoman developed by Bruker.

Although the nanomanipulations are done in contact mode, the probe used is a tapping mode probe (OTESPA-R3 tips with a cantilever length of 160 µm and a stiffness of 26 N/m). Indeed, for contact mode imaging, a less rigid cantilever is required so that it can torque smoothly as the tip slides on the surface, and so that the deflection is very sensitive to any features on the surface (and also to avoid scratching delicate materials). For the nanomanipulations of interest however, a more rigid cantilever is needed to push the whole hBN wheel and overcome the friction between the layers.

The wheels are moved on the sample by implementing straight-lined segments: after imaging the sample in tapping mode, vectors can be drawn in the Nanoman interface that represent the movements imposed to the tip. The tip movements are executed in contact mode, with the feedback deactivated at a horizontal velocity of 0.1 µm/s. The vertical force is configured by the imposed deflection set point (the value depends on the tip used) which was generally set between -100 and -500 nm. After execution of the tip movement, one can check if the wheel moved by making a new tapping image.

Manipulations were first tried on the single hBN wheel that was first transferred on the sample. But all the attempts resulted in folding or damaging the handles. The HSQ (SiO_x) layer thus seemed to be mandatory to obtain a 3D shape that can be effectively pushed with this technique.

After transferring new hBN/HSQ wheels on the sample, these were moved a lot to obtain a more adequate configuration for further experiments: images of the sample before and after manipulations are shown on Figure 4.1.

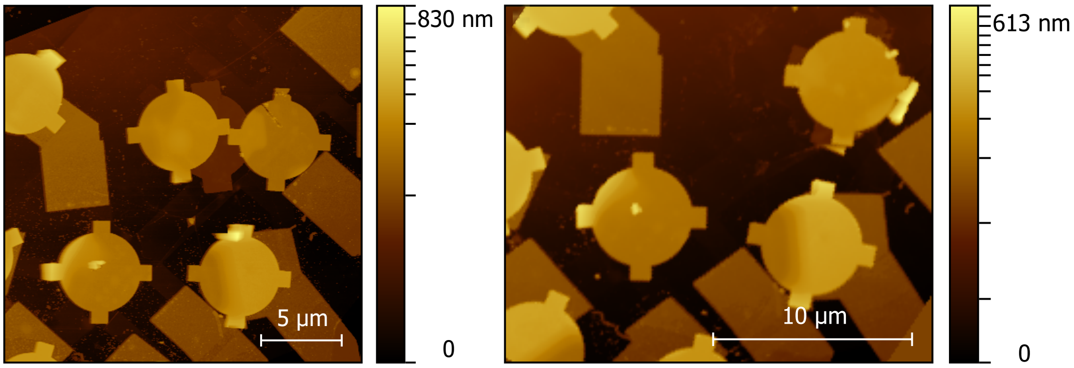

(a) (b)

Figure 4.1: AFM images of the whole sample (a) before and (b) after nanomanipulations of the wheels.

Step-by-step movements on Figure 4.2 illustrate the effect of the sequential movements

imposed with Nanoman to the tip to move away cumbersome wheels.
Generally the first movements of an hBN object is quite difficult, as if the adhesion was too strong. But after a few gentle slight rotation movements, it becomes possible to move it really easily and as much as wanted.
As will be discussed later, it could also be seen that while moving wheels away, the latter push polymer residues with them.

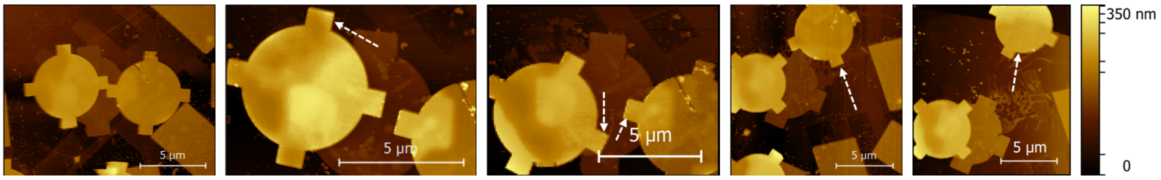

Figure 4.2: Step-by-step AFM images of the movements of some wheels to reach a more adequate configuration (the white dotted arrows indicate the movements that were just executed).

Figure 4.3 shows that it is possible to make sliding movements with an hBN layer on another hBN lattice, as long as these are misaligned. The new hBN/HSQ wheel was positionned completely on top of the first hBN wheel, and rotated until the lattices are aligned. At that point, the two hBN layers are blocked together and the AFM tip can not make the upper layer slide anymore.

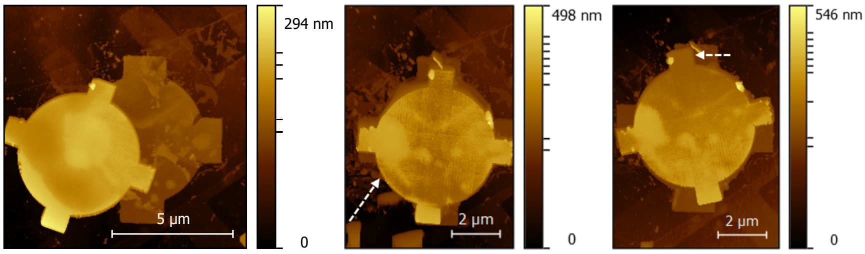

Figure 4.3: AFM images of the alignment procedure of the new hBN/HSQ wheel on the first hBN wheel, step by step.

Figure 4.4 shows that after that, when pushing the upper wheel, the lower hBN wheel always follows the same movement, and the two can now only move together.
This is a good illustration of the anisotropy and different frictional states that arise in homogeneous interfaces, as explained later in this section.

It could be noticed that when rotating or translating wheels, the latter tend to push the filth (polymer, impurities) on their way. e.g. in particular, when the "double" hBN wheel (topped by another aligned wheel) was finally moved, a very clean spot appeared at its original position (this is slightly visible on Figure 4.1-b and Figure 4.4-c). Using the wheel as a "broom" is thus a good way to clean the Hall bar at interesting spots before measurements[1].

---

[1] however, the sample wasn't cleaned this way because of timing issues

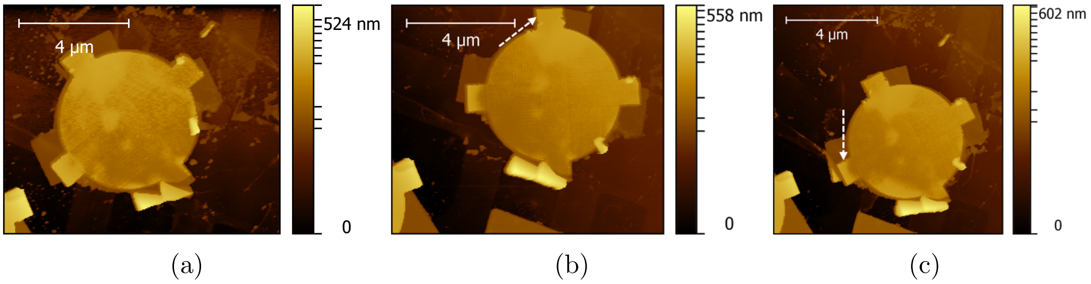

(a) (b) (c)

Figure 4.4: AFM images of the two aligned wheels moving together.

AFM nanomanipulations were also used to attempt to break short circuits appearing between the gold contacts as shown on Figure 4.5-a (probably due to the way the electron beam scanned each pad one after the other during lithography). This method was successful: results are visible on Figure 4.5-b and c.

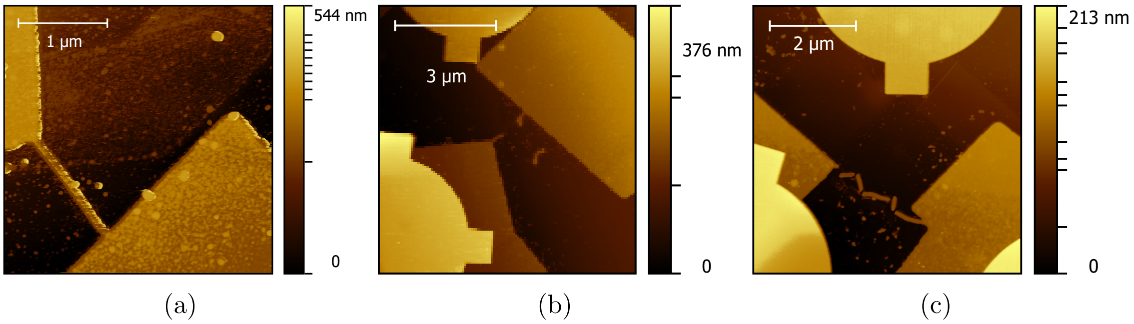

(a) (b) (c)

Figure 4.5: AFM images of some short circuits in the device before (a) and after (b and c) being cut by the AFM tip.

4.1.3 Tribology and superlubricity

Nanoscale friction mechanisms on graphitic surfaces has been investigated in several studies in the past.

Ref. [62–66] studied in particular friction of a graphite (or graphene) layer sliding against another graphite layer (homogeneous interface) and brought to light the appearence of a state where friction is very low (nearly ”vanishing”) called superlubricity when the lattices of graphene are misaligned. In contrast, when the lattices are aligned in bernal stacking, the layers are nearly locked, and when forced to friction, the layers exhibit highly dissipative stick-slip motion, with friction force several orders of magnitude higher than in misaligned interfaces.

This description corresponds well to what was observed when sliding an hBN wheel on another hBN surface, which seems logical as hBN posseses a similar hexagonal structure: when misaligned, the wheel was easy to move, and when aligned, the AFM couldn't overcome the vdW interactions keeping them together, and it became more favorable for the whole system to slide over the graphene.

To obtain superlubricity, the interface must be made of clean, chemically inert and atomically flat rigid surfaces. Wrinkles due to the transfer process and impurities have an important impact on the friction.

The ambition of these studies resides in the fact that structural superlubricity has the potential to provide a viable alternative to liquid lubricants in view of achieving effective reduction of friction and wear in small devices.

The explanation of the superlubricity and dissipative states resides simply in commensurability arising when two identical hexagonal lattices are aligned, and the incommensurability when they are not.
Figure 4.6 shows how the atoms motion is modeled in the Frenkel–Kontorova–Tomlinson model [67–69] (the 2D layers are simplified in a 1D chain of atoms, linked by strings, over a 1D periodical potential). In the commensurate case (Figure 4.6-a), as the periodicity of the atoms in the upper layer matches the periodicity of the potential generated by the atoms of the lower layer, the upper ”chain” will favor configurations where each atom is in a minimum of the potential. Sliding one layer over the other implies a change of configuration: this requires a lot of energy as all the atoms must be moved from their ideal position. The atoms, that do the same movement at the same time, are first pulled (and stick to their position) until the force becomes sufficient to make them jump to the next interstitial position (they slip), resulting in the stick-slip motion. Friction in commensurate interfaces thus requires a lot of force, corresponding to the single atom friction multiplied simply by the number of atoms.
The magnitude of friction is dependent on the number of atoms and thus on the size of the moving flake.
Figure 4.6-b shows the model in the case of an incommensurate interface. Instead of sticking and slipping together, like in the commensurate case, the atoms move over the barrier more or less one by one, inducing periodic compressions and stretches in the chain. As this time, the periodicities do not match, the ”chain” has no energetically preferred position. In each configuration of the chain, one atom is near a minimum for instance, and by sliding the chain of a small distance, a different atom will get close to a minimum. Altogether, the configuration is globally indentical. The ground state energy of the chain is thus ”translationally invariant” [70]. So not much energy is necessary to slide one layer on the other, and friction is dramatically reduced (the lateral shear forces cancel each other out). The friction is then independent on the area of contact, and the only remaining friction component is due to effects arising in rim areas [64].

Heterogeneous interfaces of graphene/hBN (or graphite/hBN) were also later studied experimentally and in simulations [71, 72]. In this case, because of the lattice mismatch, there is no true commensurability at any angles and the friction anisotropy is orders of magnitude smaller than in homogeneous junctions [71]. The superlubricity is even said to persist in aligned contact [71, 72]. This is why in the whole experiment, wheels

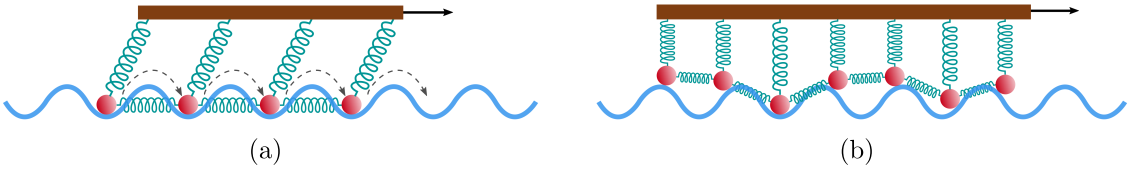

Figure 4.6: Frenkel–Kontorova–Tomlinson one-dimensional model of the nanoscale friction mechanism between two atomically flat surfaces.The upper surface is represented by an (infinitely long) chain of atoms (in red) connected by springs. If there is more than one atomic layer, the atoms can also be connected by springs to an upper rigid structure (in brown) that is moved in the direction of sliding. The lower surface is considered stiff and rigid and is represented by a sinusoidal potential (in blue), whith wich the red atoms interact. (a) In the commensurate case, the spacing between each atom of the upper chain is the same as (or an integer number of times) the periodicity of the potential. All the atoms can lie in a minimum of the potential, and must be removed from their position in a collective motion, requiring energy. The atoms exhibit together stick-slip motions with dissipation. (b) In the incommensurate case, the spacing between the red atoms is different from the periodicity of the potential. Each atom is randomly far from or close to a potential well. Thus, considering infinite chain and potential, each relative position is equivalent, and thanks to the various force magnitude acting in each of the atoms strings, the motion of the upper system is easily performed.

are easily moved on the graphene Hall bar, without any risk of blocking the lattices together. There is still frictional anisotropy though, as explained in subsection 4.1.4 (Figure 4.10), but the phenomenon is quite different from homogeneous interfaces.

4.1.4 Rotation and friction

To produce friction measurements during movements of the wheel, the same parameters are used (deflection setpoint, feedback deactivated, etc.), except that horizontal velocity of the tip is reduced (generally 0.05 µm/s, or less for more detailed measurement).
The principle of measurement was explained in section 2.5 (recording the horizontal deflection of the tip, which is representative of the friction magnitude).

An important constraint that is added in the manipulation is that the segments implemented must be in the vertical direction (y-direction), because all the frictional interactions between the tip and the surface must be translated into torsion of the cantilever (causing only horizontal deviation of the laser beam on the photodiode). The direction of the movement must thus be perpendicular to the orientation of the cantilever (which is always horizontal, along the x-direction).
It is then necessary to record the friction channel while the tip is executing the straight-lined implemented path.

The result obtained is a curve representing the voltage signal generated by the photo-

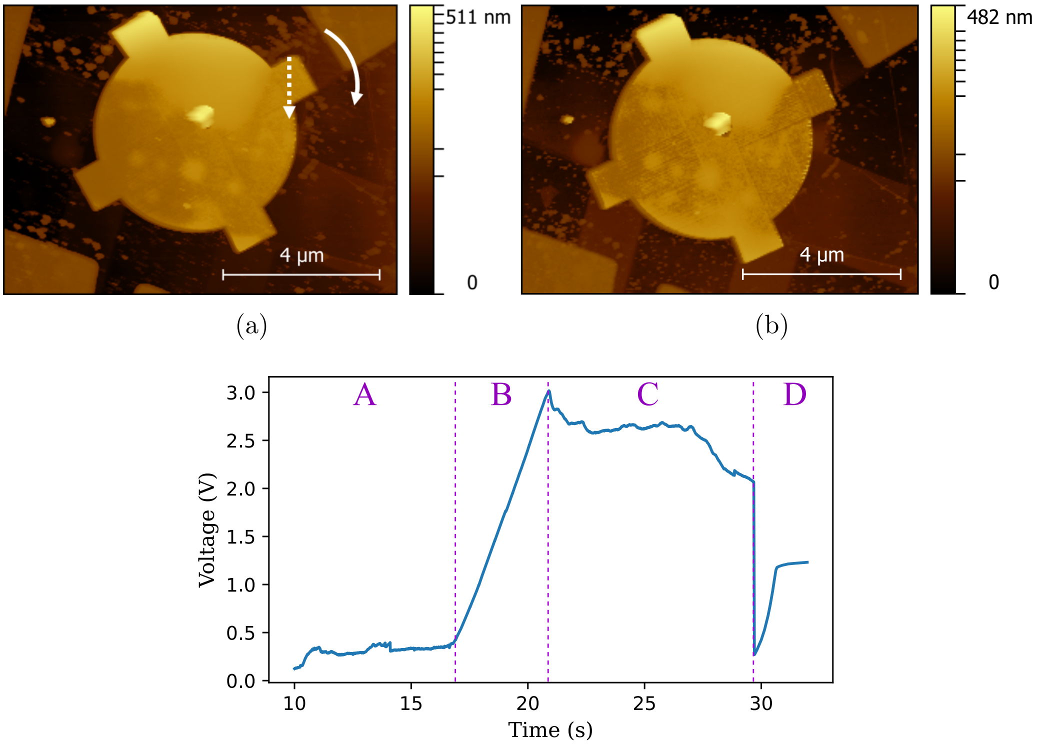

(a) (b)

(c)

Figure 4.7: (a) AFM image of the wheel before the downward movement of the tip (the dotted white arrow represents the straight-lined segment implemented in Nonoman, and the plain white arrow shows the sense of rotation of the wheel resulting). (b) AFM image of the wheel after the tip movement. (c) Recorded voltage generated on the photodiode during the tip movement as a function of time (the different steps of the friction are labeled A, B, C...). The friction is measured with a tip velocity of 0.05 µm/s.

diode as a function of time, as shown on Figure 4.7-c for the movement of the tip and the hBN wheel on BLG shown between Figure 4.7-a (the dotted arrow represents the segment implemented that is about to be executed, and the plain curved arrow shows the resulting rotation movement of the wheel) and Figure 4.7-b.

The curve is separated in different steps of the contact:

A: The tip slides against the BLG surface in dynamic friction.

B: The tip encounters the edge of the wheel and starts to cant away while pushing against it. The friction between the hBN and BLG layer is static, until the "maximal" force is reached, corresponding to the maximal deflection of the tip (peak of the curve).

C: The hBN layer starts to slide on the BLG layer in dynamical friction, pushed by the tip.

D: The tip has finished the implemented movement and can be lifted.

Figure 4.8 shows that for an upward movement of the tip, the voltage signal of the photodiode is inverted, because the cantilever is torqued in the opposite direction, and thus the beam is deviated on the other half of the four-quadrant photodiode.
Besides, the dynamical hBN/BLG friction part of the signal seems more constant and regular than in Figure 4.7. This might be due to the fact that impurities were pushed in one direction (clockwise rotation on Figure 4.7), then the wheel was rotated in the other direction (counter-clockwise rotation on Figure 4.8), so that there is a smaller amount of impurities left to push.

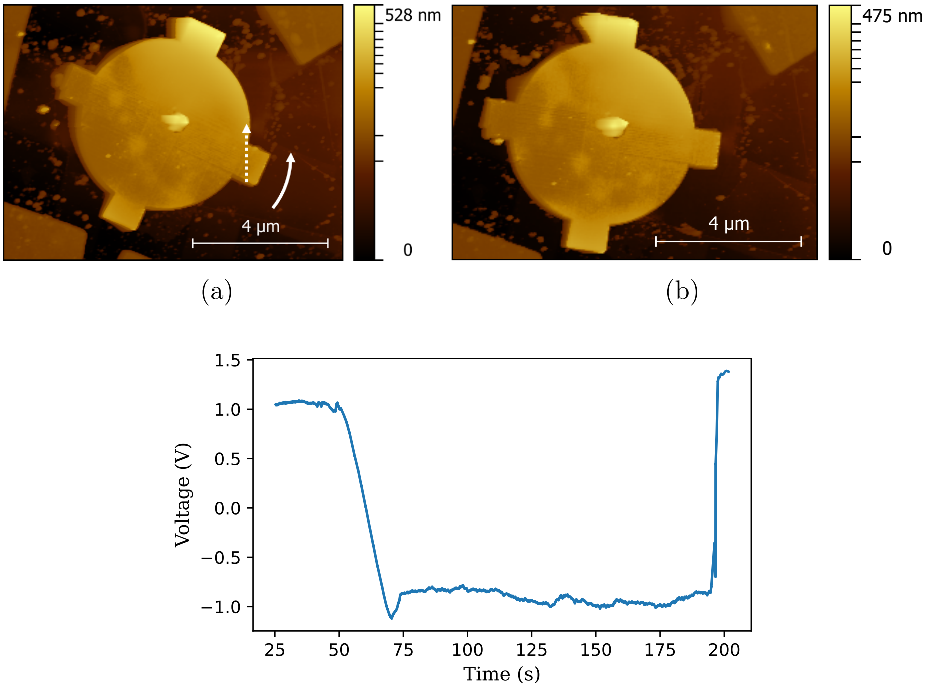

(a)

(b)

(c)

Figure 4.8: (a) AFM image of the wheel before the upward movement of the tip (the dotted white arrow represents the straight-lined segment implemented in Nonoman, and the plain white arrow shows the sense of rotation of the wheel resulting). (b) AFM image of the wheel after the tip movement. (c) Recorded voltage generated on the photodiode during the tip movement as a function of time. The friction is measured with a tip velocity of 0.05 µm/s.

Figure 4.9 shows the recorded friction curve when the two layers pass through the aligned position. A high peak appears then during the hBN/BLG dynamical friction step. As mentioned earlier, this maximum kinetic friction is a sign of frictional anistropy in the interface, which is coherent with experimental and simulation observations from the litterature introduced in section 4.1.2. The relative rotation angle can be identified to zero degree at the position of the peak, and the global span of the rotation imposed can be measured on the AFM images[2], with an error bar of ±1°. The zero-degree alignment is assumed to coincide with the position of the maximum/minimum of the signal (the error bar is difficult to assess in that case).

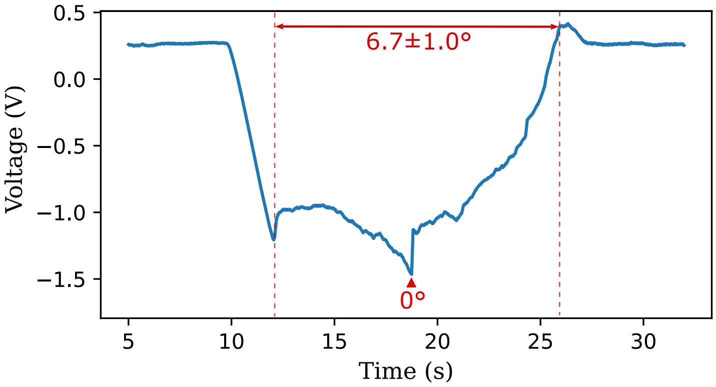

Figure 4.9: Recorded voltage generated on the photodiode during the upward tip movement as a function of time, in the case where the two hexagonal lattices pass through the aligned position (the red triangle indicates the peak marking the moment at which the layers are aligned). The friction was measured with a tip velocity of 0.05 µm/s.

Heterogeneous interface frictional anisotropy was studied experimentally and in simulations by Song *et al.* [71]. The experimental friction curve is shown on Figure 4.10, confirming not only that the anisotropy is at the origin of a maximum friction at aligned position, but also that it appears with six-fold symmetry, as already seen in Ref. [42].

In the same piece of work, using atomistic molecular dynamics simulations, Song *et al.* showed that the origin of frictional anisotropy in such homogeneous and heterogeneous interfaces should arise from completely different physical mechanisms: in the graphite/hBN interfaces, the friction energy dissipates through the internal degrees of freedom of the two layers in contact, while in homogeneous graphitic contacts, the friction energy dissipates through the center-of-mass motion (the stick-slip motion described in section 4.1.3) [71].
Indeed, in a previous simulation work, Mandelli *et al.* brought to light that in graphene/hBN aligned junctions, the motion is characterized by smooth soliton-like gliding of the superstructure ridges (for a contact size at least of the order of the moiré domain walls width), instead of the collective stick-slip motion (center-of-mass motion) observed in

---

[2] In this specific case however, the time data are not converted into an angle axis because the angular velocity can not be considered constant due to the irregularities on the right side of the peak.

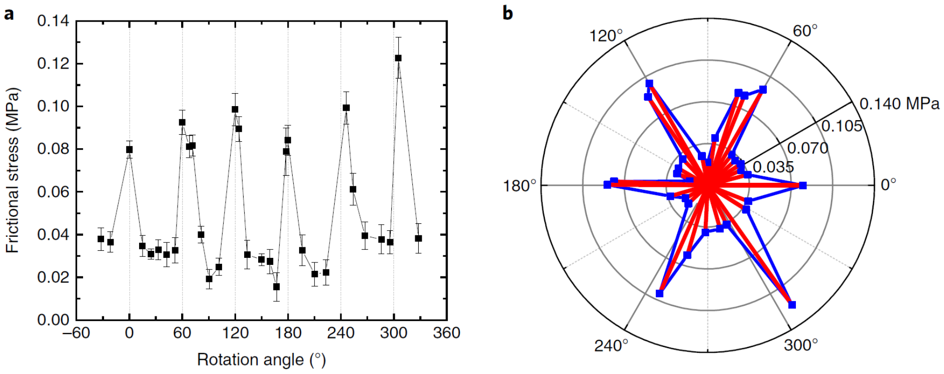

Figure 4.10: Frictional stress dependence on the rotation angle between the graphite and hBN surfaces under ambient conditions. Both linear (a) and polar (b) representations showed the anisotropy of the measured friction with six-fold symmetry [71].

graphene/graphene homojunctions [72]. More specifically, in the simulation model, the moiré superstructure is characterized by nearly-commensurate regions separated by domain walls (as discovered by Woods *et al.* in Ref [34]), inducing lattice stretches and compressions in the two lattices that tend to adapt to each other. And the system compensates the resulting tension with the formation of elevated ridges (out-of-plane deformation) [72].
So the movement of the atoms resembles the motion illustrated on Figure 4.6-b in the Frenkel-Kontorova-Tomlinson model (the heterojunction still exhibits the superlubricity state), but instead of the random distribution of the position of atoms with respect to the potential, there is a periodicity due to the moiré and the nearly-commensurate areas in the aligned case. The ridges are thus propagated by smooth soliton-like sliding, and only a fraction of the atoms cross a potential energy barrier simultaneously.
Song *et al.* [71] concluded from their simulations that at any angle, the internal degrees of freedom are the dominant factor of the frictional behavior in heterogenous interfaces (hBN/graphene), and the main energy dissipation is due to the out-of-plane motion of atoms. Those out-of-plane distortions are naturally larger when elevated ridges emerge, i.e., at small angles[3].
But the question remains of whether the commensurate/incommensurate transition (and thus the strains and out-of-plane distortions) can hold when the number of layers of graphene increase (in aligned commensurate stacking), as well as in the case of hBN encapsulation. If it was not the case, the explanations from Song *et al.* would fail to explain the anisotropy that clearly arises in these experiments.

Figure 4.11 shows again the peak due to alignment, but this time measured with slower tip movement (0.01 µm/s i.e. 5 times slower than for data in Figure 4.9) during the dynamic hBN/BLG friction (the movement is executed in the opposite direction), providing a more accurate curve shape, and a smoother evolution, especially around the peak (on Figure 4.9, the alignment peak looks asymmetrical, as if the movement was

---

[3] Woods *et al.* [34] established that the commensurate areas (which should be at the origin of the elevated ridges) appear only for angles $\lesssim 1°$.

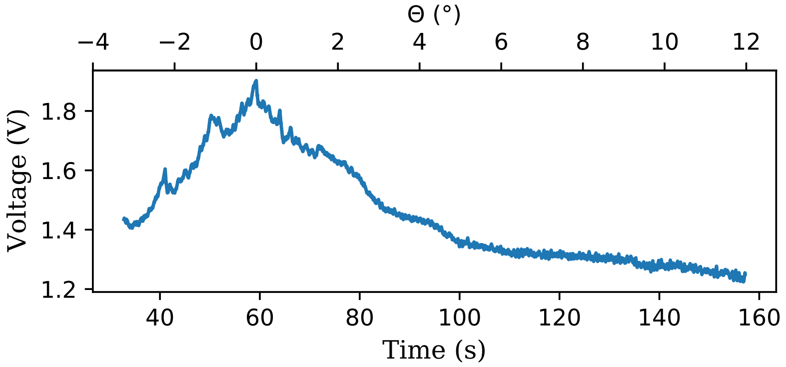

Figure 4.11: Recorded voltage generated on the photodiode during the downward tip movement (only during dynamic friction of the layers) as a function of time (or equivalently, as a function of the relative angle of rotation measured on the AFM images), in the case where the two lattices pass through the aligned position (0°). The friction was measured with a tip velocity of 0.01 µm/s.

locked then abruptly and instantly unlocked).

The relative rotation angle can now be identified during the friction, by establishing the peak position as the zero-degree alignment (indicated on the top x axis), and by assessing the rotation angle on the AFM images before and after friction. This angle measurement implies assumptions and simplifications: to convert the time data into angle, the angular velocity of the wheel must be assumed to be constant. In reality, the angular speed may have small variations, especially when the curve presents irregularities and small ("stick-slip-like") peaks. The impact of those non-linearities is neglected in this case. It is also assumed that the zero-degree alignment corresponds precisely to the position of the maximum/minimum of the signal.

The peak can be compared with one obtained with monolayer graphene (MLG) from Ref [42] on Figure 4.12. A few important considerations can be retrieved from the curve. The first observation is that the shape of the BLG/hBN curve looks slightly different from the MLG/hBN one: interestingly the peak seems a little larger ($\geq 6°$ wide) and deviates from the bell shape to display a rather linear trend. One should however remain cautious and avoid concluding too fast on those observations, due to the error bar in the angle measurement[4] and due to the fact that the presence of impurities or defects might impact the shape of the curve.

That being said, despite the error bar, the width of the curve looks quite larger than expected and raises questions. It appears that the friction starts to increase at a misalignment angle clearly larger than 1° from the alignment position. If the width of the anisotropy peak could be confirmed, knowing that Woods *et al.* [34] established that the commensurate areas (and thus the distortions and elevated ridges) should appear only for angles $\lesssim 1°$, this would raise the following questions:

---

[4] the total rotation is estimated of 15.5° with an error bar of ± 1.0°, meaning that data at smaller angles, closer to the alignment for instance, the measurement should be more more accurate

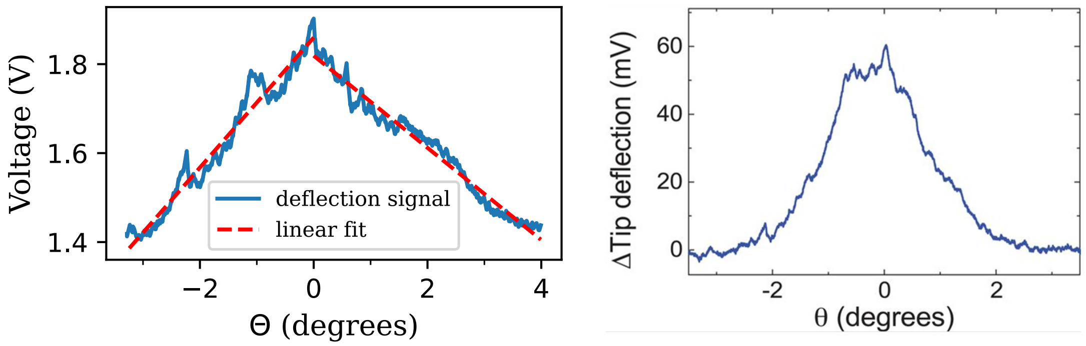

(a) (b)

Figure 4.12: Peak comparison: hBN/bilayer graphene friction curve (a) from this work (same measurement as Figure 4.11) and hBN/monolayer graphene friction peak (b) from Ref. [42]. In (b), the deflection is measured with respect to the constant level of deflection in misalignment configuration; and the zero-degree position is confirmed with simultaneous electronic transport. Both friction curves were measured with a tip velocity of 0.01 µm.

- Do strain solitons and elevated ridges reported by Mandelli *et al.* occur at angles larger than 1°, in the case of BLG/hBN ?
- Somehow, is the soliton-like motion of the hBN layer not linked to the commensurate-incommensurate transition investigated by Woods *et al.* ?
- Is the explanation of Song *et al.* erroneous or incomplete to understand the anisotropy ?

It is also important to point out that the friction might not be homogeneous in this experiment because the hBN/graphene overlap area is not always constant during friction (although for small angles, the variation should be very small). Moreover, there is also a friction contribution related to the hBN substrate, as some portions of area of the wheel (mostly the handles) sometimes stick out of the Hall bar and rubs against the hBN substrate (with a contact area that is thus also varying). However, this hBN surface was etched by the oxygen plasma (when shaping the Hall bar), which should prevent the high friction anisotropy (at hBN/hBN alignment), and make the surface more rough (so friction is much higher for these small areas). It is though difficult to know if the contribution is large or small, maybe even negligible: the surface areas at stake are very small, but the superlubricity (friction forces close to zero) is no more homogeneous over the whole hBN wheel.

Taking all these elements into account, the measurements may not be sufficient to conclude with absolute certainty in a different behavior in hBN/BLG friction than in hBN/MLG friction.

The quality of the curve could still be improved by pushing the wheel back and forth over the Hall bar many times before measurements, hence cleaning more the surface

(this could not be done due to timing and circumstances).
A larger rotation amplitude as shown on Figure 2.15-c from Ref. [42] would allow more accurate observations of the alignment peak.

A second interesting observation is the difference of peak height obtained in Ref. [71] (Song *et al.*) shown on Figure 4.10 with respect to misalignment friction level. Indeed, the ratio between the voltage at misalignment and alignment configurations should be roughly proportional to the change in the friction force between the two states. On the friction curves measured in our experiment, the ratio $V_{\text{alignment}}/V_{\text{misalignment}} \simeq 1.4$ (and it is also the case of the measurements done by Ribeiro-Palau *et al.*) while in Ref. [71] this ratio is clearly greater than 2.0 (as if the anisotropy was stronger).
Different explanations are possible:

- It is likely that in our case, the fact that the overlapping area is changing and the additional friction of the etched hBN substrate bring an important background contribution to the signal amplitude.
- Some previous studies suggested the existence of friction due to edge effects [73] or rim forces [64], especially in misaligned position. Depending on the contribution of those, the different edge and bulk proportions of each sample could have an impact. The question remains whether this friction contribution is more or less important than the contribution of the moire.
- Some fabrication parameters might have an impact, in particular an effect of the number of layers of graphene would be the most interesting (or even the thickness of hBN in the wheel). Or even the fact that a mobile hBN flake slides on a motionless graphene (or BLG) sheet, instead of using a mobile graphite flake, sliding over a motionless hBN substrate in the case of Ref. [71][5].
- The difference could be due to differences in the measurement technique. The methods are rather similar (both implying AFM tip deflection), but in Ref. [71], the technique implies a normal load applied by the tip on the sliding graphite flake.

Either one of these reasons or a combination of those could be at the origin of the different voltage ratio measured.

Finally, a third important observation is the appearance of small ”secondary” peaks on the left side of the main peak, at $\theta \simeq -2.2°$ and $\theta \simeq -1.1°$. As illustrated on Figure 4.13, the same peaks and global shape of the curves also appear on another friction measurement (curve below) done with the same wheel, on the same sample[6].

---

[5] Especially, if an important contribution comes from the edges, as the edges in graphene and hBN are not equaly inert, the friction of a graphite on top of hBN could be larger than the opposite configuration. One could also imagine that in one configuration, the friction related to the edges would dominate for longer than in the other.

[6] Note that the curves are measured with the same tip velocity and although the tip was moved in

Measuring the time interval t_r with respect to the maximum position (identified as the probable zero-degree alignement postion), the relative position of the peaks appears to be very similar in both measurements. It also appears that the signal is not symmetrical and this asymmetry as well as the global shape (a sort of shoulder seems to emerge at $t_r \sim 11$ s) is also reproduced in the second measurement. The reproducibility of the signal shows that the peaks (and some other features) are not due to noise.

Figure 4.13 provides a better view of the peaks themselves, by subtracting the linear fitting curve of the signal (shown on Figure 4.12).

It would be very interesting to check whether the different observations mentioned in this section could be confirmed by re-measuring the friction on another similar sample. If the peaks are reproducible, a natural explanation would be that they arise from an intrinsic behavior of the system, and that, for example, there exist stable configurations ("stability islands") at certain small twist angles.

It is however utterly possible that the peaks (and other features) are due to a defect in the sample, for instance one or several wrinkle(s). If it is the case, it could also explain the different width and shape observed on Figure 4.12.

To check the possibility of an intrinsic behavior, simulations of the sliding experiment (including lattice relaxation/reconstruction) should help to identify the reason for the local extrema.

---

the opposite direction both curves correspond to a counterclockwise rotation (a different handle of the wheel is manipulated). Unfortunately, there is no clean measurement of the analogous measurement during clockwise rotation

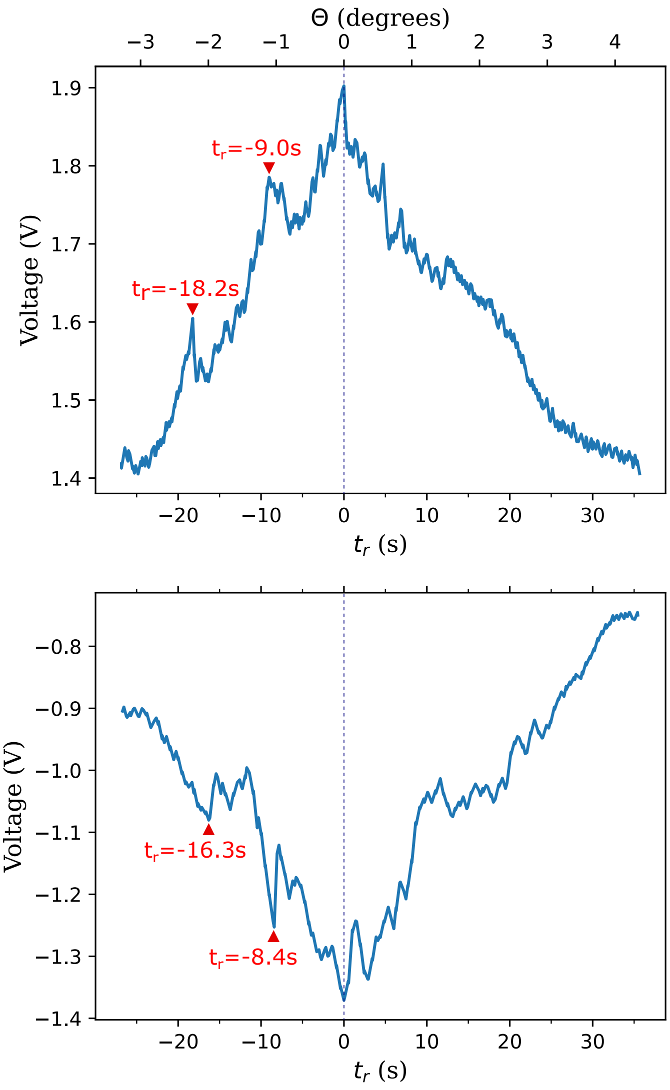

Figure 4.13: The first curve (above) is the same curve as on Figure 4.11 and Figure 4.12-a. The second curve is another friction measurement realized with the same wheel (on the same sample). The two curves were measured with the same tip velocity of 0.01 µm/s, and both correspond to a counterclockwise rotation (one corresponding to a downward movement of the tip, on one handle of the wheel, and the other to an upward movement, on the opposite handle). Secondary peaks appearing on both signals, roughly at the same time interval, relatively to the main maximum peak position, are highlighted with red triangles.

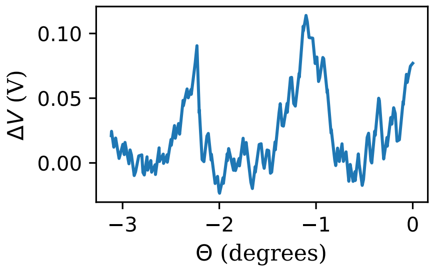

Figure 4.14: Friction signal from Figure 4.11, from which the linear fit is substracted to highlight the existence and shape of the secondary friction peaks.

4.2 Electrical measurements

Electrical measurements were a central motivation in this study.

A first measurement of the four-terminal resistance of the BLG Hall bar was taken at room temperature after transferring the first hBN wheel[7]. The 4-point resistance was recorded while sweeping the back-gate voltage (V_G). For bilayer graphene, a roughly similar curve shape as seen in the litterature for monolayer (Figure 2.16) is expected.

When collecting the measurements at contacts between which no hBN was deposited, no dirac point maximum appeared. As the BLG is exposed to air and not protected by encapsulation, unwanted doping effects are at play.

But when measuring at contacts between which lies the hBN wheel, the curve on Figure 4.15, a maximum resistance is visible near 0 V (corresponding to the CNP), as expected. In this case, the BLG is encapsulated and protected by hBN, assuring a better quality of the measurements.

As the hBN is misaligned on the BLG, naturally the secondary Dirac points are not measurable for a reasonable range of V_G.

The curves appear quite asymmetrical: on the electrons-side, the resistance does not decrease as much as on the hole-side. This could be due to inhomogeneities, for instance areas where the Dirac point might arise at higher gate voltage (even higher than 20 V), or inhomogeneous doping around the contacts area.

It can also be observed that the Dirac point is slightly shifted during the second V_G sweep (from high voltage to low voltage) with respect to the first V_G sweep (from low voltage to high voltage), which is probably due to charge accumulation in the SiO_2 dielectric cystal.

Then the central point of interest of the experimental results would have been to provide such electrical measurements while varying the orientation of hBN wheels by nanoma-

---

[7] the measurements were realized with equipment using needles, as the sample was not bonded yet

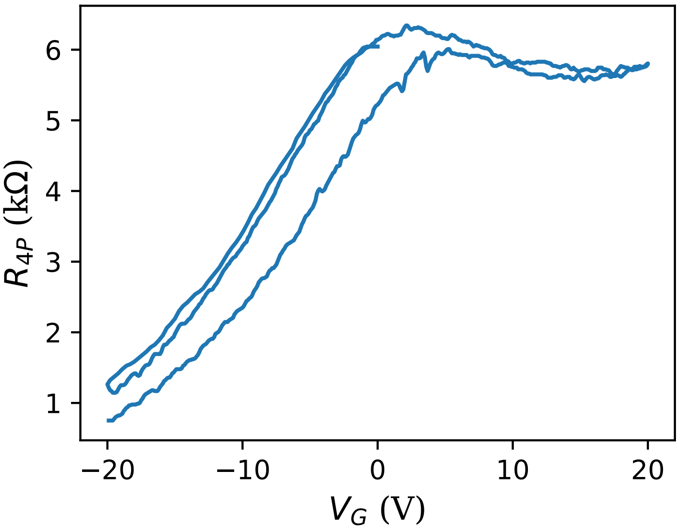

Figure 4.15: 4-terminal measurement of the sample resistance (R_4P) as a function of the back-gate voltage V_G during consecutive sweeps of the latter at room temperature.

nipulation (and then measurements at very low temperature).

But unfortunately, when later, after further completion of the device (adding and alignment of hBN/SiO$_x$ wheels, bonding ...), measurements were attempted again, all the contacts seemed to have deteriorated a lot (moreover the Hall bar was accidentally ripped and folded in its middle during one of the attempts of motion of the wheels). All kind of 2-points or 4-points measurements between any of the contacts would yield unreasonable resistance values (and large out-of-phase signal on the lock-in measuring the resistance).
It would seem that one or several processes undergone by the sample (heating, RTA, cleaning in solvents such as acetone and isopropanol ...) or the ripping of a part of the Hall bar may have degraded the quality of connection between the Ti/Au contact and the BLG layer.

Thus the experiments could not yet fulfill the desired goal to get to the bottom of the angle dependence of electrical transport in a BLG/hBN tunable moiré superlattice (that could be compared to the case of monolayer investigated in Ref. [42]), nor to reproduce experimental achievement of superconductivity, as described in [2].

4.3 Raman measurement of the twist angle

In a previous study, Cheng *et al.* [53] brought to light a method for measuring the twist angle between bilayer graphene and hBN, using the Raman signature of the stack. They observed a linear dependence of the widths of the 2D subpeaks with the superlattice period (yielding the relationship with the misalignment angle).

The objective would have been here to assess the change of FWHM of the subpeaks obtained after rotating the wheels.

Unfortunately, measurements taken after completion of the device provided signals with a large background and a lot of noise. Figure 4.16-a shows the Raman spectrum measured after transferring the first hBN wheel (the sample was only "partly" cleaned and a lot of PPC residues were remaining as shown on Figure 3.28-a). The G- and 2D-peak are still quite recognizable (and the peak at 1360 cm^{-1} is a feature of the hBN raman spectrum).
Two months later, after adding the other hBN/SiO$_x$ wheels, and after the sample underwent better cleaning procedures (oven under vacuum), the Raman spectrum was measured again. And despite the cleaning, the signal (that can be seen on Figure 4.17) seems to get even worst. But the shape of the 2D-peak is still relatively discernible.

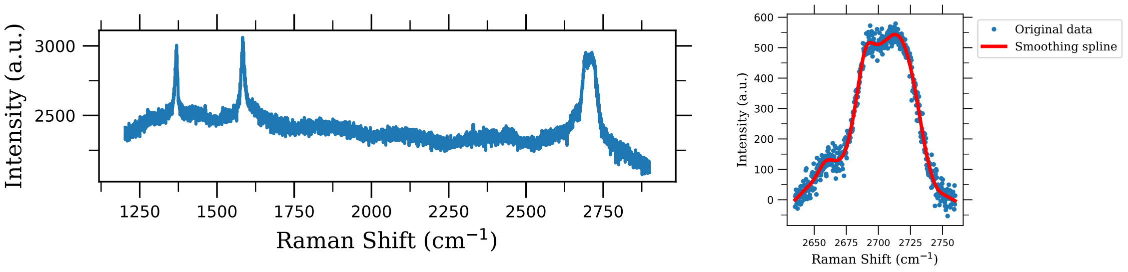

(a) (b)

Figure 4.16: (a) Raman spectrum after completion of the device with one pure hBN wheel. The laser spot was targeted on the wheel (the layers measured are thus encapsulated BLG with random angles). A green laser (514 nm) is used. (b) Zoom on the 2D peak. The background is locally removed, and a smoothing spline is constructed on the base of the noisy data, allowing to better distinguishe the features generated by the subpeaks.

Removing locally the background and using a smoothing spline, the signal of the 2D peaks could be improved, as shown on Figure 4.16-b and Figure 4.17-b. And those could again be deconvoluted into four lorentzian subpeaks (visible in Appendix A on Figure B.3), but those subpeaks seem too sensitive to the smoothing parameters used (the shape of the 2D peak, and hence the characteristics of the subpeaks can vary with number of knots for instance). Thus, due to the significant noise in these signals, parameters such as the precise FWHM of the subpeaks could not be retrieved with high accuracy.

It can however be observed that the 2D peak is shifted of ~ 8 cm^{-1} after encapsulation between the two hBN (substrate and wheel), with comparison of the spectrum measured on the exfoliated BLG flake on a Si/SiO$_2$ substrate.

Later again, the sample was measured with the blue laser in order to check if a different

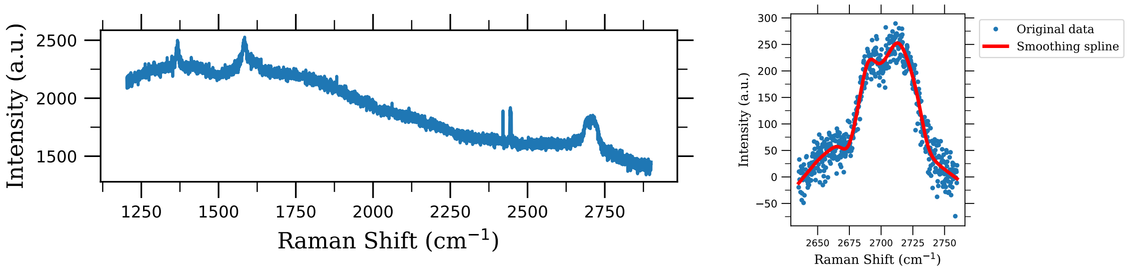

(a)

(b)

Figure 4.17: (a) Raman spectrum after cleaning and hBN/SiO$_x$ wheels. Again, a green laser source (514 nm) is used, the laser spot was targeted on the wheel. (b) Zoom on the 2D peak. The background is locally removed, and a smoothing spline is constructed on the base of the noisy data, allowing to better distinguishe the features generated by the subpeaks.

type of excitation might yield a different result (Figure 4.18). It can be noted that changing the excitation energy from a green laser to a blue laser shouldn't change the apparition of the characteristic peaks, but all the peaks except the G-peak appear with a slightly different Raman shift and intensity. Indeed, for processes that involve double resonance (including electron-phonon resonance), a different light wavelength will excite an electron to a slightly different level of energy and the position of this electron in the brillouin zone will be different depending on the excitation wavelength. This will strongly affect the selection rules for possible phonon emission, which is what Raman spectroscopy is meant to probe. The scattered photons energy will hence be slightly different.

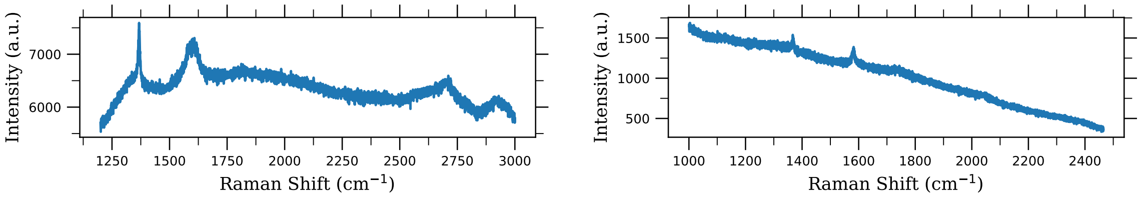

(a)

(b)

Figure 4.18: Raman spectrum of the same sample measured with (a) a green laser (514 nm) and (b) a blue laser (633 nm)

With the blue laser, the equipment doesn't allow measurements of Raman Shifts higher than 2500 cm^{-1}, leaving no possibility to see the 2D-peak. Besides, the background is still too significant. On Figure 4.18-a, this time the high background doesn't even allow to distinguish well the shape of the 2D-peak.

In the end, the effect of the twist angle on Raman peaks could not be studied in this work. It would have been interesting to compare the FWHM of the 2D subpeaks before and after rotating the wheels, but the too important noise (especially after the rotations) prevented to make such observations.

The reason of the apparition of the background is probably not linked to degradation of the BLG in particular, but rather to some kind of deterioration of the whole sample, because a background was also measured on the hBN bottom layer alone (as well as the hBN of unfinished samples) and on the substrate.
A background can also arise in the signal due to reflections from the metallic contacts. However, in other studies (such as Ref. [42]), Raman measurements could be made without encountering that kind of problem.
In conclusion, the origin of this problem remains puzzling. And again, the most probable justification would be linked to some of the processes undergone by the sample such as heating, RTA, or the use of polymers, solvents (acetone, isopropanol, anysole, ...) or the gain of impurities (although the background increased after cleaning).

Chapter 5

Conclusion and perspectives

In this master thesis, the effects of the twist angle between hBN and a bilayer graphene sheet were experimentally investigated.

As stated at the beginning of this work, several objectives were followed in this master thesis.
To begin with, the fabrication of the new device architecture developed by Ribeiro-Palau *et al.* was successfully completed for the first time at UCLouvain (WINFAB laboratories), with bilayer graphene instead of monolayer graphene. The device was functional as the rotation of the wheels by nanomanipulation was made possible, and electrical measurements could be done at the beginning of experimental trials.
The next objective was to achieve the alignment of the two crystalline orientations, which was done with help of friction measurements. The twist angle could then be measured and controlled thanks to this technique. Those measurements also allowed characterization of the friction between the two different lattices.
Technical device failures however prevented to go to the bottom of the angle dependence of the electronic transport in this tunable moiré superlattice, and also to characterize the twist angle effect with Raman measurements. Consequently, the exciting perspectives raised by potential electrical measurements simply remain to be done in future experimental work on a new sample.

Thus, the point of interest of the experimental outcome in this work was slightly reoriented from the electronic perspectives towards tribology and frictional aspects.
The observations made in this work raise questions about the existence commensurate/incommensurate transitions in the case of multilayer graphene (which are moreover sandwiched between hBN layers); its potential impact on the frictional anisotropy phenomenon; and the existence of strain solitons at twist angles beyond the 1° limit.
The friction data yield some new hints to answer these questions, and show a behaviour in BLG/hBN different from BLG/hBN. The data are however too scarce to answer these questions with confidence, and a more complete frictional study could bring interesting prospects. For instance, more diverse and numerous friction curves, with larger angles could be measured on cleaner samples for a clearer comparison. Measurements can be

done with samples of monolayer, bilayer, or more layers of graphene, with the same hBN thickness, and with a constant (or controlled) contact area. It could also be interesting to investigate how the behavior samples with hBN on top of graphene or with graphene on top of hBN differ, especially the edge effects in hBN and in graphene can bring a different contribution that can be studied with different wheel size and shapes.
Observation of secondary peaks in hBN/BLG friction could also either be the signature of stable configurations in the system, which would be a very interesting phenomenon and could raise very exciting prospects for more theoretical studies, or could just be due to a defect in the stack (such as a wrinkle). This calls thus for verification (again with new clean samples).

A few perspectives of improvements could also be retrieved from the sample fabrication. Defects in the flakes and stacks could be reduced and maybe the device failures could be avoided (although their origin is not well known). For instance, there are possibilities for improving the transfer technique in order to obtain less wrinkles in the heterostructure and simply to make it more efficient and less time consuming. Using an oven under vacuum instead of RTA to clean the samples might also be for the best. For now, using FIB milling appeared not to be a good alternative to the traditional lithography technique. In future work, samples can be fabricated with a graphite backgate under the hBN substrate, in order to obtain higher mobilities and to be able to make measurements in a magnetic field, allowing for instance to study further the moiré effect in quantum Hall measurements.

In a more global point of view, a wide range of perspectives are made possible by the device architecture presented. Plenty of possible combinations could be explored with a variable twist angle. Other exciting prospects also concern electronic friction: the way friction is affected by change in electronic density could possibly be evidenced (applying a backgate voltage during the friction measurement). The idea was put forward by Rebeca Ribeiro-Palau, and could open doors towards a whole new field, offering again a wide range of possibilities.

Acknowledgments

I would like to acknowledge the help of several persons who offered me a great deal of support and assistance, especially in the difficult context faced during this year due to the covid crisis, in which this study was conducted.

First of all, I wish to express my deepest gratitude to my supervisor Pr. Benoît Hackens for introducing me to this fascinating research field, and for all I learned from his precious advices. His relentless dedication and availability cannot be underestimated, always providing with guidance, suggestions for improvements, or even coming to help in the labs in critical times.

My special thanks to Nicolas Moreau for his patience and availability as he taught me most of the fabrications and characterization techniques, and monitored my work for many months. His kindness and encouragements, as well as the discussions about experimental techniques were very helpful to carry through this project.

I'm also extremely grateful to Rebeca Ribeiro-Palau who kindly welcomed me in her labs at the C2N, allowing me to perform electrical and frictional measurements. I can not express how much I learned from her invaluable experience and knowledge of the domain. I also enjoyed very instructive and inspiring discussions. I also take this opportunity to thank Everton Arrighi, who was very dedicated to help me draw as much results as possible from the short duration of my stay at the C2N.

I would like to thank Sebastien Faniel who spent a large amount of his time helping in the clean room me to realize complex fabrication processes and to manipulate sophisticated machines.

I would also like to warmly thank Hui Shang and Wasil Malik for generously offering me their help in the labs, and for interesting discussions.
I thank as well the WINFAB staff and users for their kind help with the equipment, and friendly converstations.

Finally I want to deeply thank my family and friends, who supported me through thick and thin, and provided me with all the comfort, the fun and the encouragements I needed during this work, and more.

Bibliography

[1] Yuan Cao, Valla Fatemi, Shiang Fang, Kenji Watanabe, Takashi Taniguchi, Efthimios Kaxiras, and Pablo Jarillo-Herrero. Unconventional superconductivity in magic-angle graphene superlattices. *Nature*, 556(7699):43–50, March 2018.

[2] Satoshi Moriyama, Yoshifumi Morita, Katsuyoshi Komatsu, Kosuke Endo, Takuya Iwasaki, Shu Nakaharai, Yutaka Noguchi, Yutaka Wakayama, Eiichiro Watanabe, Daiju Tsuya, Kenji Watanabe, and Takashi Taniguchi. Observation of superconductivity in bilayer graphene/hexagonal boron nitride superlattices, 2019. unpublished (arXiv e-print: 1901.09356).

[3] Guorui Chen, Aaron L. Sharpe, Patrick Gallagher, Ilan T. Rosen, Eli J. Fox, Lili Jiang, Bosai Lyu, Hongyuan Li, Kenji Watanabe, Takashi Taniguchi, Jeil Jung, Zhiwen Shi, David Goldhaber-Gordon, Yuanbo Zhang, and Feng Wang. Signatures of tunable superconductivity in a trilayer graphene moiré superlattice. *Nature*, 572(7768):215–219, July 2019.

[4] K. Novoselov, A. Geim, S. Morozov, D. Jiang, Y. Zhang, S. Dubonos, I. Grigorieva, and A. Firsov. Electric field effect in atomically thin carbon films. *Science*, 306(5696):666–669, October 2004.

[5] Recep Zan, Chris Muryn, Ursel Bangert, Philip Mattocks, Paul Wincott, David Vaughan, Xuesong Li, Luigi Colombo, Rodney S. Ruoff, Bruce Hamilton, and Konstantin S. Novoselov. Scanning tunnelling microscopy of suspended graphene. *Nanoscale*, 4(10):3065, 2012.

[6] Daniel Cooper, Benjamin D'Anjou, Nageswara Ghattamaneni, Benjamin Harack, Michael Hilke, Alexandre Horth, Norberto Majlis, Mathieu Massicotte, Leron Vandsburger, Eric Whiteway, and Victor Yu. Experimental review of graphene. *ISRN Condensed Matter Physics*, 2012:1–56, April 2012.

[7] Luis E. F. Foa Torres, Stephan Roche, and Jean-Christophe Charlier. *Introduction to Graphene-Based Nanomaterials: From Electronic Structure to Quantum Transport.* Cambridge University Press, 2^{nd} edition, March 2020.

[8] P. R. Wallace. The band theory of graphite. *Physical Review*, 71(9):622–634, May 1947.

[9] K. Novoselov, A.K. Geim, S. Morozov, Dingde Jiang, Mikhail Katsnelson, Irina Grigorieva, S.V. Dubonos, and Anatoly Firsov. Two-dimensional gas of massless dirac fermions in graphene. *Nature*, 438(7065):197–200, December 2005.

[10] A. Geim and K. Novoselov. The rise of graphene. *Nature materials*, 6(3):183–91, April 2007.

[11] S. V. Morozov, K. S. Novoselov, M. I. Katsnelson, F. Schedin, D. C. Elias, J. A. Jaszczak, and A. K. Geim. Giant intrinsic carrier mobilities in graphene and its bilayer. *Physical Review Letters*, 100(1):016602, January 2008.

[12] D. C. Elias, R. V. Gorbachev, A. S. Mayorov, S. V. Morozov, A. A. Zhukov, P. Blake, L. A. Ponomarenko, I. V. Grigorieva, K. S. Novoselov, F. Guinea, and A. K. Geim. Dirac cones reshaped by interaction effects in suspended graphene. *Nature Physics*, 7(9):701–704, July 2011.

[13] A. S. Mayorov, D. C. Elias, M. Mucha-Kruczynski, R. V. Gorbachev, T. Tudorovskiy, A. Zhukov, S. V. Morozov, M. I. Katsnelson, A. K. Geim, and K. S. Novoselov and. Interaction-driven spectrum reconstruction in bilayer graphene. *Science*, 333(6044):860–863, August 2011.

[14] Alexander S. Mayorov, Daniel C. Elias, Ivan S. Mukhin, Sergey V. Morozov, Leonid A. Ponomarenko, Kostya S. Novoselov, A. K. Geim, and Roman V. Gorbachev. How close can one approach the dirac point in graphene experimentally? *Nano Letters*, 12(9):4629–4634, September 2012.

[15] Mipt Press Office, Moscow Institute of Physics and Technology. Scientists sort through bilayer graphene, January 2017. url: `https://phys.org/news/2017-01-scientists-bilayer-graphene.html` (accessed on 22-03-2020).

[16] Yuanbo Zhang, Tsung-Ta Tang, Caglar Girit, Zhao Hao, Michael C. Martin, Alex Zettl, Michael F. Crommie, Y. Ron Shen, and Feng Wang. Direct observation of a widely tunable bandgap in bilayer graphene. *Nature*, 459(7248):820–823, June 2009.

[17] Taisuke Ohta, Aaron Bostwick, Thomas Seyller, Karsten Horn, and Eli Rotenberg. Controlling the electronic structure of bilayer graphene. *Science*, 313(5789):951–954, August 2006.

[18] Zahra Torbatian and Reza Asgari. Plasmonic physics of 2D crystalline materials. *Applied Sciences*, 8(2):238, February 2018.

[19] Estelina da Silva, M. Santos, Jonathan Skelton, Tao Yang, T. Santos, Stephen Parker, and Aron Walsh. Electronic and phonon instabilities in bilayer graphene under applied external bias. *Materials Today: Proceedings*, 20:373 – 382, September 2020.

[20] Edward McCann and Vladimir I. Fal'ko. Landau-level degeneracy and quantum hall effect in a graphite bilayer. *Physical Review Letters*, 96(8):086805, March 2006.

[21] Edward McCann and Mikito Koshino. The electronic properties of bilayer graphene. *Reports on Progress in Physics*, 76(5):056503, April 2013.

[22] G. Jones. *Graphene on crystalline insulators: subsurface potentials and screening effects*. PhD thesis, University of Bath, June 2015.

[23] Xiaomeng Liu, Zeyu Hao, Eslam Khalaf, Jong Yeon Lee, Yuval Ronen, Hyobin Yoo, Danial Haei Najafabadi, Kenji Watanabe, Takashi Taniguchi, Ashvin Vishwanath, and et al. Tunable spin-polarized correlated states in twisted double bilayer graphene. *Nature*, 583(7815):221–225, Jul 2020.

[24] Cheng Shen, Yanbang Chu, QuanSheng Wu, Na Li, Shuopei Wang, Yanchong Zhao, Jian Tang, Jieying Liu, Jinpeng Tian, Kenji Watanabe, and et al. Correlated states in twisted double bilayer graphene. *Nature Physics*, 16(5):520–525, Mar 2020.

[25] Yuan Liu, Nathan O. Weiss, Xidong Duan, Hung-Chieh Cheng, Yu Huang, and Xiangfeng Duan. Van der Waals heterostructures and devices. *Nature Reviews Materials*, 1(9):16042, Septembre 2016.

[26] Thomas Galvani, Fulvio Paleari, Henrique P. C. Miranda, Alejandro Molina-Sánchez, Ludger Wirtz, Sylvain Latil, Hakim Amara, and François Ducastelle. Excitons in boron nitride single layer. *Physical Review B*, 94(12):125303, September 2016.

[27] A. K. Geim and I. V. Grigorieva. Van der waals heterostructures. *Nature*, 499(7459):419–425, July 2013.

[28] Andres Castellanos-Gomez. Why all the fuss about 2D semiconductors? *Nature Photonics*, 10(4):202–204, March 2016.

[29] C. R. Dean, A. F. Young, I. Meric, C. Lee, L. Wang, S. Sorgenfrei, K. Watanabe, T. Taniguchi, P. Kim, K. L. Shepard, and J. Hone. Boron nitride substrates for high-quality graphene electronics. *Nature Nanotechnology*, 5(10):722–726, August 2010.

[30] J. Martin, N. Akerman, G. Ulbricht, T. Lohmann, J. H. Smet, K. von Klitzing, and A. Yacoby. Observation of electron–hole puddles in graphene using a scanning single-electron transistor. *Nature Physics*, 4(2):144–148, November 2007.

[31] Xu Du, Ivan Skachko, Anthony Barker, and Eva Y. Andrei. Approaching ballistic transport in suspended graphene. *Nature Nanotechnology*, 3(8):491–495, July 2008.

[32] Eduardo V. Castro, H. Ochoa, M. I. Katsnelson, R. V. Gorbachev, D. C. Elias, K. S. Novoselov, A. K. Geim, and F. Guinea. Limits on charge carrier mobility in suspended graphene due to flexural phonons. *Physical Review Letters*, 105(26):266601, December 2010.

[33] Alexander S. Mayorov, Roman V. Gorbachev, Sergey V. Morozov, Liam Britnell, Rashid Jalil, Leonid A. Ponomarenko, Peter Blake, Kostya S. Novoselov, Kenji

Watanabe, Takashi Taniguchi, and A. K. Geim. Micrometer-scale ballistic transport in encapsulated graphene at room temperature. *Nano Letters*, 11(6):2396–2399, June 2011.

[34] C. R. Woods, L. Britnell, A. Eckmann, R. S. Ma, J. C. Lu, H. M. Guo, X. Lin, G. L. Yu, Y. Cao, R. V. Gorbachev, A. V. Kretinin, J. Park, L. A. Ponomarenko, M. I. Katsnelson, Yu. N. Gornostyrev, K. Watanabe, T. Taniguchi, C. Casiraghi, H-J. Gao, A. K. Geim, and K. S. Novoselov. Commensurate–incommensurate transition in graphene on hexagonal boron nitride. *Nature Physics*, 10(6):451–456, April 2014.

[35] C. R. Dean, L. Wang, P. Maher, C. Forsythe, F. Ghahari, Y. Gao, J. Katoch, M. Ishigami, P. Moon, M. Koshino, T. Taniguchi, K. Watanabe, K. L. Shepard, J. Hone, and P. Kim. Hofstadter's butterfly and the fractal quantum hall effect in moiré superlattices. *Nature*, 497(7451):598–602, May 2013.

[36] J. R. Wallbank, A. A. Patel, M. Mucha-Kruczyński, A. K. Geim, and V. I. Falko. Generic miniband structure of graphene on a hexagonal substrate. *Physical Review B*, 87(24):245408, June 2013.

[37] B. Hunt, J. D. Sanchez-Yamagishi, A. F. Young, M. Yankowitz, B. J. LeRoy, K. Watanabe, T. Taniguchi, P. Moon, M. Koshino, P. Jarillo-Herrero, and R. C. Ashoori. Massive dirac fermions and hofstadter butterfly in a van der waals heterostructure. *Science*, 340(6139):1427–1430, May 2013.

[38] Matthew Yankowitz, Jiamin Xue, Daniel Cormode, Javier D. Sanchez-Yamagishi, K. Watanabe, T. Taniguchi, Pablo Jarillo-Herrero, Philippe Jacquod, and Brian J. LeRoy. Emergence of superlattice dirac points in graphene on hexagonal boron nitride. *Nature Physics*, 8(5):382–386, March 2012.

[39] L. A. Ponomarenko, R. V. Gorbachev, G. L. Yu, D. C. Elias, R. Jalil, A. A. Patel, A. Mishchenko, A. S. Mayorov, C. R. Woods, J. R. Wallbank, M. Mucha-Kruczynski, B. A. Piot, M. Potemski, I. V. Grigorieva, K. S. Novoselov, F. Guinea, V. I. Fal'ko, and A. K. Geim. Cloning of dirac fermions in graphene superlattices. *Nature*, 497(7451):594–597, May 2013.

[40] Matthew Yankowitz, Jiamin Xue, and B J LeRoy. Graphene on hexagonal boron nitride. *Journal of Physics: Condensed Matter*, 26(30):303201, July 2014.

[41] Stephen Carr, Daniel Massatt, Shiang Fang, Paul Cazeaux, Mitchell Luskin, and Efthimios Kaxiras. Twistronics: Manipulating the electronic properties of two-dimensional layered structures through their twist angle. *Physical Review B*, 95(7):075420, February 2017.

[42] Rebeca Ribeiro-Palau, Changjian Zhang, Kenji Watanabe, Takashi Taniguchi, James Hone, and Cory R. Dean. Twistable electronics with dynamically rotatable heterostructures. *Science*, 361(6403):690–693, August 2018.

[43] Kyounghwan Kim, Matthew Yankowitz, Babak Fallahazad, Sangwoo Kang, Hema C. P. Movva, Shengqiang Huang, Stefano Larentis, Chris M. Corbet, Takashi Taniguchi, Kenji Watanabe, Sanjay K. Banerjee, Brian J. LeRoy, and Emanuel Tutuc. van der waals heterostructures with high accuracy rotational alignment. *Nano Letters*, 16(3):1989–1995, February 2016.

[44] Duoming Wang, Guorui Chen, Chaokai Li, Meng Cheng, Wei Yang, Shuang Wu, Guibai Xie, Jing Zhang, Jing Zhao, Xiaobo Lu, Peng Chen, Guole Wang, Jianling Meng, Jian Tang, Rong Yang, Congli He, Donghua Liu, Dongxia Shi, Kenji Watanabe, Takashi Taniguchi, Ji Feng, Yuanbo Zhang, and Guangyu Zhang. Thermally induced graphene rotation on hexagonal boron nitride. *Physical Review Letters*, 116(12):126101, March 2016.

[45] C. R. Woods, F. Withers, M. J. Zhu, Y. Cao, G. Yu, A. Kozikov, M. Ben Shalom, S. V. Morozov, M. M. van Wijk, A. Fasolino, M. I. Katsnelson, K. Watanabe, T. Taniguchi, A. K. Geim, A. Mishchenko, and K. S. Novoselov. Macroscopic self-reorientation of interacting two-dimensional crystals. *Nature Communications*, 7(1):10800, March 2016.

[46] Axel Eckmann, Jaesung Park, Huafeng Yang, Daniel Elias, Alexander S. Mayorov, Geliang Yu, Rashid Jalil, Kostya S. Novoselov, Roman V. Gorbachev, Michele Lazzeri, Andre K. Geim, and Cinzia Casiraghi. Raman fingerprint of aligned graphene/h-BN superlattices. *Nano Letters*, 13(11):5242–5246, October 2013.

[47] Pilkyung Moon and Mikito Koshino. Electronic properties of graphene/hexagonal-boron-nitride moiré superlattice. *Physical Review B*, 90(15):155406, October 2014.

[48] M. Mucha-Kruczyński, J. R. Wallbank, and V. I. Falko. Heterostructures of bilayer graphene andh-BN: Interplay between misalignment, interlayer asymmetry, and trigonal warping. *Physical Review B*, 88(20):205418, November 2013.

[49] Alexis Warnier. Fabrication and electrical transport properties of twisted bilayer graphene devices. Master's thesis, Université Catholique de Louvain, August 2019.

[50] K. Zeranska-Chudek, A. Lapinska, A. Wroblewska, J. Judek, A. Duzynska, M. Pawlowski, A. M. Witowski, and M. Zdrojek. Study of the absorption coefficient of graphene-polymer composites. *Scientific Reports*, 8(1):9132, June 2018.

[51] A. C. Ferrari, J. C. Meyer, V. Scardaci, C. Casiraghi, M. Lazzeri, F. Mauri, S. Piscanec, D. Jiang, K. S. Novoselov, S. Roth, and A. K. Geim. Raman spectrum of graphene and graphene layers. *Physical Review Letters*, 97(18):187401, October 2006.

[52] C. Neumann, S. Reichardt, P. Venezuela, M. Drögeler, L. Banszerus, M. Schmitz, K. Watanabe, T. Taniguchi, F. Mauri, B. Beschoten, S. V. Rotkin, and C. Stampfer. Raman spectroscopy as probe of nanometre-scale strain variations in graphene. *Nature Communications*, 6(1):8429, September 2015.

[53] Bin Cheng, Peng Wang, Cheng Pan, Tengfei Miao, Yong Wu, T. Taniguchi, K. Watanabe, C. N. Lau, and M. Bockrath. Raman spectroscopy measurement of bilayer graphenes twist angle to boron nitride. *Applied Physics Letters*, 107(3):033101, July 2015.

[54] Ado Jorio, Riichiro Saito, Gene Dresselhaus, and Mildred S. Dresselhaus. *Raman Spectroscopy in Graphene Related Systems*. Wiley-VCH Verlag GmbH & Co. KGaA, January 2011.

[55] Katherine J. I. Ember, Marieke A. Hoeve, Sarah L. McAughtrie, Mads S. Bergholt, Benjamin J. Dwyer, Molly M. Stevens, Karen Faulds, Stuart J. Forbes, and Colin J. Campbell. Raman spectroscopy and regenerative medicine: a review. *npj Regenerative Medicine*, 2(1):12, May 2017.

[56] Andrea C. Ferrari and Denis M. Basko. Raman spectroscopy as a versatile tool for studying the properties of graphene. *Nature Nanotechnology*, 8(4):235–246, April 2013.

[57] Zhenhua Ni, Yingying Wang, Ting Yu, and Zexiang Shen. Raman spectroscopy and imaging of graphene. *Nano Research*, 1(4):273–291, October 2008.

[58] Patrick May, Michele Lazzeri, Pedro Venezuela, Felix Herziger, Gordon Callsen, Juan S. Reparaz, Axel Hoffmann, Francesco Mauri, and Janina Maultzsch. Signature of the two-dimensional phonon dispersion in graphene probed by double-resonant raman scattering. *Physical Review B*, 87(7):075402, February 2013.

[59] Riccardo Frisenda, Efrén Navarro-Moratalla, Patricia Gant, David Pérez De Lara, Pablo Jarillo-Herrero, Roman V. Gorbachev, and Andres Castellanos-Gomez. Recent progress in the assembly of nanodevices and van der waals heterostructures by deterministic placement of 2d materials. *Chemical Society Reviews*, 47(1):53–68, 2018.

[60] L. Wang, I. Meric, P. Y. Huang, Q. Gao, Y. Gao, H. Tran, T. Taniguchi, K. Watanabe, L. M. Campos, D. A. Muller, J. Guo, P. Kim, J. Hone, K. L. Shepard, and C. R. Dean. One-dimensional electrical contact to a two-dimensional material. *Science*, 342(6158):614–617, October 2013.

[61] Phaedon Avouris and Christos Dimitrakopoulos. Graphene: synthesis and applications. *Materials Today*, 15(3):86–97, March 2012.

[62] Alexander E. Filippov, Martin Dienwiebel, Joost W. M. Frenken, Joseph Klafter, and Michael Urbakh. Torque and twist against superlubricity. *Physical Review Letters*, 100(4):046102, January 2008.

[63] Ze Liu, Jiarui Yang, Francois Grey, Jefferson Zhe Liu, Yilun Liu, Yibing Wang, Yanlian Yang, Yao Cheng, and Quanshui Zheng. Observation of microscale superlubricity in graphite. *Physical Review Letters*, 108(20):205503, May 2012.

[64] E. Koren and U. Duerig. Moiré scaling of the sliding force in twisted bilayer graphene. *Physical Review B*, 94(4):045401, July 2016.

[65] M. M. van Wijk, M. Dienwiebel, J. W. M. Frenken, and A. Fasolino. Superlubric to stick-slip sliding of incommensurate graphene flakes on graphite. *Physical Review B*, 88(23):235423, December 2013.

[66] Martin Dienwiebel, Namboodiri Pradeep, Gertjan S. Verhoeven, Henny W. Zandbergen, and Joost W.M. Frenken. Model experiments of superlubricity of graphite. *Surface Science*, 576(1-3):197–211, February 2005.

[67] Michael Weiss and Franz-Josef Elmer. Dry friction in the frenkel-kontorova-tomlinson model: Static properties. *Physical Review B*, 53(11):7539–7549, March 1996.

[68] Woo Kyun Kim and Michael L. Falk. Atomic-scale simulations on the sliding of incommensurate surfaces: The breakdown of superlubricity. *Physical Review B*, 80(23):235428, December 2009.

[69] Y Dong, Q Li, J Wu, and A Martini. Friction, slip and structural inhomogeneity of the buried interface. *Modelling and Simulation in Materials Science and Engineering*, 19(6):065003, July 2011.

[70] Ali Erdemir and Jean Martin. *Superlubricity*. Elsevier, January 2007.

[71] Yiming Song, Davide Mandelli, Oded Hod, Michael Urbakh, Ming Ma, and Quanshui Zheng. Robust microscale superlubricity in graphite/hexagonal boron nitride layered heterojunctions. *Nature Materials*, 17(10):894–899, July 2018.

[72] D. Mandelli, I. Leven, O. Hod, and M. Urbakh. Sliding friction of graphene/hexagonal –boron nitride heterojunctions: a route to robust superlubricity. *Scientific Reports*, 7(1):10851, September 2017.

[73] Dirk Dietzel, Michael Feldmann, Udo D. Schwarz, Harald Fuchs, and André Schirmeisen. Scaling laws of structural lubricity. *Physical Review Letters*, 111(23):235502, December 2013.

Appendices

Appendix A

Supplementary illustrations of the fabrication process

A.1 Additional imagery of the transferred stacks of flakes

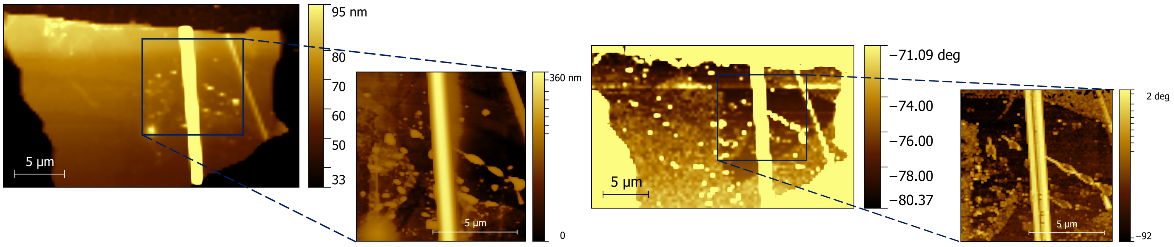

(a) (b)

Figure A.1: Supplementary zoomed image of sample 2 after the transfer step. (a) Topography (b) phase image.

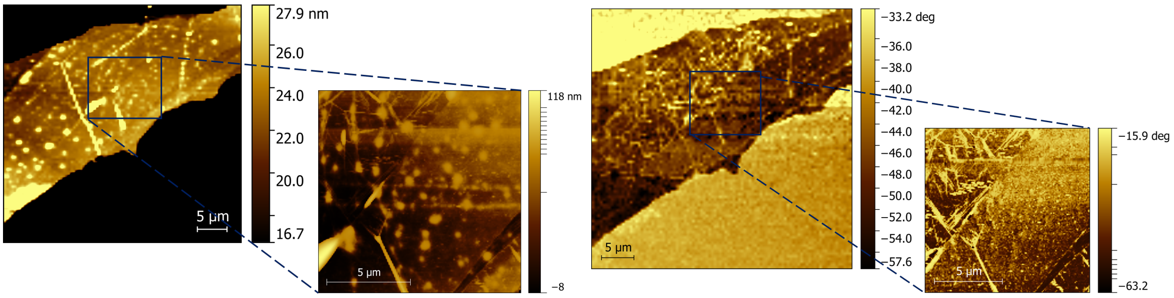

(a) (b)

Figure A.2: Supplementary zoomed image of sample 3 after the transfer step. (a) Topography (b) phase image.

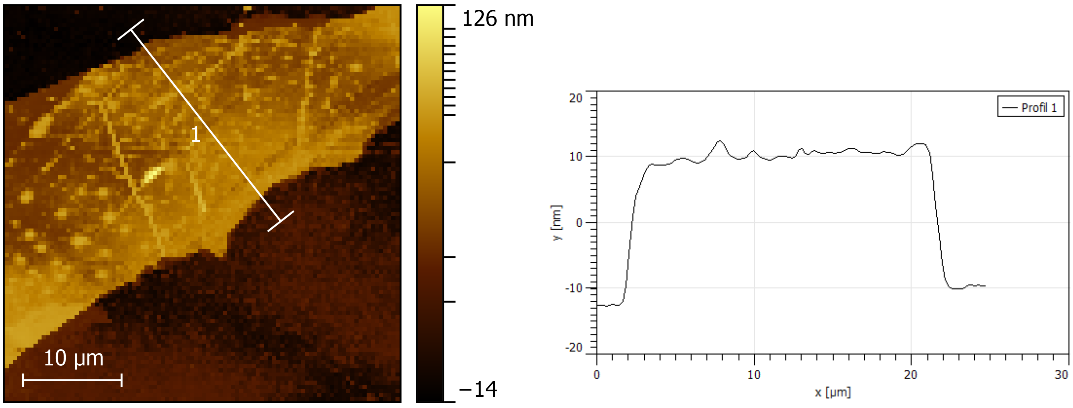

(a) (b)

Figure A.3: (a) Topographic AFM image of Sample 3. (b) Profile extracted along an arbitrary line labeled (1) drawn in white on (a).

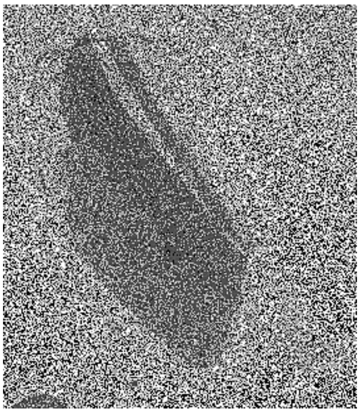

Figure A.4: SEM image of sample 3 before lithography. Here, the BLG/graphite flake appears very visible, but the hBN bottom layer doesn't seem detectable.

A.2 F.I.B. milled squares

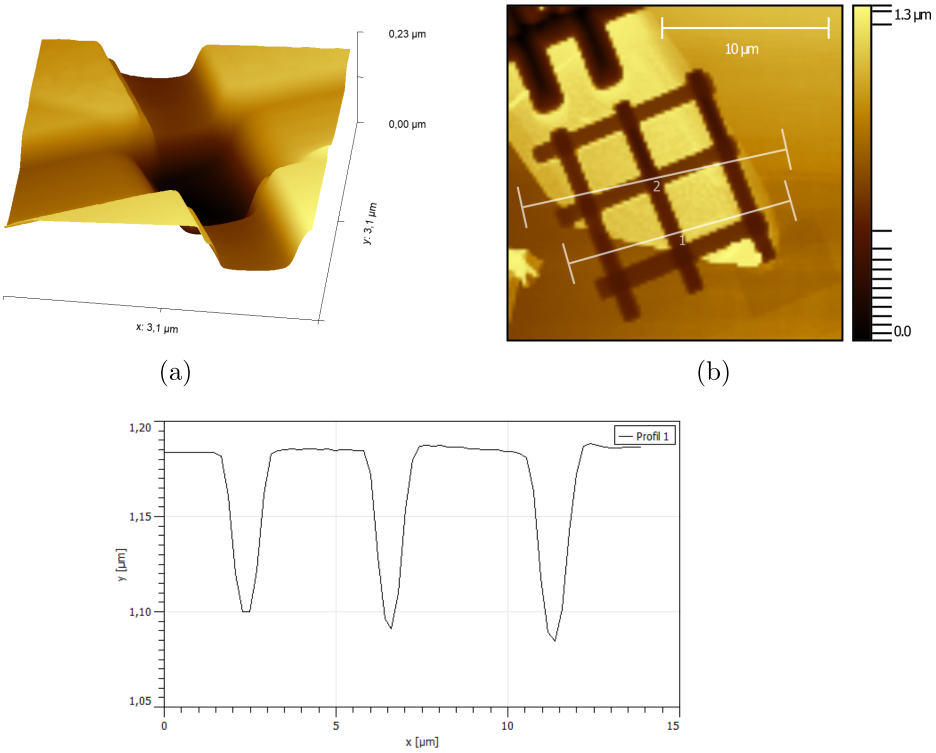

(a)

(b)

(c)

Figure A.5: 3D (a) and 2D (b) AFM topography images of the squares milled with the F.I.B. in an hBN flake. (c) Thickness profile along the line labeled 1 (in white on figure b), allowing to appreciate the depth and vertical edges obtained from F.I.B. milling.

A.3 Optical images of the final device

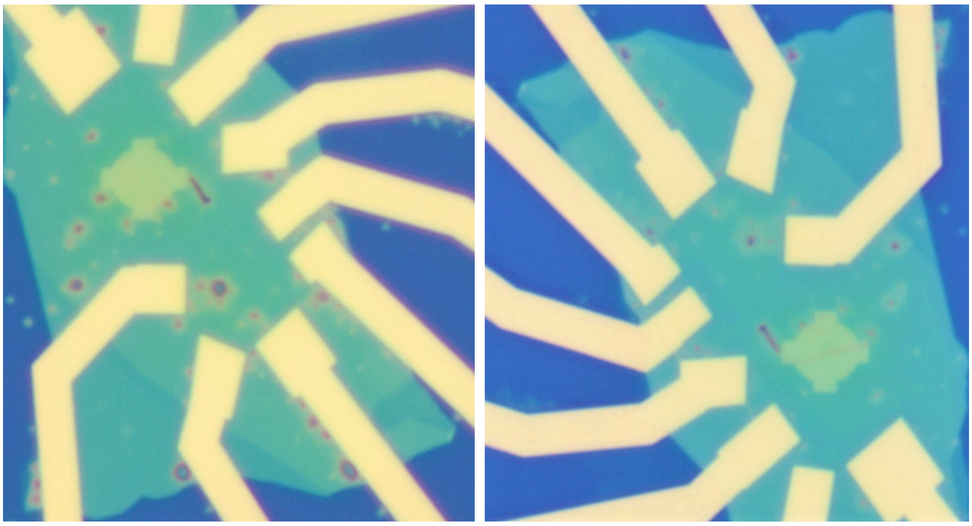
(a) (b)

Figure A.6: Optical microscope image of the finished sample (a) before and (b) after leaving the sample in acetone for around 30 min. Remaining droplets of PPC are visible in purple.

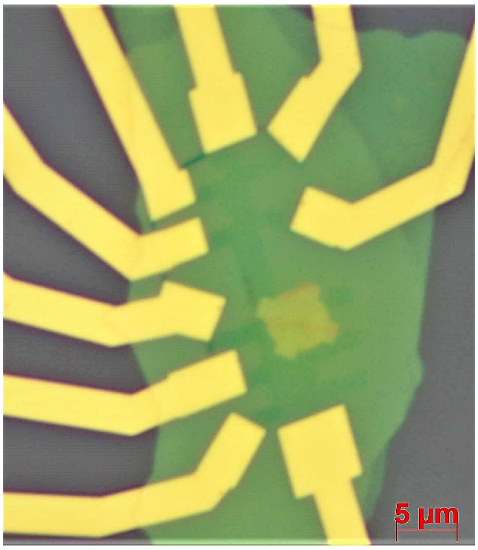

Figure A.7: Optical microscope of the nearly finished sample (with one pure hBN wheel) before removing the PPC layer, allowing to distinguish the BLG Hall bar (with adapted contrast), and thus providing a representative view of the device.

Appendix B

Supplementary experimental data

B.1 Additional friction curves

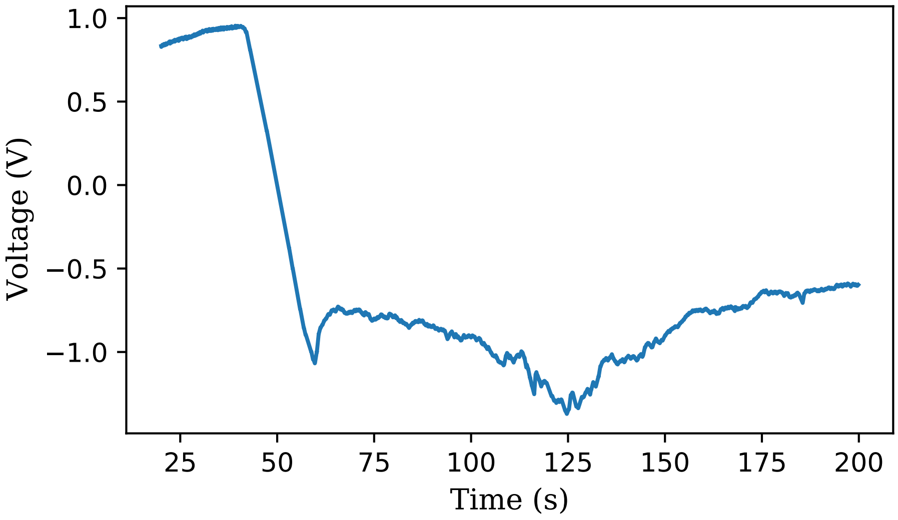

Figure B.1: Friction curve that was provided on Figure 4.13, but here shown in its entirety.

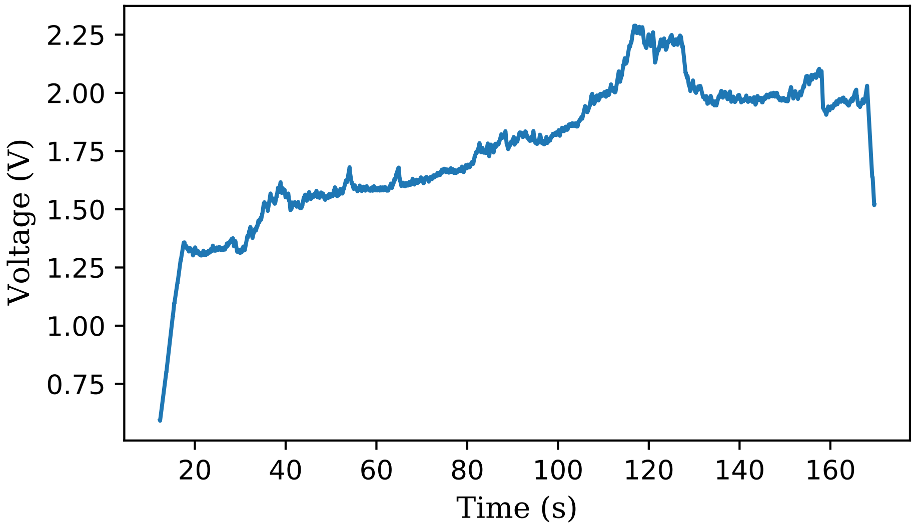

Figure B.2: Other friction curve, measured while crossing the alignment position (tip velocity: $0.01\mu m/s$). The curve looks less smooth and clean, suggesting that the friction occurred with much more impurities, which makes the data hard to analyze.

B.2 Raman 2D-peak fitting in noisy signals

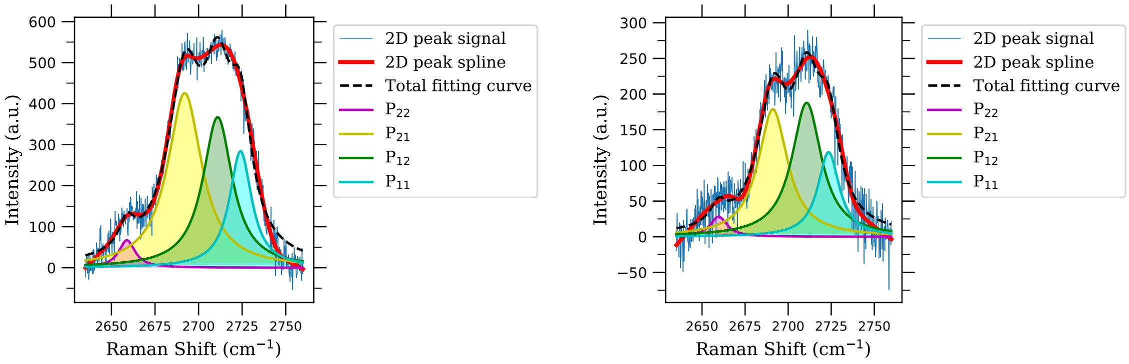

(a) (b)

Figure B.3: 2D peak from the spectra shown on Figure 4.16 and 4.17, with the Lorentzian fitting estimation, yielding the 2D subpeaks.

UNIVERSITÉ CATHOLIQUE DE LOUVAIN
École polytechnique de Louvain
Rue Archimède, 1 bte L6.11.01, 1348 Louvain-la-Neuve, Belgique | **www.uclouvain.be/epl**